

NORTHWESTERN UNIVERSITY

**Search for Two Omega Meson Decays
of Charmonium Resonances
Produced in Proton-Antiproton Annihilations**

A DISSERTATION

SUBMITTED TO THE GRADUATE SCHOOL
IN PARTIAL FULFILLMENT OF THE REQUIREMENTS

for the degree

DOCTOR OF PHILOSOPHY

Field of Physics

By

Jason J. Kasper

EVANSTON, ILLINOIS

June 2002

Gift Thesis AA 64629

© Copyright by JASON J. KASPER 2002
All Rights Reserved

Abstract

Search for Two Omega Meson Decays of Charmonium Resonances Produced in Proton-Antiproton Annihilations

Jason J. Kasper

In Fermilab experiment E835 a search has been performed for two $\omega(782)$ vector meson decays of charmonium produced via $\bar{p}p$ annihilation. All states with even charge conjugation quantum number are theoretically accessible via $\omega\omega$. No charmonium signals were clearly visible. The large nonresonant continuum from $\bar{p}p$ annihilation to $\omega\omega$ was observed to be predominantly pseudoscalar. 90% upper limit confidence intervals were calculated for $B(\eta_c \rightarrow \omega\omega)$ assuming various phase shifts, δ , between the resonant and nonresonant $\omega\omega$ production giving a range from 0.54% for $\delta = 180^\circ$ to 18% for $\delta = 0^\circ$. Upper limits on $B(\bar{p}p \rightarrow \eta'_c) \times B(\eta'_c \rightarrow \omega\omega)$ are also given over a range of assumed masses and widths for the η'_c .

To my wife Lisa,
no one deserves this page more

Acknowledgments

First, I would like to thank my advisor, Jerry Rosen. The most important quality I required in an advisor was having one whose grasp of physics was solid – certainly Jerry fits this description. I would also like to thank Stephen Pordes and Keith Gollwitzer. They have always been available for guidance and were never afraid to jump into the details of whatever issue was at the forefront of one's workload. Thanks also go to Paolo Rumerio and Ted Vidnovic (watching their analyses develop helped me greatly in understanding my own), and to Rosanna Cester who has been an inspirational and reassuring presence for the experiment. To those not directly named – I respect the collective intellect of the people on this experiment, and I hope wherever I end up I work again with this quality of people.

I'd like to give recognition to my professors from both CWRU and Northwestern especially Ken Kowalski who loved to work out any problem in bloody detail, Bruce Ikenaga, Charles Wells, Jerry Goodman who first got me interested in Math, and Rich Larcom who helped me push forward when some would have held me back.

This thesis is the result of many years of work so I would like to thank the people who helped me get to this point without cracking up: Bill Dimmock, Erick Foor, Scott Kaul and Shannon Barber, Jack and Jill Murrin, Doug and Jennifer Noernburg, Susumu Saito, and Gary Hunsberger. To my extended family who were particularly supportive throughout these years, especially Marlene and Clyde Honermann, my Grandfather, Ray Kasper (the other Dr. Kasper), my sister Kristy and her husband Chris, and my parents John and Carol – I hope I can end up half as good of parents as they are – thanks to you all. Finally, the greatest amount of thanks goes to my wife, Lisa, who had to put up with the ups and downs, late night shifts, low pay, last minute framemaker plots, etc. so that I could see my goal to completion.

Curriculum Vitae

Jason J. Kasper
Northwestern University
Fermilab Experiment E835

Education

- 2002 Northwestern University, Evanston, IL**
Ph.D. in Physics
Dissertation: "Search for Two Omega Meson Decays of Charmonium Produced in Proton-Antiproton Annihilations"
Advisor: Professor Jerome Rosen
- 1995 Case Western Reserve University, Cleveland, OH**
B.S. in Physics
Senior Thesis: " K_S^0 , Λ^0 Discrimination at Minimax"
Advisor: Professor Ken Kowalski
Leslie L. Foldy Award for Outstanding Senior in Physics
- 1995 Case Western Reserve University, Cleveland, OH**
B.S. in Mathematics
Junior Thesis: "Primes and the Central Binomial Coefficient"
Advisor: Professor Charles Wells

Experience

- 1996 – 2002 Northwestern University, Evanston, IL**
Research Assistant for Professor Jerome Rosen
DESY Experiment HERA B: Built Lens Structure for Ring Imaging Čerenkov Detector.
Fermilab Experiment E835: Maintained, monitored, and modified Neutral Trigger electronics and software. Aided in Calorimeter installation for 1996 and 1999 runs.
- 1995 – 1996 Northwestern University, Evanston, IL**
Teaching Assistant in Physics Department.
Lectured, Graded, and Supervised General Physics Labs.

Publications

M. Ambrogiani et al. "Study of the Angular Distributions of the Reactions Anti-P P \rightarrow Chi/c1, Chi/c2 \rightarrow J/Psi Gamma \rightarrow E+ E- Gamma." *Physical Review* D65:052002 (2001).

C. Patrignani et al. "E835 at FNAL: Charmonium Spectroscopy in Anti-P P Annihilations." *Nuclear Physics* A692:308 (2001).

M. Ambrogiani et al. "Search for the Eta(C)-Prime (2 1(S)0) Charmonium Resonance." *Physical Review* D64:052003 (2001).

M. Ambrogiani et al. "Study of the $\gamma\gamma$ Decays of the χ_2 (1^3P_2) and χ_0 (1^3P_0) Charmonium Resonances." *Physical Review* D62:052002 (2000).

M. Ambrogiani et al. "Measurement of the Branching Ratios $\psi' \rightarrow e^+e^-$, $\psi' \rightarrow J/\psi \pi^0\pi^0$ and $\psi' \rightarrow J/\psi \eta$." *Physical Review* D62:032004 (2000).

M. Ambrogiani et al. "Study of the χ_0 (1^3P_0) State of Charmonium Formed in $\bar{p}p$ Annihilations." *Physical Review Letters* 83:2902 (1999).

M. Ambrogiani et al. "Measurements of the Magnetic Form Factor of the Proton in the Timelike Region at Large Momentum Transfer." *Physical Review* D60:032002 (1999).

Contents

Abstract	iii
Acknowledgments	v
List of Figures	xxi
List of Tables	xxiv
1 Introduction	1
1.1 History	4
1.1.1 The Charm Quark	5
1.1.2 History of Charmonium	7
1.1.3 The Charmonium Spectrum	10
1.2 Theoretical Motivation	12
1.2.1 Strong Force Interactions	13

1.2.2	Charmonium Study	17
1.3	E835 Experiment Technique	21
1.3.1	Production of Charmonium	22
1.3.2	Resonance Scanning	25
1.4	Production of $\omega\omega$	27
2	Experiment Apparatus	30
2.1	The Antiproton Ring	30
2.1.1	Antiproton Accumulation	31
2.1.2	Beam Deceleration	34
2.2	The Hydrogen Gas Jet Target	39
2.3	E835 Detector	41
2.3.1	Luminosity Monitor	42
2.3.2	Inner Detectors	44
2.3.3	Threshold Čerenkov Counter	48
2.3.4	Central Calorimeter	51
2.3.5	Forward Calorimeter	66
3	Data Acquisition	68
3.1	DAQ Hardware	68

3.2	E835 Trigger	69
3.2.1	The Charged Trigger	71
3.2.2	Neutral Trigger	74
3.2.3	Energy Discriminators	84
3.3	Master MLU	86
3.4	Gatemaster	88
3.5	PRUDE Software Trigger	89
4	$\omega\omega$ Event Selection	94
4.1	Preliminary $\omega\omega$ Candidate Selection	95
4.1.1	Neutral Data Summary Tapes	96
4.1.2	Total Energy Trigger Selection	96
4.1.3	Fiducial Volume Cut	97
4.1.4	Cluster Invariant Mass Cuts	98
4.1.5	Fit to $2\pi^0 2\gamma$ Hypothesis	100
4.1.6	$\pi^0\gamma$ Pairings	103
4.1.7	$ \cos\theta^* $ Cut	104
4.2	Angular Distribution of $\omega\omega$	106
4.2.1	Possible $\omega\omega$ Quantum Numbers	107
4.2.2	Helicity Formulation	110

4.3	Background Subtraction	117
4.4	Efficiencies	124
4.4.1	Trigger Efficiencies	126
4.4.2	Photon Conversions	127
4.4.3	NDST Efficiency	128
4.4.4	Overlapping Event Contamination	129
4.4.5	Analysis Efficiency	131
5	Results and Conclusions	137
5.1	Results of the Selection	137
5.2	Hard Cuts on Angular Distribution	138
5.3	Angular Distributions	144
5.4	Upper Limits	157
5.4.1	Technique for Determining Limits	157
5.4.2	Upper Limit of the η_c	158
5.4.3	Upper Limit of the η'_c	163
5.5	Conclusions	167
A	Neutral Trigger Performance	173
A.1	Threshold Monitoring	174

A.2	PBG Efficiencies	177
A.3	Total Energy Efficiencies	178
B	Neutral Data Summary Tapes	182
C	Angular Dependence of the Differential Cross Section	185
C.1	Brief Introduction to D-functions	186
C.2	Calculation of the $\omega\omega$ Distribution	188

List of Figures

1.1	Neutral Current Coupling in Terms of the Cabibbo Doublet	6
1.2	Diagrams for the Strange and Charm Contributions to the Neutral Current Coupling According to the GIM Mechanism	8
1.3	OZI Suppressed Decay of J/ψ to $\pi^+\pi^-\pi^0$	9
1.4	OZI Allowed Decay of $\psi(3770)$ to Two Charged D Mesons	9
1.5	The Charmonium Spectrum	11
1.6	QCD Vertices for (a) qqg (b) ggg (c) gggg	14
1.7	Overlap of Light Quarkonia States [21]. The width of the state is represented by the hash marks at its mass.	20
1.8	e^+e^- Annihilation Producing Charmonium via a Virtual Photon . . .	23
1.9	Production of Charmonium via $\gamma\gamma$ Fusion	23
1.10	$\bar{p}p$ Annihilation Producing Charmonium via (a) 3 Gluons and (b) 2 Gluons	24

1.11	Mechanisms for η_c Decay to Two Mesons. Note (b) results in a color octet that is assumed to become singlet under a final state gluon exchange.	28
2.1	Antiproton Ring	32
2.2	Schottky Power Spectrum at $\sqrt{s}=3686$ MeV. The resolution is about 30 Hz. The vertical scale is 10 db/div.	36
2.3	Typical ψ' Scan	38
2.4	Cluster Formation from the Gas Jet Nozzle	39
2.5	Gas Jet Density as Function of Temperature and Pressure	40
2.6	As the beam current falls, the gas density (not shown on plot) is raised enough to keep luminosity constant.	41
2.7	The E835 Detector	42
2.8	Representation of the E835 Luminosity Monitor	43
2.9	Typical Luminosity Spectrum	44
2.10	Beam's View of the Inner Detectors. Only one quarter is shown. . . .	45
2.11	Threshold Curves for Čerenkov Cells	49
2.12	Cross Section Schematic of the Čerenkov Counter	50
2.13	Schematic of a CCAL Wedge	51
2.14	Beam's View of the Central Calorimeter	52

2.15	Side View of the Central Calorimeter	52
2.16	The Laser Monitor System	55
2.17	Ratio of Corrected (bottom) and Uncorrected (top) Energies to the Predicted Energy from $J/\psi \rightarrow e^+e^-$ as a Function of Distance from the Crack	59
2.18	Cluster Mass Showing Electrons, Photons, and Pions	61
2.19	π^0 Asymmetry Plotted without Split Clusters (shaded) and Including Split Clusters (open)	62
2.20	Deviation of ϕ from Two-Body Kinematics	63
2.21	Deviation of θ from Two-Body Kinematics	64
2.22	Deviation of Energy from Two-Body Kinematics	65
2.23	Forward Calorimeter I Schematic	66
2.24	Forward Calorimeter II Schematic	67
3.1	The E835 DAQ System	70
3.2	E835 Trigger System	72
3.3	Schematic of the E835 Neutral Trigger	75

3.4	Beam's View of the Central Calorimeter. Structure of the 40 overlapping super-blocks in a $5 (\Theta) \times 8 (\Phi)$ array. The overlaps are indicated by the dashed lines and are described in tables 3.2 and 3.3. Super blocks $(\Phi, \Theta) = (1, 2)$ and $(5, 5)$ are shaded.	77
3.5	Circuit Diagram for the Level I Summers. Resistor values are in ohms and capacitor values are in pF.	79
3.6	Monte Carlo simulation of the kinematics for $\bar{p}p \rightarrow J/\psi \rightarrow e^+e^-$. The electron energy as a function of ring number is shown in the top plot without the weighting factors and in the bottom plot with the weighting factors.	81
3.7	Integrator	84
4.1	Invariant Mass of all Two Cluster Combinations for E_{cm} Less than 2.985 GeV. The vertical lines are at $m_{\pi^0} \pm 0.035$ GeV.	99
4.2	Invariant Mass of all Two Cluster Combinations for E_{cm} Less than 2.985 GeV Excluding any Mass within 35 MeV of the π^0 . The η (547 MeV), pseudo- ω (slightly less than 782 MeV), and η' (958 MeV) peaks are visible.	100
4.3	Invariant Mass of all Three Cluster Combinations in the η_c Energy Region	101

4.4	Invariant Mass of all Three Cluster Combinations for Events in the η_c Energy Region (Cuts 1-4 Have Been Applied). The ω mass peak is clearly visible.	102
4.5	χ^2 Probability of Fit for $2\pi^0 2\gamma$ Hypothesis for a Typical Subset of the Six Cluster Data. The arrow is at $P(\chi^2) = 5\%$	103
4.6	$\bar{p}p$ to $\omega\omega$ with Two Spectator Quarks (Class 2)	105
4.7	$ \cos\theta^* $ Distribution for $\omega\omega$ Candidate Events in the η_c Region	106
4.8	Angles Describing the $\omega\omega$ Production and Decay	110
4.9	Two $\pi^0\gamma$ Pairs' Invariant Masses	117
4.10	Two $\pi^0\gamma$ Pairs' Invariant Masses with a Fit	118
4.11	Fit with and without the 2-D Gaussian Peak (Real $\omega\omega$ Events)	119
4.12	Projection of Real Data and Background Part of the Fit	120
4.13	$\pi^0\gamma$ Invariant Mass Scatter Plot (Corners Removed and $m_\omega \pm 2\sigma$ Bands)	120
4.14	Rotation of scatter plot by 45° about (m_ω, m_ω)	121
4.15	Projection of rotated scatter plot on the x-axis Fit to a Line and a Gaussian	122
4.16	$\cos\theta^*$ Distributions for Bands 1, 2, 7, and 8 (Overlaid)	123
4.17	$\cos\theta_\gamma$ Distributions for Bands 1, 2, 7, and 8 (Overlaid)	123
4.18	$\cos 2\beta$ Distributions for Bands 1, 2, 7, and 8 (Overlaid)	124

4.19	NDST Efficiency as a Function of Center of Mass Energy	129
4.20	Overlapping Event Detection Efficiency vs. Instantaneous Luminosity	131
4.21	Acceptance in Bins of $\cos \theta^*$ and β	134
4.22	Acceptance in Bins of $\cos \theta_\gamma$ and $\cos \theta^*$	135
4.23	Acceptance in Bins of $\cos \theta_\gamma$ and β	136
5.1	$\omega\omega$ Cross Section in the Energy Range 2.91 GeV to 3.8 GeV. Data is in 2 MeV bins. Lower figure is a log plot of the upper figure.	139
5.2	$\omega\omega$ Cross Section in the Energy Range 2.91 GeV to 3.1 GeV. Data is in 2 MeV bins.	140
5.3	$\omega\omega$ Cross Section in the Energy Range 3.2 GeV to 3.6 GeV. Data is in 2 MeV bins.	141
5.4	$\omega\omega$ Cross Section in the Energy Range 3.5 GeV to 3.6 GeV. Data is in 2 MeV bins.	142
5.5	Data from Figure 5.2 with $\beta \in [\frac{\pi}{5}, \frac{4\pi}{5}]$. Data is in 2 MeV bins.	142
5.6	Data from Figure 5.4 with $\beta \in [\frac{\pi}{5}, \frac{4\pi}{5}]$. Data is in 2 MeV bins.	143
5.7	Data from Figure 5.3 with $\beta \in [0, \frac{2\pi}{5}]$ or $\beta \in [\frac{3\pi}{5}, \pi]$. Data is in 2 MeV bins.	143
5.8	Distributions, in energy bin 2.950 GeV to 2.952 GeV, for (a) $\cos \theta^*$ (b) $\cos \theta_\gamma$ (c) $\cos 2\beta$	145

5.9	Distributions, in energy bin 2.982 GeV to 2.984 GeV, for	
	(a) $\cos \theta^*$ (b) $\cos \theta_\gamma$ (c) $\cos 2\beta$	146
5.10	Distributions, in energy bin 3.096 GeV to 3.098 GeV, for	
	(a) $\cos \theta^*$ (b) $\cos \theta_\gamma$ (c) $\cos 2\beta$	147
5.11	Distributions, in energy bin 3.416 GeV to 3.418 GeV, for	
	(a) $\cos \theta^*$ (b) $\cos \theta_\gamma$ (c) $\cos 2\beta$	148
5.12	Distributions, in energy bin 3.596 GeV to 3.598 GeV, for	
	(a) $\cos \theta^*$ (b) $\cos \theta_\gamma$ (c) $\cos 2\beta$	149
5.13	d/c vs. Energy	151
5.14	$-b/a$ vs. Energy	152
5.15	$\cos \theta^*$ Distribution for 2^{-+} with Various Values of $ a_{1,1} ^2$	156
5.16	Fit to η_c Data with Free Parameters for the Nonresonant Continuum	
	A, D and Resonant Amplitude A_R	159
5.17	Best Fit Values for σ_{peak} for 10^5 MC Experiments	160
5.18	Upper Limit of $B(\eta_c \rightarrow \omega\omega)$ versus Phase Shift	162
5.19	Interference when Cross Section Falls with \sqrt{s} for A_R Arbitrarily Cho-	
	sen as Half the Nonresonant Continuum Amplitude and for Various	
	Values of Phase Shift	164

5.20	90% Confidence Interval Upper Limit for $B(\bar{p}p \rightarrow \eta'_c) \times B(\eta'_c \rightarrow \omega\omega)$ for Various η'_c Masses, a Width of 5.0 MeV, and $\delta = 90^\circ$	165
5.21	90% Confidence Interval Upper Limit for $B(\bar{p}p \rightarrow \eta'_c) \times B(\eta'_c \rightarrow \omega\omega)$ for Various η'_c Masses, a Width of 10.0 MeV, and $\delta = 90^\circ$	166
5.22	90% Confidence Interval Upper Limit for $B(\bar{p}p \rightarrow \eta'_c) \times B(\eta'_c \rightarrow \omega\omega)$ for Various η'_c Masses, a Width of 15.0 MeV, and $\delta = 90^\circ$	167
5.23	Mechanisms for η_c Decay to Two Mesons. Note (b) results in a color octet that is assumed to become singlet under a final state gluon exchange.	171
A.1	Super-Block (3,4) Energy Distribution in GeV (top) and When There was a TDC Hit (bottom)	175
A.2	Threshold Curve. The error bars are binomial.	176
A.3	Threshold Levels vs. Run for Super-Block 20	177
A.4	PBG1 Trigger Efficiency versus Run. The low efficiencies are from runs 1371-2108 when a discriminator width was improperly set. . . .	179
A.5	PBG1 Trigger Efficiency versus Energy (MeV). The low efficiencies are from runs 1371-2108 when a discriminator width was improperly set.	180
A.6	ETOT-HIGH Trigger Efficiency versus Run	180

A.7	ETOT-HIGH Trigger Efficiency versus Energy (MeV)	181
C.1	Angles Describing the $\omega\omega$ Production and Decay	188

List of Tables

2.1	\bar{p} Beam Momentum Required for Particular Center of Mass Energies. The mass given for the η'_c is the median of the E835 search energies. .	34
2.2	Lengths, Angular Position in θ , and Distance to Interaction Point for Blocks in Each CCAL Ring	54
2.3	Shower Profile Constants	58
3.1	The Inputs and Outputs of the CMLU	74
3.2	Blocks in a Ring Summed to Make a Super-Wedge	76
3.3	Rings in a Super-Wedge Summed to Make a Super-Block.	76
3.4	Values of the Weighting Resistors and the Relative Weights for each Input Channel of the Level II Summer. The overlapping channels had two weighting resistors. The ratios are calculated relative to the central channel in each sum (i.e. channel 2, 6, 10, 14 or 18)	82

3.5	Energy and Discriminator Thresholds Values for Super-Blocks. For the η'_c region the value is calculated at 3.594 GeV in the center of mass. For $\eta_c \rightarrow \gamma\gamma$ and $J/\psi \rightarrow e^+e^-$, the thresholds for super-ring five are irrelevant since this region is kinematically inaccessible. . . .	85
3.6	The Inputs and Outputs of the NMLU	87
3.7	The Inputs and Outputs of the MMLU	88
3.8	The Inputs of the Gatemaster	90
3.9	PRUDE IDs, Priorities, Names, and Destination Data Streams	93
4.1	Number of Events Passing the Preliminary $\omega\omega$ Selection and Their Percentage of the Total Sample Set for each Trigger Type	97
4.2	Spin, Relative Angular Momentum (up to $ \vec{L}' = 3$), and J^{PC} for $\omega\omega$.	108
4.3	How $\bar{p}p$ with Specified Quantum Numbers (up to $ \vec{L} = 3$) Produces $\omega\omega$	109
4.4	Numbers of Bins and Their Ranges for the Angles that Define the Differential Cross Section	116
4.5	Efficiencies for Autopass Triggers	126
4.6	Total Energy Trigger (ETOT-HI) Efficiencies	127
4.7	PRUDE ID 51 Efficiencies	128

5.1	Fit Values for the θ_γ Angular Distributions at each of the Sample Energies	150
5.2	Fit Values for the β Angular Distributions at each of the Sample Energies	150
5.3	Results from the Fit to η_c Data	159
5.4	90% Confidence Level Upper Limit for Branching Ratios for η_c to $\omega\omega$ and $\bar{p}p$ to η_c to $\omega\omega$	169
5.5	90% Confidence Level Upper Limit for Branching Ratios of $\bar{p}p$ to η'_c to $\omega\omega$ for a 90° Phase Shift and Assumed η'_c Width Γ	170
5.6	Branching Ratios of η_c to Various Vector-Vector Final States	170
A.1	ETOT-HIGH Efficiencies	179

Chapter 1

Introduction

E835 is an experiment on the antiproton accumulator at the Fermi National Accelerator Laboratory. Our detector is optimized to record electromagnetic final state channels of charmonium decay produced when antiprotons of well defined energies annihilate with an effectively stationary hydrogen gas jet target. The development of stochastic cooling (at CERN by Simon van der Meer) along with the construction of a high resolution lead glass calorimeter helped provide us with a good laboratory for $\bar{c}c$ bound state spectroscopy below the open charm threshold. Because of the large spacing between states and their narrow line widths, $\bar{c}c$ is a good laboratory for study of $\bar{q}q$ bound states in general. Spectroscopic mapping of the $\bar{c}c$ states will aid in developing and testing an improved theory of hadron bound state structure.

In all modes of charmonium production, the study of the singlet states has been problematic – the first pseudoscalar radial excitation (η'_c) and the pseudovector state (1P_1 – first seen in this experiment's predecessor, E760) need confirmation. Spectroscopic measurements of charmonium produced from proton-antiproton annihilation have had some success, such as detailed measurements of the triplet P (χ) states.

Other states, notably the pseudoscalar ground state have been seen, but the width remains poorly measured. Pure hadronic decay of charmonium from $\bar{p}p$ annihilation remains largely unstudied. Specifically of interest in this thesis is the exclusive production of two vector mesons (e.g. $\omega\omega$, $\phi\phi$, and $\rho\rho$) from charmonium. These vector-vector systems can be produced from many $\bar{c}c$ bound states and thus may give us new or better measurements of several states in the $\bar{c}c$ spectrum, including the singlet states.

The most attractive system to explore is the $\phi\phi$. The ϕ is composed of $\bar{s}s$ and so has no overlap with the $\bar{p}p$ system. As with charmonium, $\phi\phi$ produced from $\bar{p}p$ must result from total annihilation. When omegas and rhos (composed of $\bar{u}u$ and $\bar{d}d$) are produced it is often the case that there are spectator quarks from the $\bar{p}p$ annihilation in the final state – i.e. $\phi\phi$ will not suffer the same degree of nonresonant continuum as the $\omega\omega$ or $\rho\rho$. Two issues, however, guide us to the $\omega\omega$ channel. First, without a magnet, $\phi\phi$ ($\phi \rightarrow K^+K^-$) is difficult to identify. Second, the neutral trigger, developed by the Northwestern High Energy Physics group (to which the author belongs), gives information on only neutral final states. The ω 's largest branching ratio to an all neutral final state is $B(\omega \rightarrow \pi^0\gamma) = 8.5\%$ whereas the ϕ 's largest branching ratio to an all neutral final state is $B(\phi \rightarrow \eta\gamma) = 1.3\%$. We investigated the possibility of measuring $\phi\phi$ via its decay to neutral final states, but found it impractical.

In chapter one, the history of the charm quark and charmonium is presented. The charmonium spectrum is reviewed as are some of the theoretical underpinnings of $\bar{c}c$ spectroscopy and spin dynamics. Next, E835's experiment methodology is described including the use of total $\bar{p}p$ annihilation for charmonium production and techniques for resonance scanning. Finally, the potential for $\omega\omega$ study to provide a better understanding of both charmonium dynamics and structure is discussed.

Chapter two provides a close look at the E835 detector and its operation starting with the collection of antiprotons in the Antiproton Accumulator. Next a description is given on how stochastic cooling and beam deceleration control were used to allow for production and scanning of exclusively produced $\bar{c}c$ bound states. The hydrogen gas jet target, the luminosity monitor, and the inner detectors for charged hadron and electron identification are briefly discussed. Chapter two emphasizes the lead glass calorimeter systems. They were essential as this $\omega\omega$ analysis looks into only the neutral final state decays of the ω ($\omega \rightarrow \pi^0\gamma$).

Chapter three includes a summary of the E835 data acquisition system with emphasis on the neutral trigger. The neutral trigger was not only essential in the $\omega\omega$ analysis, but it was also the responsibility of this author and the Northwestern High Energy Physics group to design, build, modify, maintain, and monitor it.

The description of $\omega\omega$ event selection is in chapter four. Preselection of $\omega\omega$ candidate events is followed by an in-depth evaluation of the $\omega\omega$ angular distribution and the insights it gives us into both resonant and nonresonant $\omega\omega$ production. The general form of the angular distribution is not published in the literature and was derived by the author specifically for this analysis. Subtraction of non- $\omega\omega$ background events is then described followed by a description of the efficiencies for detecting $\omega\omega$.

Chapter five contains the search for $\bar{c}c$ resonances in the $\omega\omega$ channel. Although no resonances were seen, nonresonant continuum was large, thus the angular distributions are examined for information about the continuum. It is shown that the continuum is dominantly pseudoscalar meaning that relative $\bar{p}p$ angular momentum $L = 0$ dominates the production channel. This information is used to obtain upper limits on the branching ratios, $B(\bar{p}p \rightarrow \bar{c}c) \times B(\bar{c}c \rightarrow \omega\omega)$, for pseudoscalar charmonium states (the η_c and η'_c). Since the resonant and nonresonant amplitudes for $\omega\omega$

production will interfere with a phase difference, δ , which is unknown, these upper limits are calculated over the full range of possible values. Finally, conclusions are offered as to how this analysis has improved our knowledge of charmonium production via $\bar{p}p$ annihilation as well as charmonium decay into two identical massive vector final states.

1.1 History

In the mid-20th century, the number of new particles uncovered in high energy physics experiments grew tremendously. By 1961, an emergence of patterns in the groupings of particles with similar attributes was evident. A landmark discovery, called the eightfold way, was proposed by Murray Gell-Mann [1].

The family of particles fell into distinct groups, called multiplets – some in groups of eight (octets) and others in groups of ten (decuplets). This classification paved the way for the next important step, the introduction in 1964 of quarks.

In 1964, Gell-Mann [2] and George Zweig [3] independently came up with an identical scheme: the zoo of particles would make more sense if the particles that reacted via the strong nuclear force were viewed as composites of yet another sub-atomic particle. In the original proposal, there were three species of such new constituents, named quarks – the up, down, and strange quarks. Quarks are spin $\frac{1}{2}$ fermions with fractional electrical charge. The up and down quarks (u and d respectively) are considered a doublet in a quantum number called isospin whereas the strangeness quantum number is unique to the strange quark.

In high energy e^+e^- colliders, the known point-like production cross section of $\mu^+\mu^-$ was compared to the hadronic production cross section. In the region above

10 GeV, away from any observed resonant states, the ratio R , given by

$$R = \frac{\sigma(e^+e^- \rightarrow \mu^+\mu^-)}{\sigma(e^+e^- \rightarrow \text{hadrons})} \quad (1.1)$$

was found to be fairly constant as a function of energy, justifying the argument (since $\mu^+\mu^-$ production by e^+e^- was understood to be point-like) that the hadronic production was also point-like – reinforcing the idea that hadrons are made up of quarks.

1.1.1 The Charm Quark

The first argument promoting the existence of a fourth quark was proposed, for purely esthetic reasons, by Sheldon Glashow and James Bjorken in 1964 [4]. By that time, it was well established that there were four types of leptons – the electron and its associated neutrino, and the muon and its associated neutrino. Glashow and Bjorken proposed a scheme in which a fourth quark, with similar quantum numbers to the up quark, filled the empty spot in the strange quark's doublet to complete the symmetry between the quark and lepton families.

$$\begin{pmatrix} u \\ d \end{pmatrix} \begin{pmatrix} ? \\ s \end{pmatrix} \longleftrightarrow \begin{pmatrix} e \\ \nu_e \end{pmatrix} \begin{pmatrix} \mu \\ \nu_\mu \end{pmatrix}$$

The most convincing argument, however, arose in an attempt to explain the absence of strangeness changing neutral currents in semileptonic weak decays. In 1963, Cabibbo [5] developed a theory that would explain the suppression of strangeness changing transitions ($\Delta S = 1$) in semileptonic weak decays as compared to the strangeness conserving transitions ($\Delta S = 0$). He arranged the known quarks, the u ,

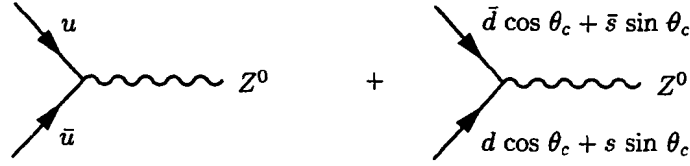


Figure 1.1: Neutral Current Coupling in Terms of the Cabibbo Doublet

d , and s , into a doublet containing the up quark and a state where the d and s were mixed via a rotation called the Cabibbo angle, θ_c . The lepton and quark doublets were then arranged as

$$\begin{pmatrix} u \\ d_c \end{pmatrix} = \begin{pmatrix} u \\ d \cos \theta_c + s \sin \theta_c \end{pmatrix} \longleftrightarrow \begin{pmatrix} e \\ \nu_e \end{pmatrix} \begin{pmatrix} \mu \\ \nu_\mu \end{pmatrix}$$

where the Cabibbo angle was approximately 0.25. In this model, the matrix element for neutral current coupling is (multiplying the Cabibbo quark doublet by its conjugate and separating out the neutral elements),

$$\underbrace{u\bar{u} + (d\bar{d} \cos^2 \theta_c + s\bar{s} \sin^2 \theta_c)}_{\Delta S=0} + \underbrace{(s\bar{d} + \bar{s}d) \sin \theta_c \cos \theta_c}_{\Delta S=1} \quad (1.2)$$

and thus, since θ_c is non-zero, shows the possibility of having strangeness changing neutral currents (see figure 1.1). As these reactions do not exist, a new model was needed.

In 1970, Glashow, John Iliopoulos and Luciano Maiani (GIM) proposed the introduction of a new quark with flavor labeled c for “charm” and a charge (matching the up quark’s) of $+2/3$ [6]. They proposed, for the quark states in weak interactions,

another doublet consisting of the c quark and the rotation of the s and d quark states that would be orthogonal to the d_c . Thus, the two quark doublets were

$$\begin{pmatrix} u \\ d_c \end{pmatrix} = \begin{pmatrix} u \\ d \cos \theta_c + s \sin \theta_c \end{pmatrix} \quad \begin{pmatrix} c \\ s_c \end{pmatrix} = \begin{pmatrix} c \\ -d \sin \theta_c + s \cos \theta_c \end{pmatrix}$$

The neutral current coupling from equation 1.2 is now modified to include diagrams from figure 1.2 and becomes

$$\underbrace{u\bar{u} + c\bar{c} + (d\bar{d} + s\bar{s})(\cos^2 \theta_c + \sin^2 \theta_c)}_{\Delta S=0} + \underbrace{(\overbrace{s\bar{d} + \bar{s}d - \bar{s}d - s\bar{d}}^{\equiv 0}) \sin \theta_c \cos \theta_c}_{\Delta S=1} \quad (1.3)$$

Notice that the strangeness changing part of the neutral current coupling drops out of the equation.

With the development of the GIM theory, the existence of the charm quark gained wide acceptance. It was necessary, then, to identify physical states that contained the charm quark. In 1974, Appelquist and Politzer [7] predicted that this theoretical charm quark should bind to its antimatter equivalent (the anticharm quark $-\bar{c}$) to produce $\bar{c}c$ pairs. In analogy to the well studied e^+e^- bound states (positronium), the system was called *charmonium*.

1.1.2 History of Charmonium

In 1974, separate groups lead by C. C. Ting at Brookhaven [8] and Burton Richter at SLAC [9] discovered a sharp resonance around 3.1 GeV. The Brookhaven group identified the resonance (which they called the J) in the e^+e^- invariant mass spectrum from the reaction $p + Be \rightarrow e^+e^- + X$. At SLAC, the particle was named the

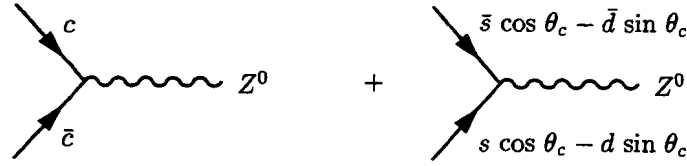


Figure 1.2: Diagrams for the Strange and Charm Contributions to the Neutral Current Coupling According to the GIM Mechanism

ψ and was discovered while examining the reaction $e^+e^- \rightarrow \text{leptons/hadrons}$. The discovery was soon confirmed by independent experiments and being that the SLAC and Brookhaven groups had simultaneously published their result in November, the particle was denoted the J/ψ .

The J/ψ was an electrically neutral, extremely heavy meson – more than three times the weight of a proton. But what made this particle so unusual was its extraordinarily long lifetime. Since e^+e^- annihilation predominantly proceeds via a virtual photon, the produced resonant state must have the quantum numbers of a vector particle ($J^{PC} = 1^{--}$). It was noticed that, for mass m and width Γ , all the known vector mesons (e.g. ρ , ω , and ϕ etc.) have Γ/m on the order of 0.1 to 0.001. The J/ψ had, however, lived very long (10^{-20} seconds) with Γ/m on the order of 10^{-5} . This was hard to reconcile with the existing models until it was proposed that the J/ψ was in fact made from a charm quark bound to its antiquark partner.

Based on the mass difference between the K_L^0 and K_S^0 , Gaillard and Lee [10] in 1974 had postulated that the charm quark mass (as a valence quark) should be about 1.5 GeV. This led to the explanation that the narrow width of the J/ψ was due to it lying below the open charm threshold. The lowest mass charmed mesons are the D mesons and so, since charm will be conserved in strong interactions, a

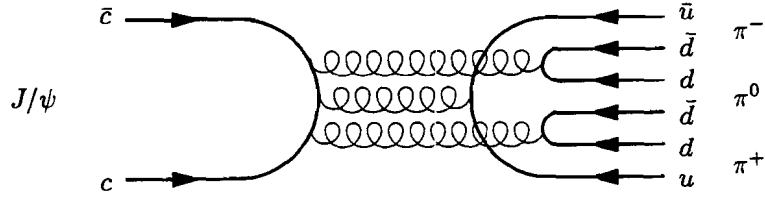


Figure 1.3: OZI Suppressed Decay of J/ψ to $\pi^+\pi^-\pi^0$

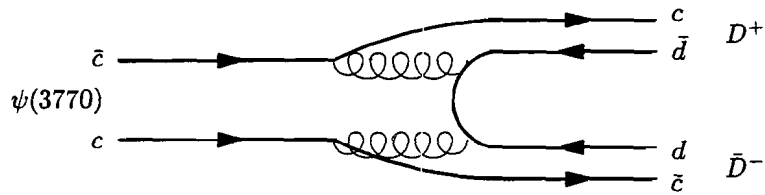


Figure 1.4: OZI Allowed Decay of $\psi(3770)$ to Two Charged D Mesons

charmonium state would need a mass greater than $2 \times m_D \approx 3.73$ GeV in order to decay to final state charmed hadrons (thus 3.73 GeV is the open charm threshold).

In the mid 1960s, Okubo, Zweig and Iizuka had developed the theory of OZI suppression [3, 11, 12]. This theory could explain the narrow width of the J/ψ since it was a charmonium state with mass below the open charm threshold, and so, it could not decay to final states containing charm quarks. OZI suppression simply says that reactions with diagrams containing disconnected quark lines will be suppressed compared to those that do not. In the J/ψ decay, the $\bar{c}c$ pair must annihilate into gluons (three, in fact, so that color and charge conjugation can be conserved) which must then materialize into quark pairs and finally hadrons. Charm states above the open charm threshold would be able to (and would prefer to) decay to charmed final states since the $\bar{c}c$ pair, although splitting up, could participate as spectators. This provides an easy mode – it is not OZI suppressed – which leads to

a larger phase space and so a larger decay width. Figures 1.3 and 1.4 show examples of an OZI suppressed and an OZI allowed charmonium decay, respectively.

1.1.3 The Charmonium Spectrum

Two weeks after the discovery of J/ψ another narrow state was discovered by the SLAC group [13]. This state was quickly identified as the first radial excitation of the J/ψ and was named the ψ' . Several additional charmonium states were identified in the next years. Figure 1.5 shows the current understanding of the charmonium spectrum near and below the open charm ($\bar{D}D$) threshold.

The vertical axis shows the mass or expected mass for the charmonium bound states for their different J^{PC} quantum numbers (horizontal axis). The states themselves are labeled by their given names and, in parentheses, their identifying spectroscopic notation, $n^{2s+1}L_J$, where s is the total quark spin, L is the magnitude of the quarks' relative angular momentum ($S = 0$, $P = 1$, etc.), $J = L + S$ is the total system angular momentum, and n is the radial excitation quantum number where $n = 1$ represents the ground state. Since charmonium is a fermion-antifermion system, its parity is given by $P = (-1)^{L+1}$, and its charge conjugation is given by $C = (-1)^{L+S}$.

After the discovery of the vector/triplet S states, the triplet P states, i.e. the χ states, were discovered in the radiative decays of the ψ' . The singlet states were more difficult to observe, but the η_c singlet S state and the singlet P wave state (the 1P_1) were claimed to be discovered and are currently awaiting confirmation.

The names of the states on the charmonium spectrum figure sit on lines representing their decay widths. The figure also shows the common decay modes for each particle. The D wave states have been observed but are not studied in this

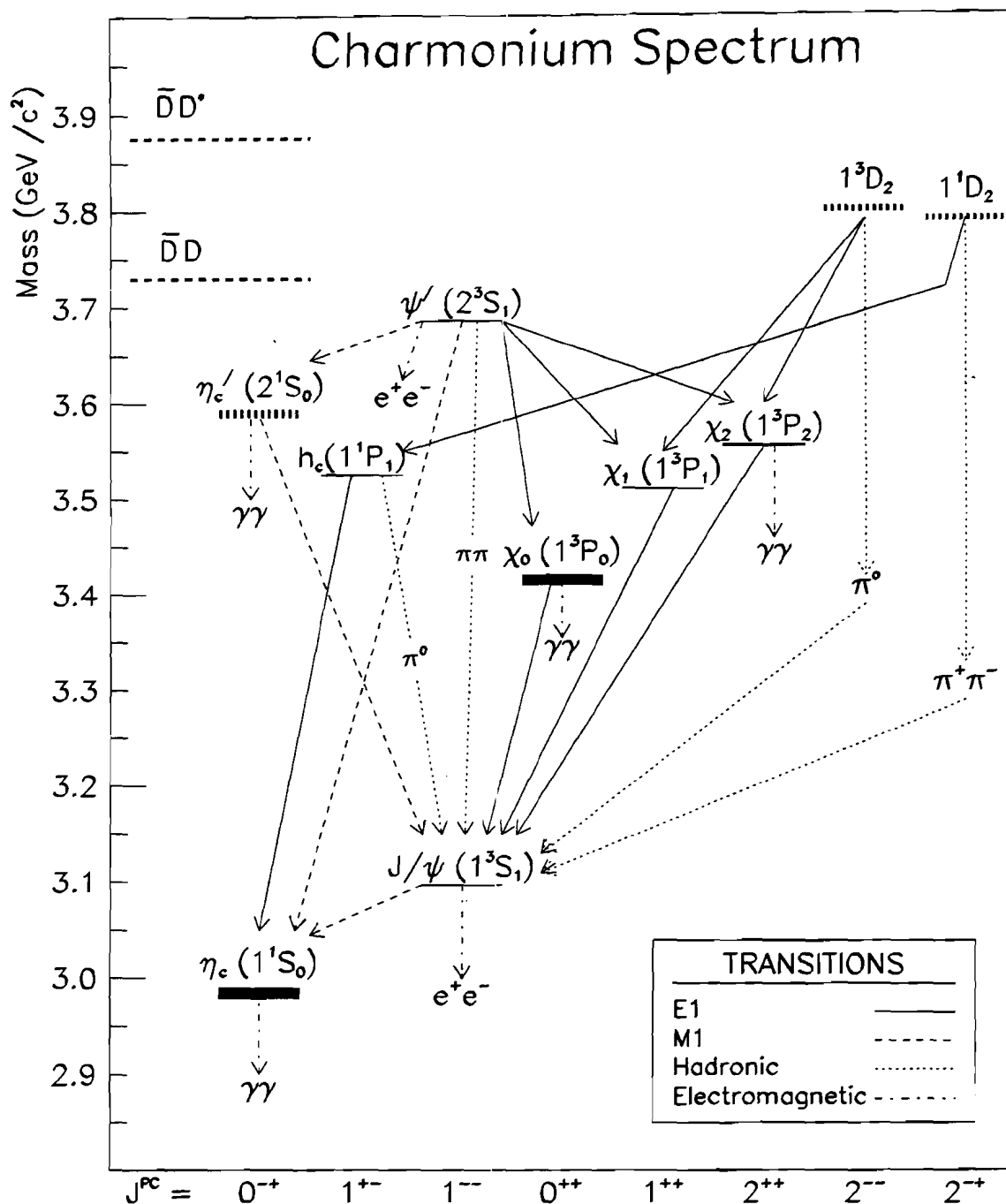


Figure 1.5: The Charmonium Spectrum

experiment and so are not discussed further.

1.2 Theoretical Motivation

A dynamical understanding of quark structure had its origins in 1968 with the study of deep inelastic lepton-neutron scattering experiments. This understanding was strongly reinforced by the results of e^+e^- annihilation to hadron studies at high energy, as well as the production of lepton pairs in hadron-hadron collisions.

The first high profile theory on quark-quark interaction was a model – proposed by Richard Feynman [14] – in which hadrons were composed of point-like and semi-free constituents called partons. The complicated process of lepto-production of multiple hadrons could be simply interpreted as (quasi) elastic scattering of the lepton by the partons. Experimental results indicated that partons have spin $1/2$ and fractional charge. The measurements of the ratio of the cross section for hadron production to that of lepton production in e^+e^- annihilation (see equation 1.1) demonstrated the point-like nature of hadron constituents and also gave evidence of a new quantum number for quarks – color.

The parton model, though successful in interpreting experimental results, is a phenomenological theory. It could not provide an understanding of the strong force which binds the quarks together inside hadrons. That partons account for only a fraction of the nucleon mass provided substantial evidence for the existence of gluons which form the basic constituents, along with these partons – identified with quarks – for the current standard model theory of the strong force, Quantum Chromodynamics (QCD).

1.2.1 Strong Force Interactions

QCD is a gauge theory of the strong force color interactions between quarks. Color is an internal degree of freedom analogous to charge in QED, and so, the gluon is analogous to the photon. The color flavor was introduced to avoid violation of the Pauli principle. When spin 3/2 particles had been discovered, the quark model seemed to conflict with the principle that multiple fermions can not exist in the same quantum state. That is, the only way to make a $J = 3/2$ state out of all u quarks (i.e. the Δ^{++}) is if they have the same quantum numbers. Introducing the color degree of freedom not only solved this puzzle, but experimentally was validated from the deep inelastic scattering experiments.

The color charge of a quark has three possible values – arbitrarily called red, blue, or green (r, b, or g). Antiquarks carry anticolor. The interquark interactions are assumed to be invariant under color exchange and are described by the symmetry group $SU(3)$. Since a quark can carry one of three possible colors, we can say that the quarks belong to the triplet representation of $SU(3)$. The massless vector bosons mediating the quark-quark interactions (gluons) are postulated to belong to an octet representation of $SU(3)$. To move color between quarks, the gluons must consist of a color-anticolor state. The 8 gluons are:

$$r\bar{b} \quad r\bar{g} \quad b\bar{g} \quad b\bar{r} \quad g\bar{r} \quad g\bar{b} \quad \frac{r\bar{r} - b\bar{b}}{\sqrt{2}} \quad \frac{r\bar{r} + b\bar{b} - 2g\bar{g}}{\sqrt{6}}$$

The color quantum number does not enter our description of hadrons, thus both baryons and mesons must be colorless (singlets) of $SU(3)$ color. If we write down the various contributions due to the exchange of gluons between quarks, the quark configurations of lowest energy are found to consist of the color singlet qqq state

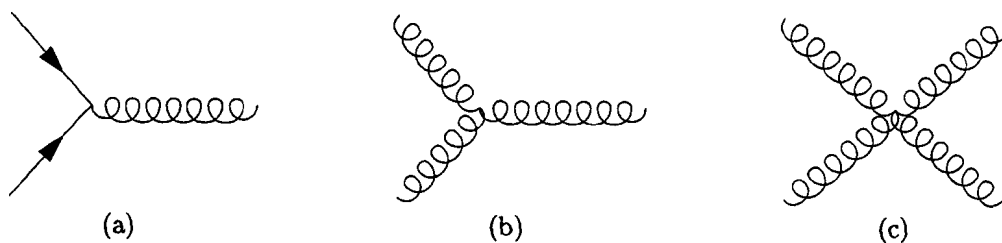


Figure 1.6: QCD Vertices for (a) qqg (b) ggg (c) $gggg$

(baryons) and the color singlet $\bar{q}q$ state (mesons). Other imaginable quark combinations (e.g., the $\bar{q}q$ octet) have weak, usually repulsive, binding. So, QCD predicts that only two of all the possible multi-quark combinations should exist in nature.

Though the photon and electric charge are similar in QED to the gluon and color charge in QCD, there is a peculiar and quite significant difference. In electromagnetism there are two types of charge and an uncharged mediating boson; in QCD there are six types of charge (color and anticolor) and a charged (i.e., colored) mediating boson. Therefore in electromagnetism, where the photon can only couple to electric charge, there is only one basic vertex. In QCD, the gluon couples to color charges on quarks or on other colored gluons, and hence, in addition to the fundamental quark-quark-gluon vertex (qqg), there will also be gluon-gluon vertices (see figure 1.6).

This additional direct gluon-gluon coupling makes QCD very different from QED and much more complex. It is essential, though, in explaining such things as the strong force coupling constant and in modeling the quark-quark interaction potential.

In QED it is well known that an electron will radiate and reabsorb photons, some

of which may temporarily become an e^+e^- pair. This pair produces a shielding effect on the electron as these pairs momentarily polarize. The closer to the electron another particle gets, the smaller this shielding effect becomes and thus the coupling gets stronger. The coupling constant for the strong force includes such a shielding effect due to a quark radiating a gluon which then produces a quark-antiquark pair. However, the non-Abelian nature of the strong force means that a radiated gluon may in fact couple to two or three gluons. This can negate (and even reverse) the effects of shielding leading to a strong coupling constant that *decreases* at close quark-quark distances. This is known as asymptotic freedom – that is, quarks at close distances behave as if they are semi-free. This leads to one of the largest problems in QCD study ... the coupling constant for low momentum transfer processes is large enough that perturbative QCD does not work. Thus, it is difficult to study the long range part of the QCD potential.

The QCD potential has been modeled phenomenologically from the charmonium spectrum in several different ways. Perhaps the most widely used is the Cornell potential [15], where for quarks separated at a distance r ,

$$V(r) = -\frac{4}{3} \frac{\alpha_s}{r} + kr \quad (1.4)$$

where α_s is the strong coupling constant, and k is described below. The $-1/r$ term should be recognized as a Coulombic potential and in fact represents single gluon exchange (the factor of $\frac{4}{3}$ comes from the requirement that the quark system must be colorless). This term dominates at short distances. At large distances, the r term dominates. This term represents multiple gluon exchange and by its nature indicates that at large distances the quark binding energy becomes increasingly large.

The confinement term, as it is called, shows that free quarks do not exist, and the strength of the term is described by k – typically taken to be around 1 GeV/fm.

Although the Cornell potential predicts the spin averaged spectrum well for heavy quarkonia, to find the structure due to the $\bar{q}q$ spin, e.g. the spacing among the triplet P states (fine structure) and between the triplet P and singlet P states (hyperfine structure), the Hamiltonian must be modified [16, 17]. The Breit-Fermi Hamiltonian [18, pages 336-347], including first order relativistic corrections (to first order in $(\frac{v}{c})^2$), now looks like

$$\begin{aligned}
 H = & \underbrace{\frac{p^2}{m} + V_v(r) + V_s(r)}_{H_0} \\
 & - \underbrace{\frac{p^4}{4m^3} + \frac{1}{4m^2} \left\{ \frac{2L(L+1)}{r} V'_v + [p^2, V_v - rV'_v] \right.}_{H_{SI}} \\
 & \left. + 2(V_v - rV'_v)p^2 + \frac{1}{2} \left(\frac{8}{r} V'_v + V''_v - rV'''_v \right) \right\}}_{H_{SI} \text{ cont.}} \\
 & + \underbrace{V_{SL} \langle \vec{L} \cdot \vec{S} \rangle}_{H_{SL}} + \underbrace{V_T \langle T_{12} \rangle}_{H_T} + \underbrace{V_{SS} \langle \vec{S}_1 \cdot \vec{S}_2 \rangle}_{H_{SS}}
 \end{aligned} \tag{1.5}$$

where p is the quark momentum, m is the quark mass, $V_v(r)$ is a vector-like potential, $V_s(r)$ is a scalar-like potential, L is the relative orbital angular momentum, S_i is the spin of the i^{th} quark, T_{12} describes the tensor spin term, and the prime indicates the derivative with respect to r . The H_0 term is the nonrelativistic zeroth order term and the first order terms include the spin independent correction, H_{SI} , and the spin dependent terms, H_{SL} , H_{SS} , and H_T . These last terms describe the spin-orbit, tensor, and spin-spin interactions, respectively. Note the following definitions

used above

$$\begin{aligned}
 V_{SL} &= \frac{1}{2m^2r}(3V'_v - V'_s) \\
 V_T &= -\frac{1}{m}(V''_v - \frac{V'_v}{r}) \\
 V_{SS} &= \frac{2}{3m^2}(\nabla^2 V_v)
 \end{aligned} \tag{1.6}$$

The expectation values from equation 1.6 are given by

$$\begin{aligned}
 \langle \vec{L} \cdot \vec{S} \rangle &= \frac{1}{2}[J(J+1) - L(L+1) - S(S+1)] \\
 \langle T_{12} \rangle &= \left[-\langle \vec{L} \cdot \vec{S} \rangle^2 - \frac{1}{2}\langle \vec{L} \cdot \vec{S} \rangle + \frac{1}{3}\langle \vec{L}^2 \rangle \langle \vec{S}^2 \rangle \right] / [(2L+3)(2L-1)] \\
 \langle \vec{S}_1 \cdot \vec{S}_2 \rangle &= \frac{1}{2}[S(S+1) - \frac{3}{2}]
 \end{aligned} \tag{1.7}$$

Obviously, the short range Coulombic type one gluon exchange is in $V_v(r)$. The multiple gluon long range potential may have a vector-like component – which would be included in $V_v(r)$ – but must also have a nonvector-like component, contained in $V_s(r)$ [19].

1.2.2 Charmonium Study

A two-body bound state offers the simplest system to study the underlying forces that bind the system together. One of the simplest and most instructive two-body bound state systems to study are the *onia*. Those are the bound states of a funda-

mental particle and its antimatter equivalent. These states are among the simplest to test theoretical predictions on since they have point-like structure, minimal particles involved, and in the ground states will often involve the minimum complexity of gauge boson exchange. These conditions make calculating the matrix elements for the inevitable annihilations relatively easy. They can have complex structures with spin that can provide insight into the interaction potential without unnecessary complexity in the mathematics.

The first onium extensively studied both theoretically and experimentally was the e^+e^- bound state called positronium [20]. The study of positronium has aided in developing a successful quantum field theory for the electromagnetic force (Quantum Electrodynamics). In a similar way, it is desirable to study systems of quarks and antiquarks, quarkonia, to investigate the fundamental properties of the strong force and test our current QCD model.

The strong force is considered flavor independent so that any quarkonia system can be studied and the results will hold true for all systems. It might naively seem, then, that the light quarkonia states would be ideal for experimentation. They are easy to form and detect – much more so than the heavy quarkonia systems. Cross sections for formation fall dramatically with increasing quark mass.

In reality, however, heavy quarkonium has many advantages. First, the quarkonia comprised of light quarks form a highly relativistic system. This complicates the Hamiltonian. Charmonium is only semi-relativistic and in fact the non-relativistic treatment has been quite successful. Consider, however, the virial theorem from which the expectation value of the kinetic energy, $\langle T \rangle$ is

$$\langle T \rangle = \frac{1}{2} \langle \vec{r} \cdot \vec{\nabla} V(\vec{r}) \rangle \quad (1.8)$$

Assume that the mean radius of the charmonium is predominately linear in r , so that $\langle T \rangle = \frac{1}{2}\langle V \rangle$. Then, with the binding energy for the $\bar{c}c$ system, E_b , given by $E_b = \langle T \rangle + \langle V \rangle$ and using the non-relativistic expression $\langle T \rangle = 2(\frac{1}{2})m_c\langle v^2 \rangle$, the mean square of the velocity is

$$\langle v^2 \rangle = \frac{E_b}{3m_c} \quad (1.9)$$

Using the rough estimate of the charm quark mass of 1.5 GeV and taking the 673 MeV mass difference between the J/ψ and the ψ' as the binding energy, the mean square velocity of the $\bar{c}c$ pair is, $\langle v^2 \rangle \approx 0.15$ GeV. This shows that relativistic effects can not be neglected completely.

The light quarks are similar in mass and since they decay readily to the lightest hadrons (there is no OZI suppression) they have short life times. The mixing of the $\bar{u}u$, $\bar{d}d$, and $\bar{s}s$ states, along with their large widths, causes crowding and a large degree of overlap in the light quark spectrum. This makes their study problematic. Figure 1.7 shows many of the light quarkonia states with their widths represented by the hash marks at their masses.

On the other hand, due to OZI suppression, charmonium states below the open charm threshold are very narrow as compared to their mass separation (refer to figure 1.5). In addition, the other quark masses differ enough that there is no non-charm quarkonia present to confuse identification. Thus charmonium states below the open charm threshold are accessible and clearly identifiable, and, as quarkonia cross section falls rapidly with quark mass, charmonium is a compromise between light quarkonia and bottomonia study.

Charmonium spectroscopic study can, therefore, allow insight into many of the specifics of QCD and the strong force. For example, how Coulomb like is the short range part of the potential? If we consider a pure Coulomb type vector interaction

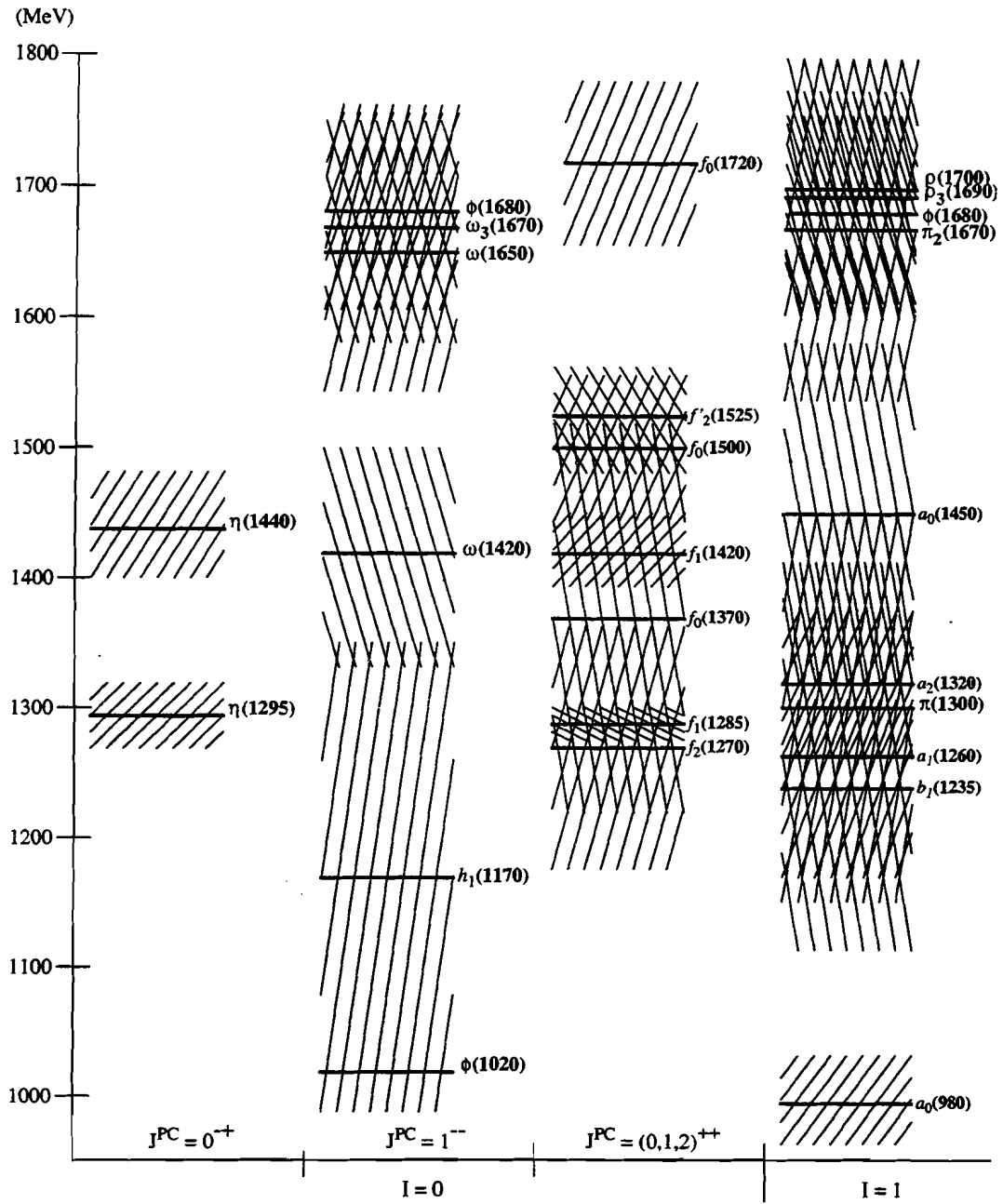


Figure 1.7: Overlap of Light Quarkonia States [21]. The width of the state is represented by the hash marks at its mass.

between quarks at close distances, i.e. $V_v \propto -\frac{1}{r}$, then V_{SS} in equation 1.7 becomes proportional to $\frac{\vec{S}_1 \cdot \vec{S}_2}{9m_1 m_2} \delta(\vec{r})$. The delta function implies that the only nonzero matrix elements are between S-wave states (e.g. the η_c and J/ψ exhibit a hyperfine splitting).

The implication is that for $L \neq 0$ the hyperfine splitting should be zero. In the case of the triplet P and singlet P states for instance, the singlet P should be at the center of gravity of the triplet P states. The identification of the 1P_1 is, therefore, of great interest.

In addition, in the limit of a pure Coulomb type interaction, the 2S and 1P levels become degenerate, leptonic widths for nS levels (dependent on $|\Psi(0)|^2$) become proportional to n^{-3} , and the 1S and 2S level spacings should grow with increasing quark mass (the energy levels are proportional to the reduced mass in the Coulomb potential). Comparison of these properties for $\bar{b}b$ and $\bar{c}c$ will also provide insight into the true flavor dependence of the quarks on the strong force (other than the obvious quark mass “flavor” dependence).

There are many more questions we hope to gain insight into, such as, can we determine the Lorentz structure of the confinement term? That is, is it truly composed of a vector and scalar contribution and nothing else? Is the tensor force term the result of an anomalous “magnetic moment” of the gluon color coupling to quarks? How does the strong coupling constant run?

1.3 E835 Experiment Technique

Charmonium study via $\bar{p}p$ annihilations was pioneered by CERN ISR experiment R704 in the early 1980s. R704 was able to directly observe some of the nonvector charmonium states created through use of a cooled \bar{p} beam interacting with a hy-

drogen gas jet target allowing direct production of the η_c , χ_1 , and χ_2 for the first time [22, 23, 24]. A two arm spectrometer was used to identify charmonium via electromagnetic final states.

Not long after the completion of R704 in 1984, experiment E760 at the Fermilab Antiproton Accumulator was commissioned (data taking was from 1994-1995). E760 [25, 26] and its successors, E835 [27] which took data in 1996-1997 (and is the subject of this thesis), and E835 phase two which took data in 1999-2000, followed in the same tradition as R704. Precise measurements of all charmonium states except the η'_c and 1P_1 were made by this trilogy of Fermilab experiments.

1.3.1 Production of Charmonium

Charmonium is produced primarily by one of three methods: e^+e^- annihilation (figure 1.8), $\gamma\gamma$ fusion (figure 1.9), or hadron scattering/annihilation. Hadron scattering/annihilation includes such processes as $\bar{p}p$ annihilation and partial annihilation, and proton-nucleon scattering. If we consider $\bar{p}p$ collisions, specifically, the process can be classified by the degree of quark-antiquark annihilation as follows:

1. Class 0 – All six quarks are spectators (rearrangement is possible, e.g. $\bar{p}p \rightarrow \Delta\bar{\Delta}$).
2. Class 1 – Four quarks are spectators, two annihilate. This is the process occurring in very high energy colliders, e.g. CDF and D0 at Fermilab.
3. Class 2 – Two quarks are spectators, four annihilate.
4. Class 3 – All six quarks annihilate ... total $\bar{p}p$ annihilation.

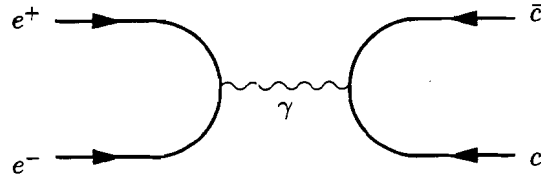


Figure 1.8: e^+e^- Annihilation Producing Charmonium via a Virtual Photon

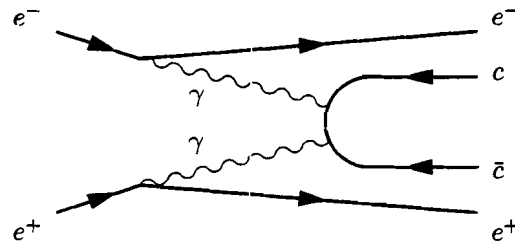


Figure 1.9: Production of Charmonium via $\gamma\gamma$ Fusion

Total $\bar{p}p$ annihilation as is attempted in this experiment (class 3) is shown as figure 1.10. The other classes mentioned above are important as nonresonant continuum and are addressed in chapter 4.

The bulk of detailed information on charmonium initially came from the study of e^+e^- annihilations. The greatest advances in charmonium study in the past have come from SLAC experiments using the Mark I, Mark II, Mark III, and Crystal Ball detectors.

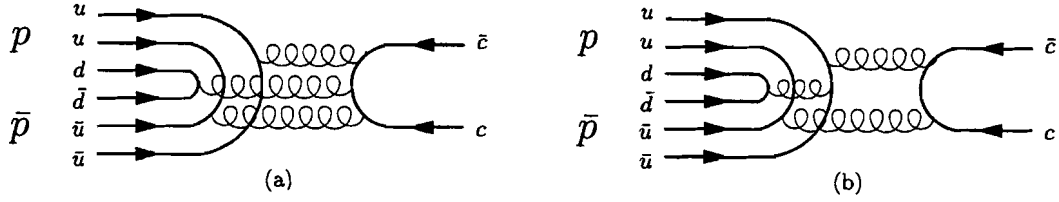


Figure 1.10: $\bar{p}p$ Annihilation Producing Charmonium via (a) 3 Gluons and (b) 2 Gluons

Charmonium produced from e^+e^- annihilation has the disadvantage that, since the e^+e^- system couples to the final state through a virtual photon, only vector states ($J^{PC} = 1^{--}$) can be directly formed, e.g. the J/ψ and the ψ' . Other charmonium states must then be observed through a secondary decay, such as the radiative transition of the ψ' . The 1P_1 would need to be observed through yet another radiative decay as the ψ' cannot directly transition to it.

In studying a particle from a radiative transition, the mass resolution depends primarily on how well the photon can be detected (i.e. the energy resolution of detector which is often quite large). In addition, the large e^+ and e^- beam energy spreads (due to bremsstrahlung radiation) are much greater in the center of mass than are the widths of the J/ψ and ψ' . This makes the direct measurement of the width impossible and instead the width must be measured by calculating the area under the final state particle's excitation curve. This makes the width measurement dependent on the detector acceptance and efficiency.

Fusion of two photons, constrained by charge conjugation conservation, is limited to producing only C even states, e.g. the η_c , η'_c , and χ states. Again, other states must be observed through secondary decays, limiting the mass resolution by the

resolution of the detector.

The creation of charmonium via $\bar{p}p$ annihilation circumvents most of these issues. Charmonium production from $\bar{p}p$ annihilation proceeds through either two or three gluon exchange¹. Thus, all $\bar{c}c$ states are directly accessible. This means that the mass resolution of the charmonium state depends primarily on the beam parameters and that the width can be directly measured. This is a great benefit to charmonium study since the beam spread can be made very small and knowledge of the beam energy can be very large.

In addition, since the proton is much more massive than the electron (by over three orders of magnitude), the radiative corrections are very small. Thus, the widths can be inferred directly from the excitation curve.

The main disadvantage of this method is the relatively large $\bar{p}p$ annihilation cross section, about 70 mb at charmonium energies, while the expected charmonium formation cross sections are at picobarn to nanobarn levels. It is thus necessary to construct a detector and experimental technique that can extract the small charmonium signals from the large hadronic background.

1.3.2 Resonance Scanning

E760 and E835 operated with the same technique – antiprotons incident upon a hydrogen gas jet target. A beam of stochastically cooled antiprotons were brought to a momentum corresponding to a desired center of mass energy (below the open charm threshold). The detector, optimized to detect electromagnetic final states, recorded events that may be of interest in our studies. As the beam momentum could be easily lowered by decelerating the beam, a charmonium resonance could be

¹One gluon mediation is not allowed since this would violate the principle that hadrons are colorless.

scanned by systematically taking data at intervals in energy about the state's mass.

The charmonium resonant parameters were determined from the scan by measuring the desired final state cross section as a function of \bar{p} center of mass energy. The observed excitation curve, $S(E)$, is a convolution of the beam energy distribution, $B(E)$, and a Breit-Wigner curve corresponding to the resonant production, $\sigma_{BW}(E)$,

$$S(E) = \int_0^\infty \sigma_{BW}(E')B(E - E')dE' \quad (1.10)$$

The Breit-Wigner cross section is given by,

$$\sigma_{BW}(E) = \frac{2J + 1}{(2S_1 + 1)(2S_2 + 1)} \cdot \frac{4\pi}{p^2} \cdot \frac{B_{in}B_{out}\Gamma_R^2/4}{(E - m_R)^2 + \Gamma_R^2/4} \quad (1.11)$$

where E is the center of mass energy, J is the spin of the resonance, S_1 and S_2 are the spin of antiproton and proton, $p = \sqrt{E^2/4 - m_p^2}$ is the momentum of the proton or antiproton in the center of mass frame, m_R and Γ_R are the mass and width of the charmonium resonance, and B_{in} and B_{out} are the branching ratios of the charmonium formation and decay channels.

With this scanning method, the parameters of the resonance can be very precisely determined since the mass resolution will primarily depend on the accuracy of the beam momentum and the width will depend primarily on the beam spread.

1.4 Production of $\omega\omega$

The ω is a $\bar{u}u$ and $\bar{d}d$ mixed state with quantum numbers $J^{PC} = 1^{--}$, that is, it is a massive vector particle. The mass and width are given by the PDG as 781.94 ± 0.12 MeV and 8.41 ± 0.09 MeV respectively. The ω and the ρ are the lightest vector hadrons known with the ω being the isospin 0 manifestation and the ρ being the orthogonal isospin 1 manifestation.

The ω , like other light quark bound states of identical vector hadrons, is accessible through many intermediate angular momentum states. In fact, any physical state with even charge conjugation quantum number is accessible to $\omega\omega$. This system may provide a consistent way to probe the charmonium spectrum including the possibilities of examining all the χ states, the η_c , and perhaps even discovering the η'_c . If the η_c can be observed in this mode, this channel could provide a new way to see the singlet P $\bar{c}c$ bound state in the reaction $^1P_1 \rightarrow \gamma\eta_c \rightarrow \gamma\omega\omega$ since the radiative decay of the 1P_1 to the η_c should be a favored decay.

No charmonium resonance has yet been observed to decay to $\omega\omega$ and an upper limit has only been placed on the η_c decay at a branching ratio less than 0.3%. It is interesting then that both the $\rho\rho$ and $\phi\phi$ (the ϕ being the lowest mass vector meson composed of $\bar{3}s$) have been observed in the η_c decay – the $\phi\phi$ having a branching ratio of $(0.71 \pm 0.28)\%$ and the $\rho\rho$ having a branching ratio of $(2.6 \pm 0.9)\%$. It is not known why the $\omega\omega$ should be so much smaller than the $\phi\phi$ or $\rho\rho$.

Consider the class 3 subprocesses in figure 1.11 where (b) results in a color octet that is assumed to become singlet under a final state gluon exchange. $K^*\bar{K}^*$ (the K^* is a vector meson composed of $d\bar{s}$) can not come from (b) and, for example, $\phi\omega$ can only come from (b), whereas $\omega\omega$, $\phi\phi$, and $\rho\rho$ can result from all three. Calculations [28] suggest that (b) is suppressed as the $\phi\phi$ is not the dominant decay

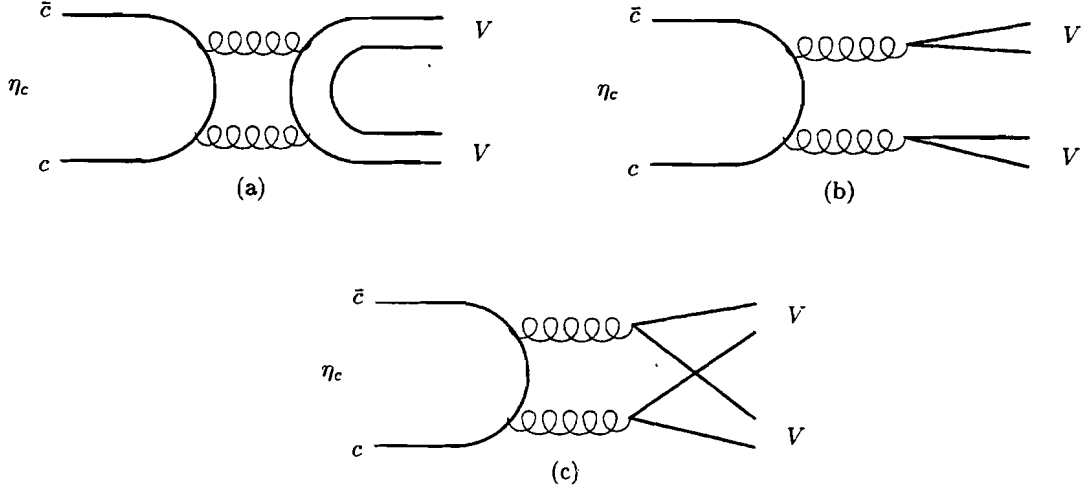


Figure 1.11: Mechanisms for η_c Decay to Two Mesons. Note (b) results in a color octet that is assumed to become singlet under a final state gluon exchange.

mode. Once the $\omega\omega$ is measured we will be closer to an understanding of how these processes contribute to η_c decay and this may give us insight into the differences in the branching ratios of charmonium to vector-vector mesons.

Since the E835 detector was designed to detect neutral final states to great precision, but has no magnet and so was not so adept at identifying charged pions, each ω was identified through its M1 decay to a neutral pion instead of the more copious $\omega \rightarrow \pi^+\pi^-\pi^0$ channel. The neutral trigger, described in chapter 3, is well suited for this task, however.

The PDG value for the branching ratio $B(\bar{p}p \rightarrow \eta_c)$ is 1.2×10^{-3} and using the upper limit for $\omega\omega$ production via η_c , $B(\eta_c \rightarrow \omega\omega) < 3.1 \times 10^{-3}$, the peak cross section if one uses equation 1.11 is less than 24 pb. This is a small cross section for E835 detection, but with a large nonresonant continuum, interference will play

a role and has the potential to pump up the signal.

Note that a subgroup of E835 has detected η_c in $\phi\phi$ at roughly twice the $\omega\omega$ branching ratio upper limit. It benefitted from low background and nonresonant continuum and the large subsequent branching ratios $B(\phi \rightarrow K^+K^-) = 49.1\%$, but the amount of data was small enough so as to limit the amount of knowledge we could gain for general vector-vector channels.

Chapter 2

Experiment Apparatus

The E835 apparatus consists of the Antiproton Ring, a hydrogen gas jet target, and the E835 detector. The production of a narrow momentum spread \bar{p} beam and the ability to accurately place that beam at a desired center of mass energy was essential as the experiment was designed to search for charmonium resonances directly produced from $\bar{p}p$ total annihilations. That is, the experiment's ability to resolve charmonium states depended primarily on knowledge of the beam parameters. The detector itself, which features a Pb glass calorimeter, is optimized for the identification of electromagnetic final states in order to extract the pb to nb cross sections from the much larger 70 mb hadronic background.

2.1 The Antiproton Ring

A schematic of the \bar{p} production and accumulation system [29, 30] is shown as figure 2.1. The system was designed to stochastically cool and accumulate antiprotons for use in Tevatron $\bar{p}p$ collisions. During the periods of fixed target running, how-

ever, the created and accumulated antiprotons were dedicated primarily for E835 use.

2.1.1 Antiproton Accumulation

The \bar{p} beam construction begins when H^- ions are accelerated by a Cockroft-Walton accelerator to 750 keV. The ions are injected into the 150 m long linear accelerator where they reach 200 MeV before passing through a carbon foil to strip them down to bare protons. The protons are injected into the 500 m circumference booster synchrotron and accelerated to 8 GeV.

The next step is injection of the protons into the Main Ring synchrotron (6.3 km circumference) where they reach an energy of 120 GeV. The protons then collide with a Tungsten target to produce a fairly flat momentum distribution of 8-9 GeV/c antiprotons (along with other negatively charged particles) which are then focused with a 1 cm radius, 15 cm long, lithium lens exerting a 750 T/m azimuthally symmetric magnetic field. The field causes the particles which are not antiprotons to be ejected from the beam pipe.

After focusing, the antiprotons enter the debuncher which has a momentum aperture of about 8% centered at 8.9 GeV/c where the cross section of 120 GeV protons colliding with the Tungsten is maximum. At this time there are 82 1.5 ns bunches with separation by 18.9 ns entering the Debuncher every 2 seconds. This is about 2×10^{12} protons every two seconds. The beam is RF rotated in phase space to make it small in ΔE and large in Δt (i.e. debunched). At this time the \bar{p} momentum spread is $\pm 2\%$. It is then longitudinally and transversely cooled (\bar{p} momentum spread decreases to $\approx 0.085\%$) and is brought into the smaller circumference Accumulator where it is RF bunched and decelerated into a smaller

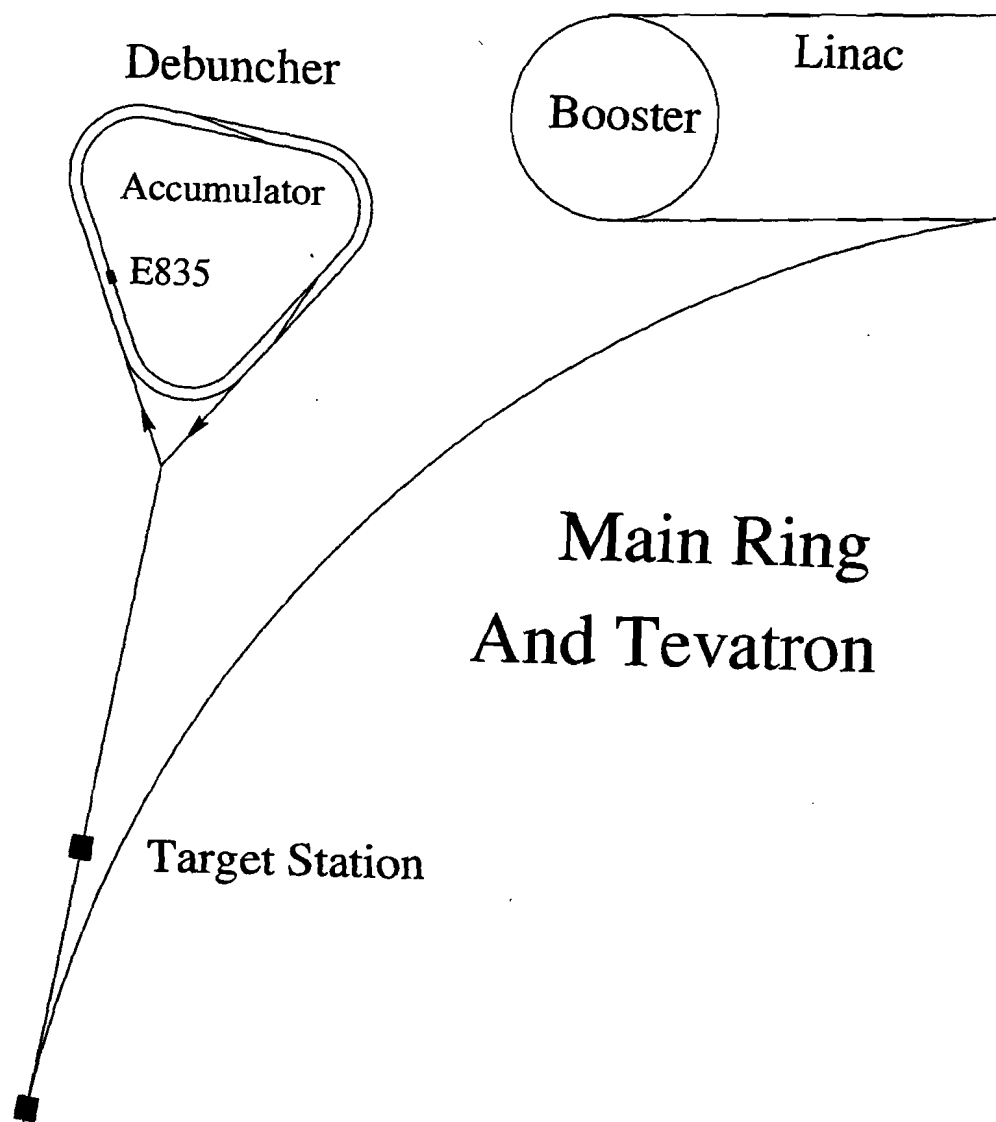


Figure 2.1: Antiproton Ring

orbit to move out of the way of the next bunch. In the Accumulator, the \bar{p} beam is further cooled to bring the momentum spread down to 0.02%. This accumulation is known as stacking.

The stochastic cooling system uses pick-up electrodes to monitor the path of the antiprotons and applies an RF kick to correct for spreading out of the momentum transversely. In high dispersion regions the transverse and longitudinal spreads are correlated allowing for longitudinal cooling as well.

The typical accumulation rate is about 3 mA/hour ($1 \text{ mA} \approx 10^{10}$ antiprotons). For E835, the typical stack size was from 20-80 mA depending on the center of mass energy at which we desired to run¹. In general, 80 mA was the upper limit that could be stably cooled and decelerated.

After stacking was complete and more cooling brought the \bar{p} beam to a reasonable momentum width, deceleration could begin. It would typically take 30 minutes to 2 hours after which time the gas jet was turned on and data taking began.

As the circulating \bar{p} beam repeatedly interacted with the hydrogen gas jet target as well as with residual gas in the beam pipe, the emittance of the beam would tend to increase, thus causing beam loss. The stochastic cooling continually worked to offset this effect. From large angle scattering, however, beam loss was inevitable. For E835 running, the beam loss half-life for a typical 40 mA stack was between 25 and 45 hours depending on the beam energy. With the jet off, the beam half-life rose to about 200 hours.

¹Large current beams tended to be wide and thus unstable during decelerations. For long decelerations (to lower energies) we therefore used smaller stacks.

$\bar{c}c$ State	Mass (GeV/ c^2)	P_{beam} (GeV/c)
η_c	2983	3686
J/ψ	3097	4066
χ_0	3417	5200
χ_1	3511	5552
1P_1	3526	5609
χ_2	3556	5724
η'_c	3594	5871
ψ'	3686	6232

Table 2.1: \bar{p} Beam Momentum Required for Particular Center of Mass Energies. The mass given for the η'_c is the median of the E835 search energies.

2.1.2 Beam Deceleration

For E760 running, the Accumulator was modified to allow deceleration of the \bar{p} beam to a momentum such that upon collision with our protons a particular center of mass energy could be obtained (see table 2.1).

The beam deceleration minimum step is determined by the least significant bit of the digital dipole power supply, approximately 150 keV/c in the lab (50 keV/c in the center of mass). Decelerations took on average 1 second per 20 MeV. At the end of the deceleration the beam was debunched and cooled further until it was about 95% contained in a 5 mm diameter. By the time data taking was about to begin, the beam had a momentum spread, σ_p/p , of about 2×10^{-4} .

The revolution frequency of the beam is determined from the beam current Schottky noise [31, detailed discussion in chapter 3]. The Schottky noise is the sum of individual pulses detected from the passage of beam particles through a coaxial quarter-wavelength pickup. If $1/T$ is the revolution frequency of an individual charged particle and t_0 is its phase so that it passes through the pickup at time $t_0 \pm nT$, then the single particle frequency spectrum (the Fourier transform of the

current) will be

$$\tilde{I}(f) = ef_0 \exp(-2\pi i f t_0) \sum_{n=-\infty}^{\infty} \delta(f - n f_0) \quad (2.1)$$

with $f_0 \equiv 1/T$. In reality, for N particles, when the currents from all the particles are summed (with the phases t_0 randomly distributed and allowing for small variations in particle frequencies), the delta functions are smeared into Schottky noise bands with frequencies $n(f_0 \pm \delta f)$. The amplitudes of the Schottky bands are proportional to the number of antiprotons traveling at that frequency. Thus, after the quarter-wavelength pickup acquires the Schottky noise spectrum, a spectrum analyzer can record the power spectrum, $P(f)$, and from the relation

$$P(f) \propto (ef)^2 \frac{dN}{df} \quad (2.2)$$

the beam frequency spectrum can be determined [32]. A typical frequency spectrum is shown as figure 2.2. Notice that the vertical scale is in powers of ten (dB) so that the tail is in fact quite small compared to the peak. These spectra were read out every three minutes during data taking and the average of all the spectra during a run was used as the beam distribution for that run. A run ended when the first tape of a set of 8mm tapes fills (each tape receives data from a particular stream – see chapter 3). This was usually on the order of three to six hours. Blank tapes were then loaded and the next run began. This was repeated until it was deemed that the beam was small enough to be dumped and thus stacking would begin again².

The \bar{p} beam frequency was approximately 0.62 MHz and was calculated to better than one part in 10^7 .

²At a small enough beam current the gas jet density could no longer be raised enough to keep luminosity constant. This usually happened around 12 mA.

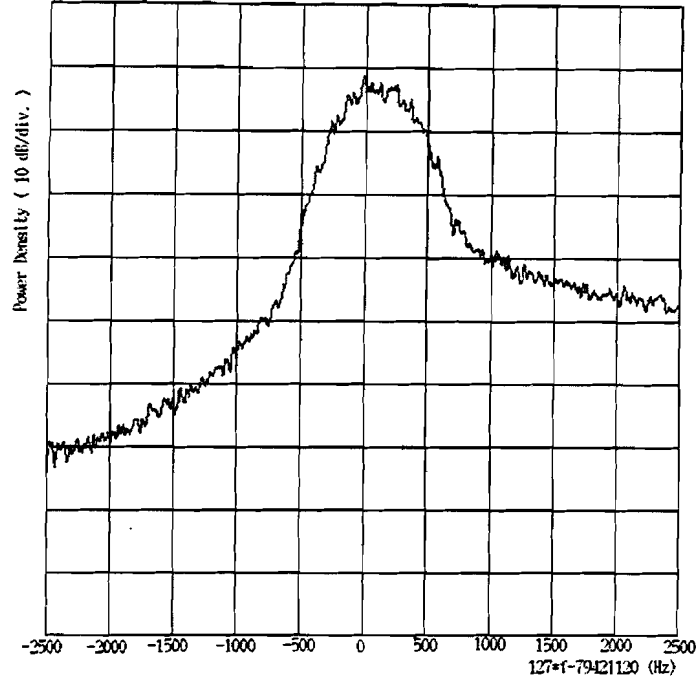


Figure 2.2: Schottky Power Spectrum at $\sqrt{s}=3686$ MeV. The resolution is about 30 Hz. The vertical scale is 10 db/div.

The beam momentum distribution, dp/p , can be calculated from the relation

$$\frac{dp}{p} = -\frac{1}{\eta} \frac{df}{f} \quad (2.3)$$

where $\eta \equiv 1/\gamma_t^2 - 1/\gamma^2$ is called the slip factor, $\gamma = E_{beam}/m_p$, and γ_t is characteristic of the accumulator lattice. Decelerations crossing this γ_t transition were prone to large beam loss since beam instability near $\gamma = \gamma_t$ is large. During E835 running, the transition energy was near enough to the χ_0 to hinder, but not prevent, data taking there.

The \bar{p} beam energy is determined from beam revolution frequency, f , and orbit length, L , according to the equation

$$E = \frac{m_p}{\sqrt{1 - \beta^2}} \quad (2.4)$$

where the velocity of the beam, β , is given by $\beta = fL$. From equation 2.4 the error on the energy is

$$\frac{\delta E}{E} = \beta^2 \gamma^3 \frac{\delta \beta}{\beta} = \beta^2 \gamma^3 \left(\frac{\delta L}{L} + \frac{\delta f}{f} \right) \quad (2.5)$$

As stated above, the error on the revolution frequency is better than 1 part in 10^7 . It turns out that the energy error is dominated by the error on the orbit length.

Initially, the central orbit (i.e. the orbit passing through the centers of all the quadrupole magnets) was determined by a survey to be 474 m but with an accuracy that was not good enough for our purposes of measuring the very narrow widths of the J/ψ and ψ' . For a more accurate estimation, we instead calibrated the orbit length from a reference orbit at the ψ' .

The ψ' mass is known very precisely to be 3686 ± 0.1 MeV [33]. The reference orbit measurement was started by decelerating the beam to an energy safely above the ψ' mass. Then e^+e^- data was taken as the beam was stepped down in energy until the peak of the ψ' was found. From the known ψ' mass, we can determine what the beam momentum must have been to give us that mass (see, for example, table 2.1), and thus we could determine β for the beam at the peak. We know what the frequency of the beam was when we were at the peak, so, from the definition of β , the equation $M_{\psi'}^2 = 2m_p^2(1 + \gamma)$, and the known ψ' mass and error, we can determine the orbit length and its error,

$$\frac{\delta L}{L} = \frac{M_{\psi'} \delta M_{\psi'}}{m_p^2 \beta^2 \gamma^3} \quad (2.6)$$

to be $474.05 \text{ m} \pm 0.70 \text{ mm}$. The error on the revolution frequency was small enough

to be neglected in the calculation. At other beam energies, the orbit length was calculated by measuring the deviation, ΔL , of the orbit length from the reference orbit using the 48 beam position monitors (BPMs) along the beam line. The error on this deviation was about ± 1 mm so that the overall error on the orbit length was $\sqrt{\delta L^2 + 1 \text{ mm}^2} \approx 1.2$ mm which translated to a systematic error on the ψ' mass of about 150 keV and on the J/ψ mass of about 50 keV.

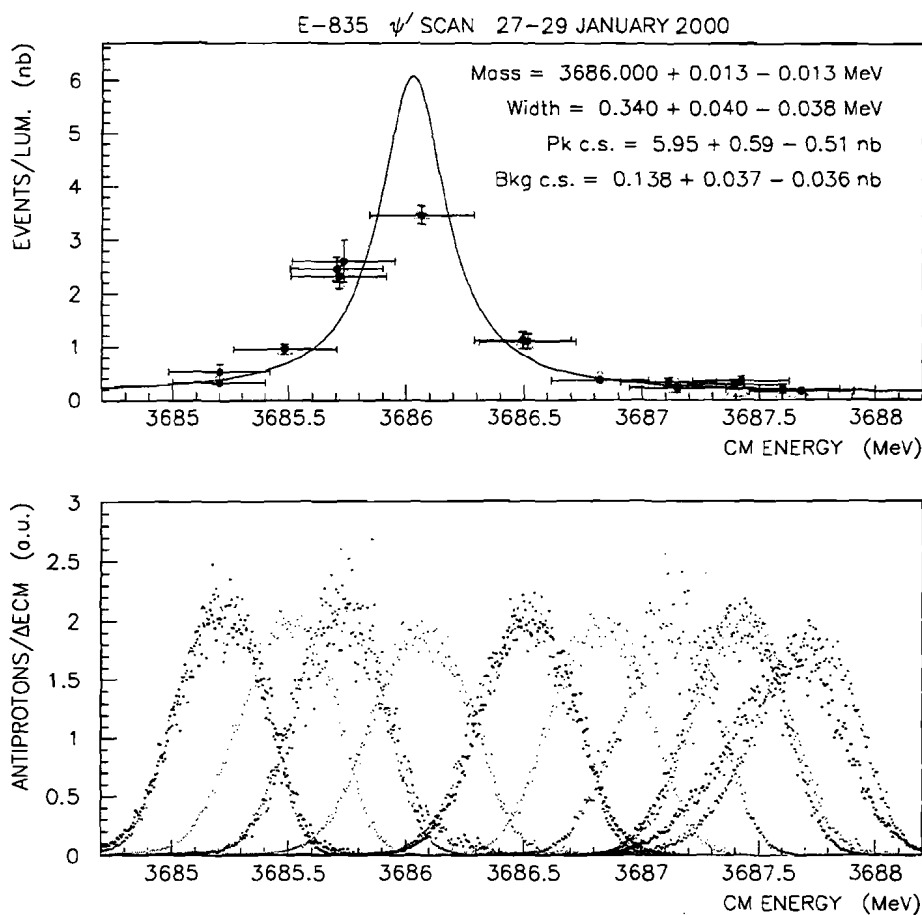


Figure 2.3: Typical ψ' Scan

An example of a ψ' scan is shown in figure 2.3 [34]. The data points on the top plot correspond to the cross section measured at each center of mass energy. The bottom plot shows the beam energy distribution at each point in the deceleration (the target energy is the peak of each distribution). After taking data (in this case e^+e^-) for a time at one energy, the beam was decelerated to the next lower energy. The curve on the top plot is the data deconvoluted from the beam shape. So essentially, how well we determine the mass and width of narrow states depends on how well we know the beam energy and spread (and statics, of course), not on the resolution of the detector.

2.2 The Hydrogen Gas Jet Target

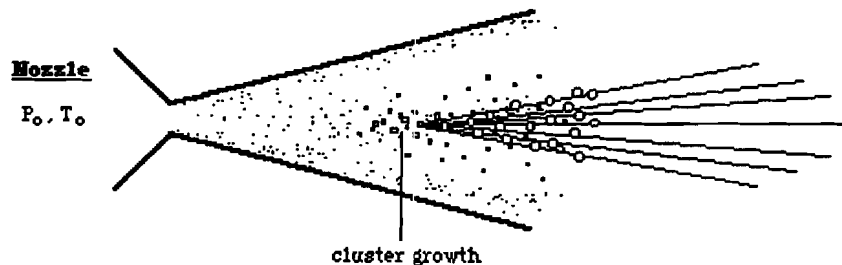


Figure 2.4: Cluster Formation from the Gas Jet Nozzle

The target for the \bar{p} beam was a hydrogen gas jet flowing perpendicular to the beam line [35]. The jet of hydrogen gas adiabatically expanded from an approximately $37\ \mu\text{m}$ flared nozzle at temperatures from 21 K to 80 K and pressures up to 100 psi, thus creating condensed hydrogen molecular clusters (see figure 2.4). The clusters traveled from the nozzle through several chambers of vacuum pumps separated by skimmers to keep the jet narrow. The diameter of the gas jet was

6.3 mm for 95% containment. After crossing the interaction region, the hydrogen was pumped out so as not to contaminate the vacuum in the beam pipe.

The design of the gas jet allowed the experiment to adjust the nozzle temperature and pressure, and thus the density, of the hydrogen molecular clusters. Figure 2.5 shows the relation between temperature, pressure, and density.

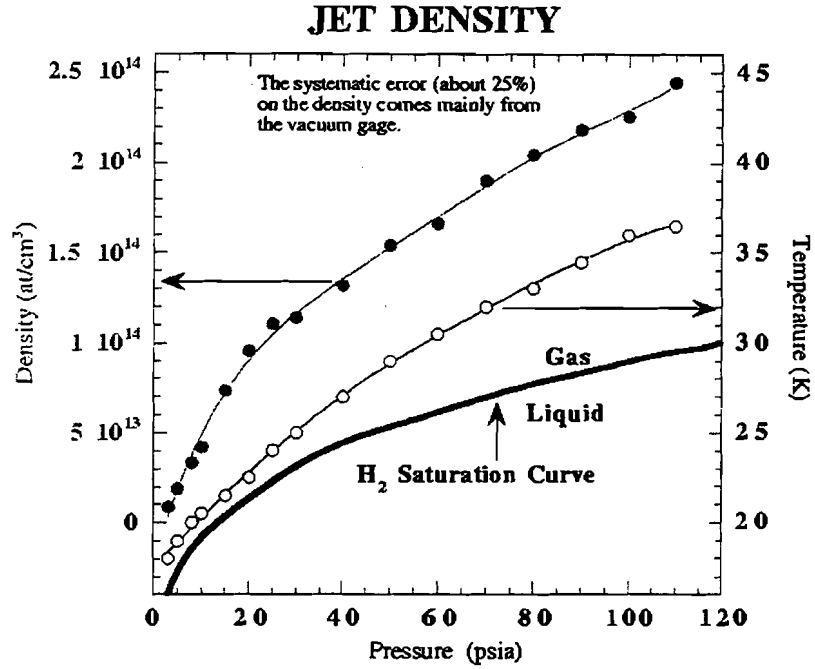


Figure 2.5: Gas Jet Density as Function of Temperature and Pressure

As the beam circulated and repeatedly interacted with the jet protons, the beam current, I_{beam} , would decrease. However, since the luminosity, \mathcal{L} , is given by

$$\mathcal{L} \propto d \times I_{beam} \quad (2.7)$$

where d is the density of the hydrogen gas, the luminosity could be kept constant

by increasing the density. The density could be adjusted, while taking data, up to about 3.2×10^{14} at/cm³ which allowed us to maintain a luminosity on the order of 2.0×10^{31} cm⁻² sec⁻¹ (near the maximum rate the data acquisition system could handle). This not only allowed E835 to maximize the number of interactions for a given amount of beam, but also helped to reduced rate dependent systematics in the analyses. Figure 2.6 shows how luminosity was kept constant even as beam current decreased.

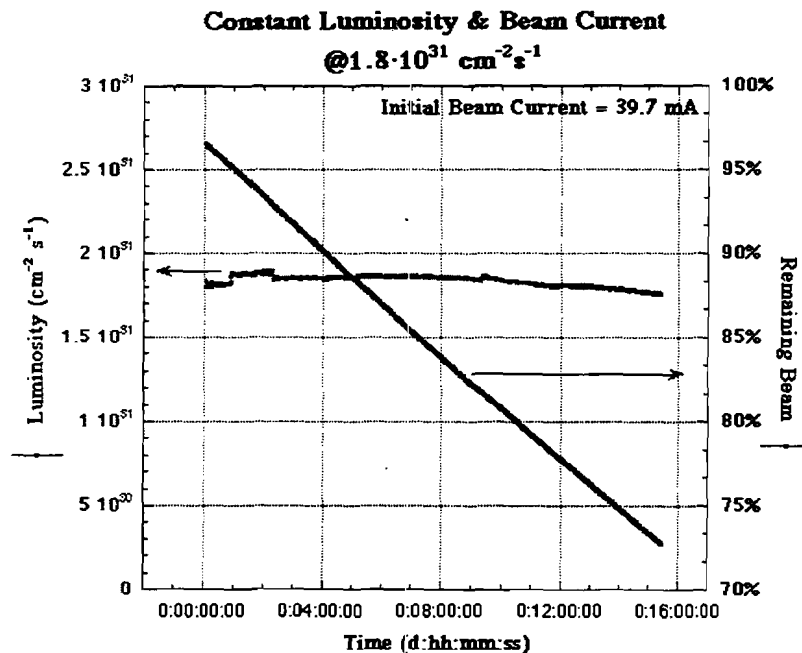


Figure 2.6: As the beam current falls, the gas density (not shown on plot) is raised enough to keep luminosity constant.

2.3 E835 Detector

The E835 detector consisted of a luminosity monitor, an inner charged tracking system, a threshold Čerenkov detector, and two Pb glass calorimeters covering different polar angle regions. The detector schematic is figure 2.7.

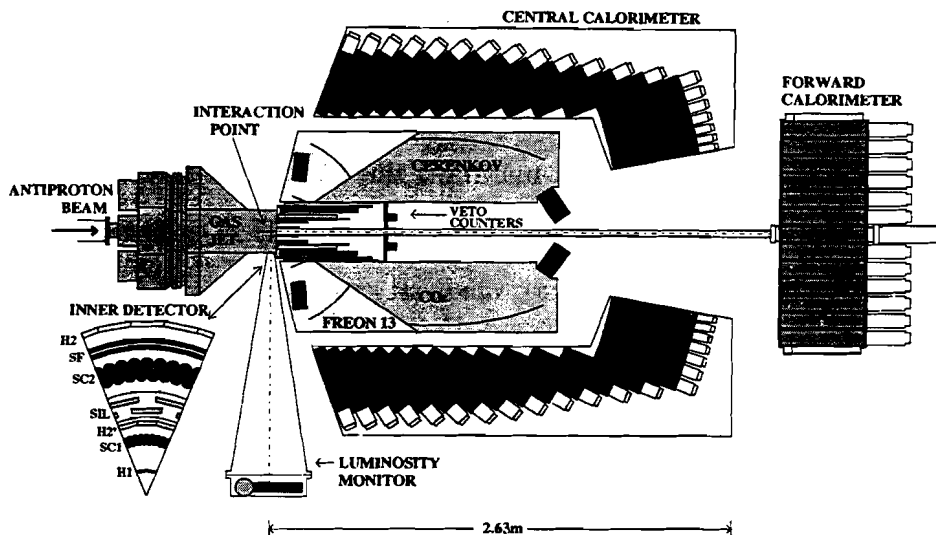


Figure 2.7: The E835 Detector

2.3.1 Luminosity Monitor

The integrated luminosity, necessary to determine cross sections and decay rates, is (rewriting equation 2.7)

$$\mathcal{L} = N_{\bar{p}} f \rho \quad (2.8)$$

where $N_{\bar{p}}$ is the number of circulating antiprotons, f is the \bar{p} revolution frequency, and ρ is the area density of the target. Since the thickness of the gas jet target cannot be measured well enough to give an error on \mathcal{L} of only a few percent, the luminosity monitor was necessary.

The luminosity monitor was composed of three 500 μm thick solid state detectors (thick enough to stop 8 GeV protons) located 147 cm below the interaction region at a polar angle (with respect to the beam direction) of 86.435° [36]. One detector was

mounted on a movable tray located directly beneath the beam axis. The other two were fixed detectors located symmetrically on either side of the movable detector. The active surface area of each detector was about $1 \text{ cm} \times 5 \text{ cm}$.

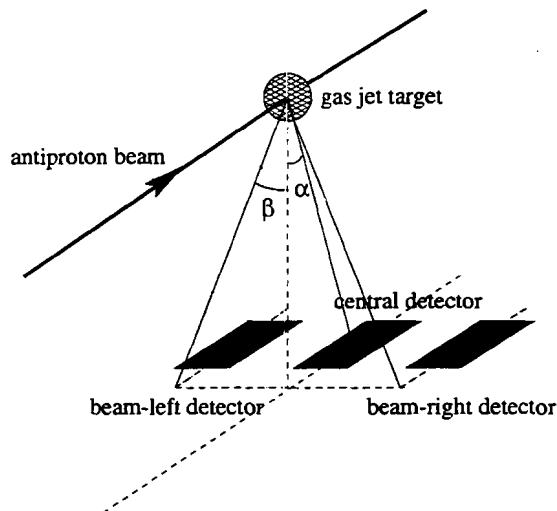


Figure 2.8: Representation of the E835 Luminosity Monitor

Having three detectors enabled a more accurate \mathcal{L} calculation and allowed E835 to detect horizontal displacement of the beam³. A representation of the E835 luminosity monitor is shown in figure 2.8.

The luminosity can be found to within a few percent by counting the numbers of recoil protons from low momentum transfer ($t < 0.05(\text{GeV}/c^2)^2$) elastic scattering $\bar{p}p$ interactions since,

$$N = \mathcal{L} \frac{d\sigma_{el}}{dt} \frac{dt}{d\Omega} d\Omega \quad (2.9)$$

where N is the number of the recoil protons, σ_{el} is the elastic scattering cross section, and $d\Omega$ is the solid angle subtended by the detector [37]. The $\bar{p}p$ differential elastic

³Vertical beam offset would, of course, be apparent from the large luminosity drop as the beam partially or fully missed the jet.

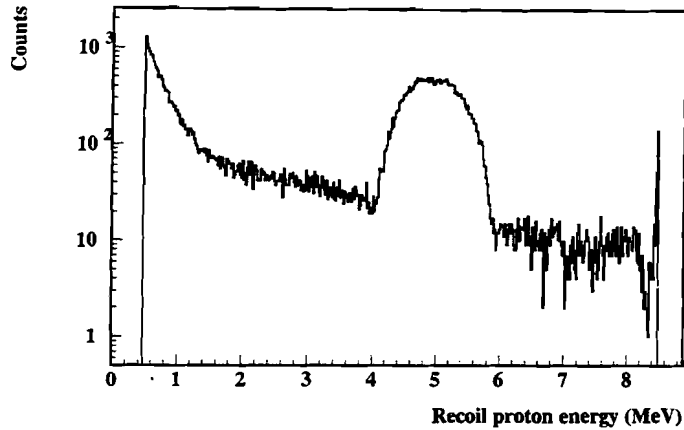


Figure 2.9: Typical Luminosity Spectrum

cross section is well measured at low momentum transfer. A typical luminosity spectrum is shown as figure 2.9. The signal sits on top of an exponential background.

The error on the luminosity measurement was less than 4% of which most was systematic error; in particular 2.5% was due to the error on the differential cross section [38].

2.3.2 Inner Detectors

The purpose of the E835 inner detectors was to detect charged particle tracks. It consisted of three scintillating hodoscopes ($H1$, $H2$, and $H2'$), two double layered straw tube drift chambers ($SC1$ and $SC2$), a silicon pad detector (SI), a double layered scintillating fiber tracker (SF), and a forward hodoscope (FCH). The first seven detectors are arranged symmetrically around the beam axis. The forward hodoscope is perpendicular to the beam axis at the backend of the other inner detectors. A schematic of the inner detectors is shown as figure 2.10.

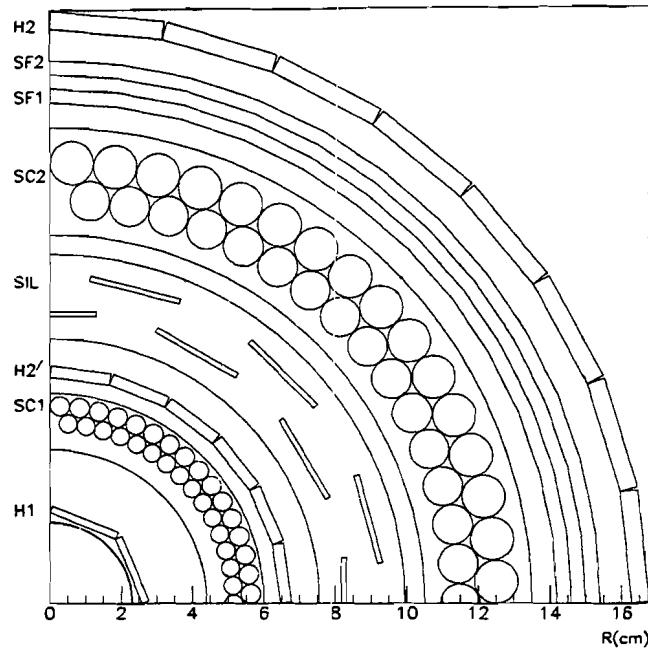


Figure 2.10: Beam's View of the Inner Detectors. Only one quarter is shown.

Scintillating Hodoscopes

The three scintillating hodoscopes were composed of rectangular Bicron 408 scintillators arranged to be azimuthally symmetric about the beam axis. Their primary function was to detect charged particles and produce fast trigger signals. Thus they could also be used to reject events with unwanted charged tracks.

H1 consisted of eight 1 mm thick scintillating paddles with the center of each paddle 5 cm from the center of the beam pipe. It covered polar angles 9° to 65° . *H2'* consisted of 24 2 mm thick scintillating paddles with the center of each paddle 7 cm from the center of the beam pipe. It also covered polar angles 9° to 65° . *H2* consisted of 32 2 mm thick scintillating paddles with the center of each paddle

15.8 cm from the center of the beam pipe. It covered polar angles 15° to 65° .

$H1$ and $H2$ were aligned such that the cracks would coincide for each $H1$ paddle (each $H1$ paddle covers four $H2$ paddles). $H2'$ was aligned in such a way that the center of $H2'$'s paddles were lined up with the cracks of the other hodoscopes, thus reducing the crack inefficiency.

Each of the scintillator paddles was light tight and coupled to their own light guides and photomultiplier tubes. $H1$ and $H2$ used Phillips XP2982 PMTs, while $H2'$ used Hamamatsu R1398 PMTs.

The Forward Charged Hodoscope was a set of eight flat scintillating paddles placed perpendicular to the beam pipe. Each paddle covered about 50° in azimuthal angle so there was about 2.5° of overlap between adjacent paddles. The polar angle coverage of FCH was 2° to 10° . The purpose of FCH was to veto events with charged tracks in the forward direction and to determine whether energy deposited in the forward calorimeter was from charged particles or photons.

Silicon Pads

The 4608 silicon pads [39] were cylindrically symmetric and arranged on 24 printed boards about 9 cm from the center of the beam pipe. Due to excessive electronic noise, this detector could not be used for E835 analyses.

Straw Tubes

Two cylindrical straw tube chambers [40], at radii of 5.4 cm and 12.0 cm, were used to provide a measurement of the azimuthal coordinate (ϕ) for the charged tracks. Each chamber consisted of two staggered layers of 64 drift tubes oriented parallel to the beam pipe. The tubes contained a mixture of Ar , C_4H_{10} and $(OCH_3)_2CH_2$ in

the proportions of 82:15:3 with a drift velocity of about $40 \mu\text{m}/\text{ns}$. Each of the 128 channels was read out by an amplifier-shaper-discriminator directly mounted to the downstream end of the detector. The output signals were then sent to TDCs.

The detection efficiency per layer ranges from 80%, near the wall of the tubes, to 100% near the anode wire. The angular resolution per track, measured with a clean sample of $\bar{p}p \rightarrow J/\psi \rightarrow e^+e^-$ events, was about 9 mrad per track.

Scintillating Fiber Tracker

The scintillating fiber tracker's primary use was to measure the polar angle, θ , of charged tracks with high precision [41]. The signal was also used in the first level trigger to select hadronic channels based upon their kinematics. The 860 channel tracker had two layers, 430 channels each, of scintillating fibers which were wrapped around a support cylinder with average radii 14.4 cm and 15.06 cm. The 95 cm Kuraray SCSF-3HF-1500 multiclad fibers had an outer diameter of 0.835 mm and a core diameter of 0.74 mm. The tracker covered 15° to 65° in θ . The fibers were aluminized at one end to increase the light yield and improve homogeneity. The other ends were thermally spliced to 4 m clear fibers which carried the light to the surface of the Visible Light Photon Counters (VLPCs).

The VLPCs are solid state photo detectors with high quantum efficiency (70% at 550 nm). They were housed in a cryostat and operated at a temperature of 6.5 K. The signals from VLPCs were amplified and sent to ADCs, TDCs, and the first level trigger logic. The intrinsic resolution was about (0.7 ± 0.1) mrad.

2.3.3 Threshold Čerenkov Counter

The threshold Čerenkov counter was used in the charged particle trigger and the offline to select electrons and positrons out of the large hadronic background [42]. The Čerenkov detector was a cylindrical shell around the beam pipe with an inner radius of 17 cm and an outer radius of 59 cm. It was divided into two cells. The downstream cell covered 15° to 38° in θ and the upstream cell covered 34° to 65° . The cells were equally segmented into 8 mirrored sections, each covering 45° in ϕ and aligned with one of the eight H1 counters.

The two segments of the Čerenkov were used to house different gases, both at room temperature and one atmosphere of pressure. Two gases were needed to allow optimization of electron detection and pion identification for good e/π separation, the characteristics of which are determined by kinematics – in particular θ .

The downstream cell was filled with CO_2 (the index of refraction, n , is 1.00041). The upstream cell was filled with Freon-13 (CF_3Cl)⁴ with $n=1.00072$. The Čerenkov angle θ_c , defined by the equation $\cos \theta_c = 1/\beta n$, is (note $\beta \approx 1$) 1.64° for CO_2 , 2.17° for Freon-13, and 2.66° for Freon-12. The pion energy threshold, $E_{threshold}$, from the equation

$$E_{threshold} = \frac{m_\pi}{\sqrt{1 - \frac{1}{n^2}}} \quad (2.10)$$

where m_π is the pion mass is, for CO_2 , Freon-13, and Freon-12 respectively, 4.875 GeV, 3.680 GeV, and 3.005 GeV. Note that because of their low mass electrons/positrons are nearly always over threshold. Pions from the reaction $\bar{p}p \rightarrow \pi^+\pi^-$ at 15° in θ (the maximum energy a pion will have in the downstream cell), cross the threshold energy in CO_2 when the center of mass energy is 3.423 GeV. Similarly, pions created

⁴During the last month of running it was filled with Freon-12 (CF_2Cl_2) with $n=1.00108$.

from the same reaction but emitted at 34° (maximum energy in the upstream cell) cross the threshold energy when $E_{cm} = 3.368$ GeV for Freon-12 and when $E_{cm} = 4.293$ GeV for Freon-13. This dependence of energy threshold on emitted pion angle is shown as figure 2.11. Note that the energy threshold increases rapidly with θ , so for most angles and E835 energies, pions can be separated from the electrons quite effectively.

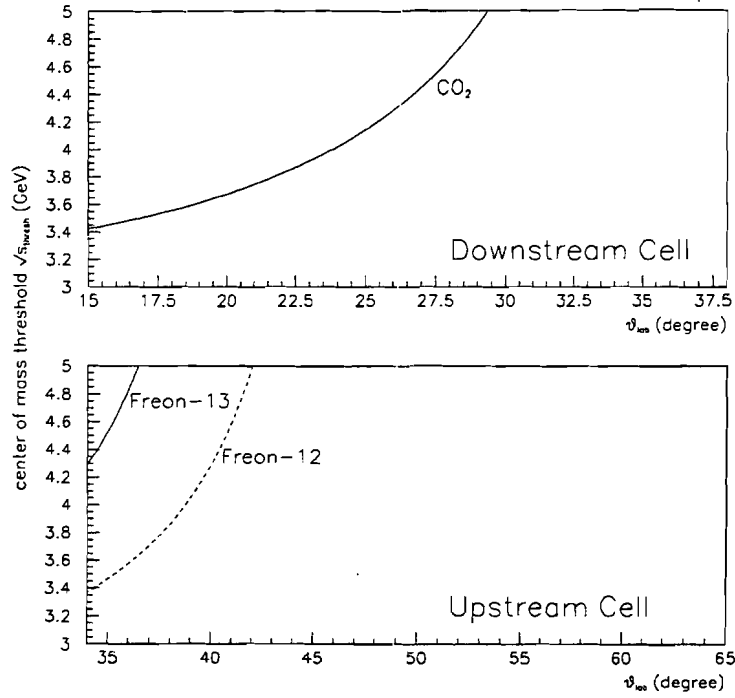


Figure 2.11: Threshold Curves for Čerenkov Cells

The eight ellipsoidal mirrors were built using carbon fiber epoxy composites. In the downstream cell, the first focus is at the center of the interaction region and the second focus is at the vertex of the regular octagon where the PMT windows were

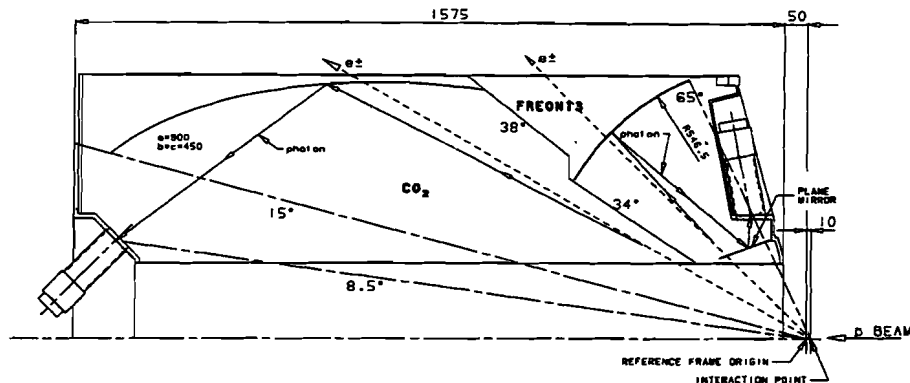


Figure 2.12: Cross Section Schematic of the Čerenkov Counter

In the upstream cell each of the eight sectors is equipped with a focusing spherical mirror and a plane mirror to reflect the light onto a PMT placed on the counter's back wall. All PMTs are 2" diameter Hamamatsu R1332Qs. A transverse view of the counter is shown in figure 2.12. The photoelectron yield was 14 to 16 (8 to 9) per incident electron for the downstream (upstream) cell. The signals from the PMTs were amplified, split, and sent to the charged trigger, ADCs, and TDCs.

The efficiency of the Čerenkov counter was found using clean samples of $J/\psi \rightarrow e^+e^-$ and $\chi_2 \rightarrow \gamma J/\psi \rightarrow \gamma e^+e^-$. Events were accepted if they satisfied a kinematical fit with a probability greater than 1%. The single electron detection efficiency was calculated to be $(98.1 \pm 0.5)\%$.

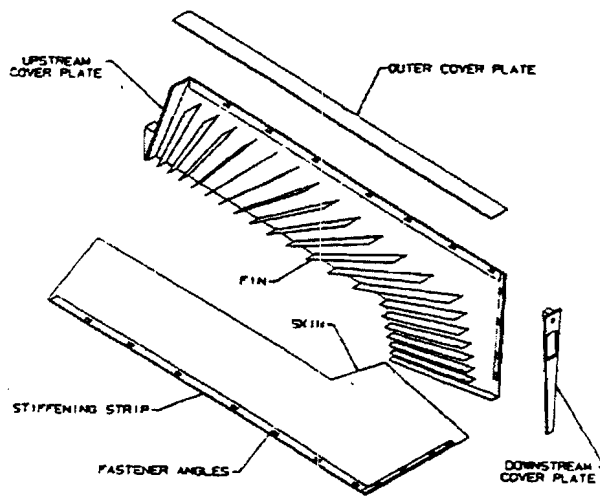


Figure 2.13: Schematic of a CCAL Wedge

2.3.4 Central Calorimeter

Around the Čerenkov counter was the central calorimeter (CCAL). The CCAL, which was used to measure the energies and positions of photons and electrons (and positrons), was the heart of the E835 detector. It was built with 1280 Schott F2 type Pb glass blocks, which were arranged with a pointing geometry to the interaction region. The blocks were arranged such that there were 20 blocks in a wedge (common ϕ and covering 10.6° to 70° in θ) and 64 blocks in a ring (common θ with full azimuthal symmetry). The design for one wedge is shown in figure 2.13.

The wedge housing for the blocks was made from stainless steel with a separation between blocks in a common wedge, the fins, of 0.254 mm, and a separation between blocks in adjacent wedges, the skins, of $0.735 \text{ mm} \times 2 = 1.47 \text{ mm}$. Having material between the blocks was undesirable from an energy reconstruction point of view, but it was deemed at the time the best way to physically construct the calorimeter.

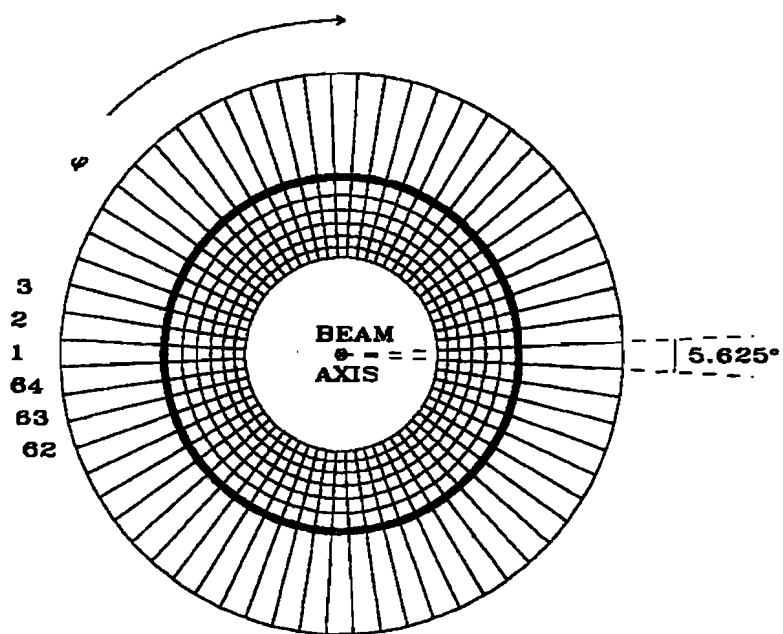


Figure 2.14: Beam's View of the Central Calorimeter

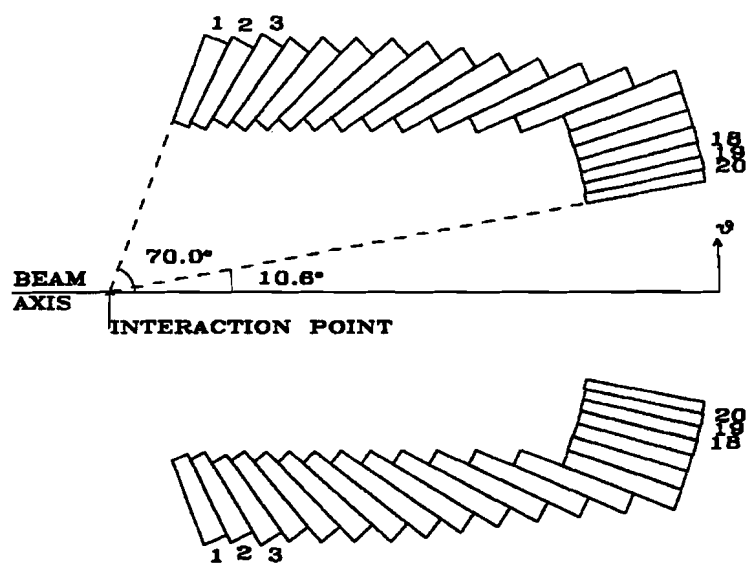


Figure 2.15: Side View of the Central Calorimeter

64 wedges were stacked in the cylindrical construct which sat atop rollers to allow rotation of the entire CCAL in the event maintenance on a bottom wedge was required. Figures 2.14 and 2.15 show cross sectional views in ϕ and θ respectively. The CCAL granularity was decided as a compromise between the necessity of resolving photons from symmetric π^0 decays at high energies and not wanting too much inert material between blocks.

Each wedge was equal in ϕ thus making them 5.625° each. The blocks ranged from about 38 cm long at the largest θ (ring 1) to about 50 cm at the smallest θ (ring 20). These lengths correspond to radiation lengths of approximately 12 to 16. The electromagnetic shower of Čerenkov radiation emitted as the glass was struck by photons, electrons, or positrons had a Moliere radius such that the energy was about 95% contained in the block. The length, angular position in θ , and distance to the nominal interaction point of the blocks in each CCAL ring are described in table 2.2.

The light was collected by Hamamatsu photomultiplier tubes (PMTs) glued to the back of each block. Because the size of the blocks vary for different rings, four sizes of PMTs were used (to best match the back surface of the block). The three types of PMTs used were 3" R3036-02 for rings 1 to 14, 2.5" R3345-02 for rings 15 to 16, 2" R2154-04 for rings 17 to 18, and 1.5" R580-13 for rings 19 to 20. The PMTs were connected to RG-174 cable which connects to the back of the wedge housing and couples to another RG-174 cable residing external to the wedge housing. A fiber optic cable was also connected to each block and then to a laser system to allow monitoring of the CCAL blocks by pulsing light into them and observing the output.

Ring	Length (cm)	Central θ (degree)	$\Delta\theta$ (degree)	Front face from target (cm)	PMT size (in.)	Fractional PMT coverage
1	37.80	67.387	5.226	72.44	3.0	0.473
2	38.65	62.259	5.031	75.87	3.0	0.475
3	39.88	57.342	4.803	80.07	3.0	0.476
4	41.50	52.664	4.552	85.08	3.0	0.478
5	43.54	48.246	4.284	90.96	3.0	0.479
6	46.03	44.101	4.007	97.79	3.0	0.481
7	48.98	40.234	3.728	105.62	3.0	0.482
8	50.00	36.644	3.451	114.54	3.0	0.497
9	50.00	33.327	3.183	124.66	3.0	0.520
10	50.00	30.273	2.925	136.07	3.0	0.544
11	50.00	27.472	2.679	148.89	3.0	0.568
12	50.00	24.908	2.449	163.26	3.0	0.593
13	50.00	22.567	2.233	179.34	3.0	0.617
14	50.00	20.434	2.033	197.28	3.0	0.641
15	50.00	18.493	1.848	197.29	2.5	0.546
16	50.00	16.730	1.678	197.29	2.5	0.664
17	50.00	15.130	1.522	197.30	2.0	0.527
18	50.00	13.679	1.380	197.30	2.0	0.644
19	50.00	12.364	1.250	197.30	1.5	0.443
20	50.00	11.174	1.131	197.30	1.5	0.543

Table 2.2: Lengths, Angular Position in θ , and Distance to Interaction Point for Blocks in Each CCAL Ring

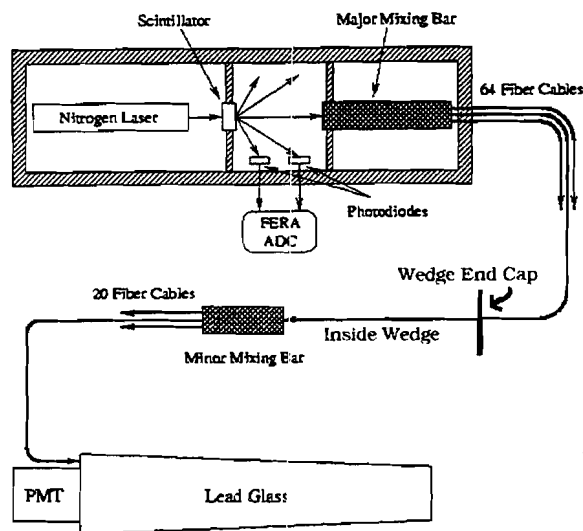


Figure 2.16: The Laser Monitor System

Laser Monitor System

Because Pb glass is vulnerable to radiation damage, the gains of the CCAL channels needed to be calibrated and monitored constantly. The monitor system also provided a check preventing E835 from running with the high voltages set incorrectly. A schematic of the laser monitor is shown as figure 2.16.

A Laser Science, Inc. model VSL-337ND nitrogen laser was chosen as the light source due to its narrow pulse width of about 3 ns with a 1 ns rise time and pulse consistency on the order of 4%. The narrow pulse width enabled the DAQ to collect laser data events using the normal gate. The UV light from the laser was incident upon a scintillator which produced visible blue light. After entering a leucite mixing bar the light evenly entered 64 fiber optic cables each of which entered one of the wedge housings. Another mixing bar in the wedge housing distributed the light to the individual blocks via the fiber optics (attached to the backs of the blocks)

mentioned previously. Two photodiodes placed before the first mixing bar were used to monitor the laser light. The laser was pulsed every ten seconds during data taking and the events were written to tape on a special trigger. See reference [43, Appendix B] for details on the laser monitor and CCAL calibration.

CCAL Signal Shaping

Because of the large increase in instantaneous luminosity going from E760 to E835, the CCAL readout had to be modified to minimize multiple pulses in a single FERA gate. The solution was to use a Splitter-Shaper-Discriminator Circuit to reshape the signal thus allowing it to fit in as narrow a FERA gate as possible. It was determined that 100 ns was the smallest gate that could reasonably be used. Shaping the signal also had the benefit of minimizing the tail of the signal which was quite large in E760. After being shaped, a small part of each of the 1280 CCAL signals was sent to a discriminator set at 6 mV (about 12 MeV) and then continued to a TDC. The remaining signal from the shaper went directly to the FERA. See reference [43, Appendix A] for details on shaping the CCAL signals.

CCAL Clusterizer

The goal of the CCAL clusterizer was to accurately determine the energies and positions of hits in the central calorimeter. The clusterization routines started by searching for block energies in the CCAL beginning with the block at wedge one ring one and continuing to ring 20, then switching to the next higher wedge at ring one etc. The clusterizer looked for local maxima, defined as the block with the largest energy deposit among its eight neighbors. This was denoted the seed block.

The seed block and the 3×3 block cluster centered on the seed block had to be

above a particular energy threshold. For analyses sensitive to low energy photons, such as $\gamma\gamma$, the seed/cluster thresholds were 5/20 MeV and for the other analyses, including this one, the thresholds were 25/50 MeV. The clusters, defined as these 3×3 grids about a seed were classified into three types: isolated, shared, or split.

A cluster is isolated when its 3×3 grid does not overlap another cluster's grid. The entry position of the incident particle was found using the energy weighted sum of the grid blocks, thus allowing position resolution to better than one block width. The i^{th} block in the grid had an energy deposit E_i and a distance, in block units, of x_i along the θ_{lab} direction and y_i along the ϕ_{lab} direction with respect to the seed block, i.e. $x_i, y_i \in \{-1, 0, 1\}$. The entry position could then be expressed as

$$x = \frac{\sum_{i=1}^9 E_i x_i}{\sum_{i=1}^9 E_i} \quad (2.11)$$

$$y = \frac{\sum_{i=1}^9 E_i y_i}{\sum_{i=1}^9 E_i} \quad (2.12)$$

Note, however, that this does not take into account the fact that blocks were not square and that the energy lost in the inactive material between blocks was different in the x and y directions due to the different thickness of the skins and fins. To correct for these a parameterization of the shower profile was used.

The shower profile could be parameterized by two exponential functions where one described the shower core and the other described the shower tail [44]. The corrected positions, X and Y , were then calculated using the initial positions x and y from equations 2.11 and 2.12 as

$$|X| = A_x(1 - e^{-\frac{|x|}{x_A}}) + B_x(1 - e^{-\frac{|x|}{x_B}}) \quad (2.13)$$

$$|Y| = A_y(1 - e^{-\frac{|y|}{y_A}}) + B_y(1 - e^{-\frac{|y|}{y_B}}) \quad (2.14)$$

where $A_{x,y}$, $B_{x,y}$, $x_{A,B}$, $y_{A,B}$ were determined empirically from test beam data taken at Brookhaven National Laboratory. Their values are given in table 2.3. The sign of X and Y was the same as the sign of x and y respectively.

A_y	724.4	y_A	0.03208
A_x	706.5	x_A	0.03969
B_y	123.6	y_B	0.1860
B_x	102.6	x_B	0.1715
C_{low}	0.0614	$x_{C,low}$	7.367
C_{high}	0.0857	$x_{C,high}$	19.690
C_y	0.14736	y_C	48.908
D_y	0.15935	y_D	12.761

Table 2.3: Shower Profile Constants

The energy was similarly corrected using the equation

$$E_{corrected} = \frac{E_{measured}}{(1 - C_x e^{-\frac{|X'|}{x_C}})(1 - C_y e^{-\frac{|Y'|}{y_C}} - D_y e^{-\frac{|Y'|}{y_D}})} \quad (2.15)$$

where $E_{measured}$ was the measured energy of the cluster and (X', Y') was the entry position corrected but measured from the block edge instead of the center. Also, it had to be taken into account that the staggering of the blocks meant the corrections would be different depending on whether the incident particle hit the upper half of the block (then $C_x = C_{high}$) or the lower half (then $C_x = C_{low}$). These values were also determined from the test beam at BNL and are shown in table 2.3. Figure 2.17 shows the ratio of the corrected and uncorrected energies to the predicted energy for the decay $J/\psi \rightarrow e^+e^-$ as a function of the distance from the crack.

Shared clusters occurred when two clusters' 3×3 grids share non-seed blocks. The energy must then be split between them. Initially, the corrected energy and

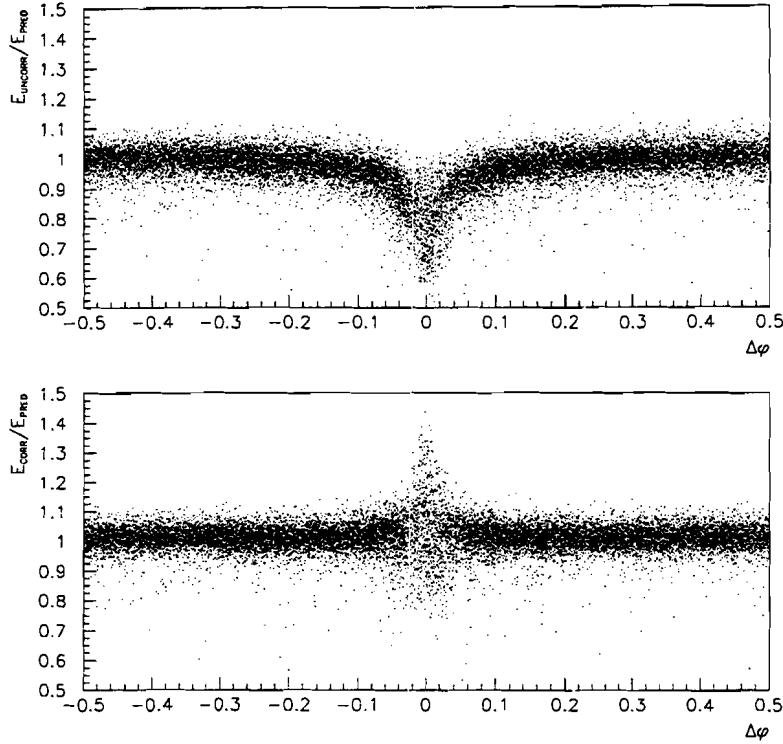


Figure 2.17: Ratio of Corrected (bottom) and Uncorrected (top) Energies to the Predicted Energy from $J/\psi \rightarrow e^+e^-$ as a Function of Distance from the Crack

position of each cluster was calculated as if the other cluster did not exist. Thus, energy in the overlapping blocks was double counted. Assuming that the cluster energy drops off exponentially from the center of the cluster, the fraction of the energy, $f_{i,n}$, in a shared block, i , coming from cluster n is given by

$$f_{i,n} = \frac{E_n e^{-\frac{(|x_{i,n}|+|y_{i,n}|)}{0.17}}}{E_1 e^{-\frac{(|x_{i,1}|+|y_{i,1}|)}{0.17}} + E_2 e^{-\frac{(|x_{i,2}|+|y_{i,2}|)}{0.17}}} \quad (2.16)$$

where E_m and $(x_{i,m}, y_{i,m})$ are the energy and position (from the middle of block i) of cluster m . The constant 0.17 was determined empirically with $J/\psi \rightarrow e^+e^-$ data. Then, the new cluster energy can be expressed as

$$E'_n = \sum_{i=1}^9 f_{i,n} E_i \quad (2.17)$$

where $n=1,2$ for the two shared clusters. The new positions could be found from a variation of equations 2.11 and 2.12:

$$x'_n = \frac{\sum_{i=1}^9 f_{i,n} E_n x_i}{\sum_{i=1}^9 f_{i,n} E_i} \quad (2.18)$$

$$y'_n = \frac{\sum_{i=1}^9 f_{i,n} E_n y_i}{\sum_{i=1}^9 f_{i,n} E_i} \quad (2.19)$$

An iterative procedure was then used where the new positions and energies were used as input to equation 2.16 and new energies and positions were found from equations 2.17, 2.18, and 2.19 etc. The iteration was complete when the θ and ϕ positions changed by less than 5 mrad and the energy changed by less than 30 MeV.

The final classification of cluster was the split cluster. A split cluster occurred when two clusters were so close together that a second local maximum was not discernible, such as in symmetric π^0 decays. For π^0 decays, at the largest E835 energies, the smallest opening angle between the final photons could be as small as 1.5 blocks. To identify these events the cluster mass, M_{cl} , was found for a 5×5 block grid about the local maximum for each isolated cluster as

$$M_{cl} = \sqrt{\left(\sum_i E_i\right)^2 - \left(\sum_i \vec{p}_i\right)^2} \quad (2.20)$$

where E_i was the energy in the i^{th} block of the grid and \vec{p}_i was defined as $E_i \hat{r}_i$ where \hat{r}_i was the unit vector from the interaction point to the i^{th} block. Figure 2.18 shows M_{cl} for e^+e^- from J/ψ decays and $\pi^0 \rightarrow \gamma\gamma$ decays from $\pi^0\pi^0$ data. The small peak is from isolated π^0 clusters and the large peak is from coalesced π^0 s. Clusters with M_{cl} above 100 MeV were split. Figure 2.19 shows the recovery of the asymmetric π^0 s obtained by splitting clusters.

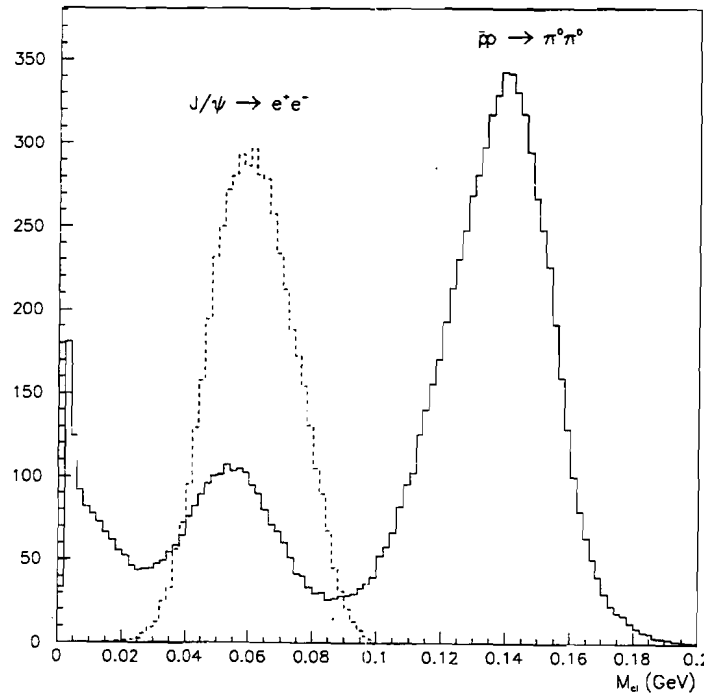


Figure 2.18: Cluster Mass Showing Electrons, Photons, and Pions

The procedure for splitting clusters was similar to the method for sharing clusters. In the split case, a second local maximum was chosen to be the block with the largest energy deposit on one of the four corners of the 3×3 grid centered at

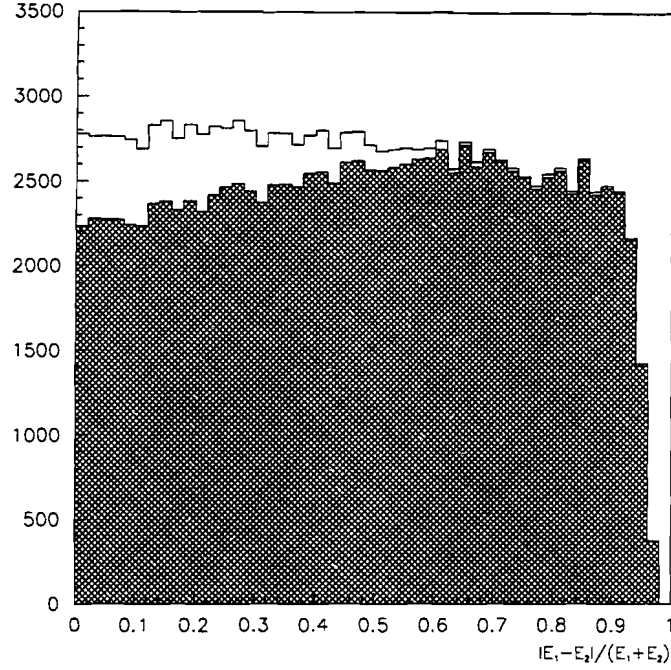


Figure 2.19: π^0 Asymmetry Plotted without Split Clusters (shaded) and Including Split Clusters (open)

the seed block. Since much information from the tail of that cluster was blocked by the large energy of the seed block, a 5×5 grid was chosen for the position and energy calculations (to get as much information on the shower as possible). It was also best to not include the seed block's energy for either cluster in the parameter determinations of the other cluster. With these exceptions, the procedure for energy and position determination mirrors that of the shared cluster. Note that by not including the seed block energies to find the other cluster parameters there will be an overestimation of the calculated π^0 invariant mass.

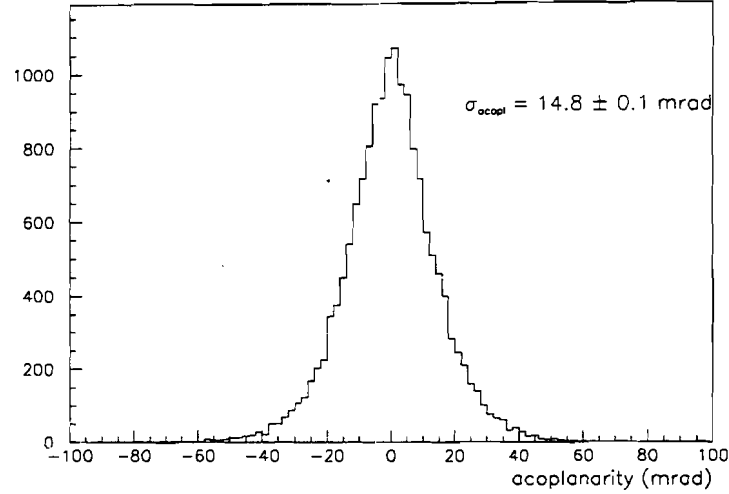


Figure 2.20: Deviation of ϕ from Two-Body Kinematics

CCAL Resolution

The CCAL resolution was calculated using the numerous and easy to identify $J/\psi \rightarrow e^+e^-$ decays. For e^+ and e^- azimuthal angles ϕ_{e^+} and ϕ_{e^-} respectively (and in fact for any two-body decay), the amount the event deviates from the expected two-body kinematics, $\Delta\phi$, is,

$$\Delta\phi \equiv \pi - |\phi_{e^+} - \phi_{e^-}| \quad (2.21)$$

The distribution of $\Delta\phi$ is shown as figure 2.20. The figure shows a $\sigma_{\Delta\phi}$ of about 15 mrad which through the equation $\sigma_{\Delta\phi} = \sqrt{2}\sigma_\phi$ leads to a ϕ resolution for the CCAL of 11 mrad.

Looking at the same two-body kinematics in the θ variable, where for example

$\theta_{e^+,meas}$ and $\theta_{e^+,theor}$ are the measured and theoretical values for the e^+ based on the location and energy of the e^- , the deviation of θ from real two-body kinematics, $\Delta\theta$ is,

$$\Delta\theta = \theta_{e^+,meas} - \theta_{e^+,theor} \quad (2.22)$$

The distribution of $\sigma_{\Delta\theta}$ is shown in figure 2.21 and through its dependence on the σ_θ reveals a CCAL resolution in θ of 6 mrad.

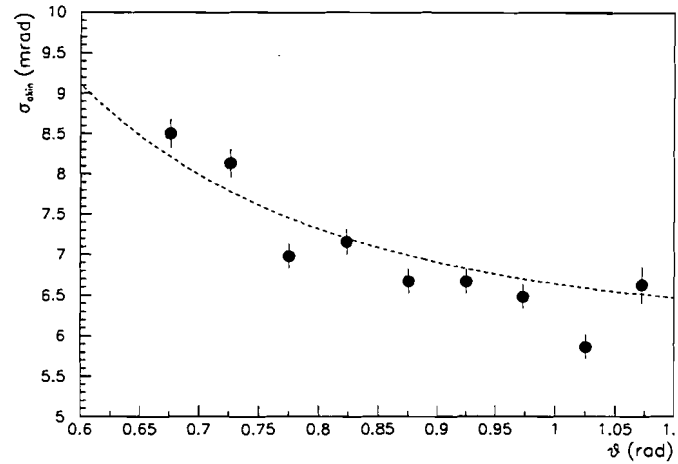


Figure 2.21: Deviation of θ from Two-Body Kinematics

The electron and positron energy is again predicted from two body kinematics using θ as measured by the CCAL. Figure 2.22 shows the quantity $(E_{meas} - E_{theor})/E_{meas}$. This shows consistency with the E760 calculation for the energy resolution [26] given by

$$\frac{\sigma_E}{E} = \frac{5.0\%}{\sqrt{E(GeV)}} + 1.4\% \quad (2.23)$$

and taking into account the cluster crack correction, where f is defined by $E_{corrected} =$

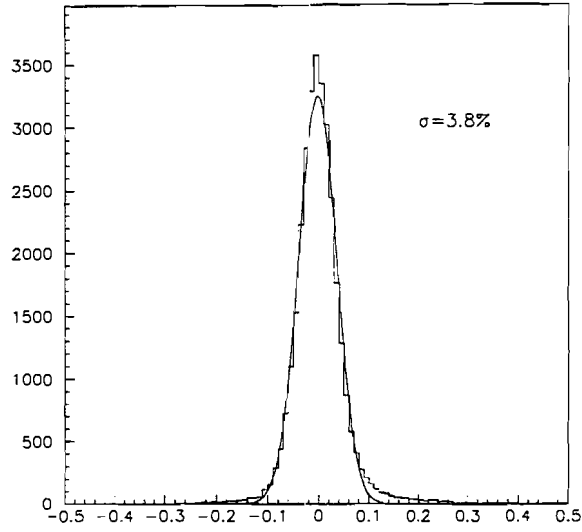


Figure 2.22: Deviation of Energy from Two-Body Kinematics

$f E_{measured}$, the energy error on a cluster was

$$\frac{\sigma_E}{E} = \frac{0.05}{\sqrt{E}} + 0.3(f - 1)E + 0.005 \quad (2.24)$$

See reference [45, Chapter 3] for more details on cluster parameter errors, CCAL resolutions and vertex determination from CCAL data.

Cluster Timing

Because of E835's large instantaneous luminosity and unavoidable noise or extraneous reactions with particles hitting the CCAL, signals not associated with the event under examination could cause contamination by sharing the same CCAL FERA gate with the desired event. For example, the tail end of a large signal from a pre-

vious event could enter the same FERA gate, over threshold, and be recorded as a signal. The CCAL was thus instrumented with TDCs to separate “intime” clusters, or those associated with the desired event, from the other clusters.

The time of a cluster was determined by the time of the largest energy block in a cluster (which should almost always arrive at the TDC first since it should have the steepest trailing edge signal upon entering the discriminator). The times recorded by the TDC were corrected for slewing to attempt to remove the effects of pulse height on time. If a cluster had no block with TDC information, as could happen when there were low energy clusters, the cluster time was labeled as “undetermined”. A cluster was labeled “intime” if the time was within ± 10 ns of the mean event time and “out of time” if there was a TDC but it was outside this window.

2.3.5 Forward Calorimeter

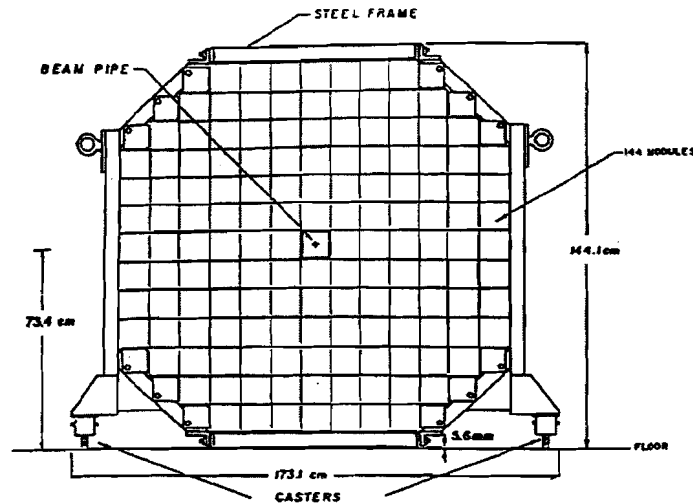


Figure 2.23: Forward Calorimeter I Schematic

During E835 running there were two different forward calorimeters, FCAL I and

FCAL II. Both covered 2° to 12° in θ . The first FCAL, used also in E760, was a set of 144 lead-scintillator sandwich counters [46]. Excessive radiation damage necessitated the creation of FCAL II. FCAL II was put in the detector in March 1997. It was built with 144 Pb glass blocks of three sizes. Schematics for FCAL I and FCAL II are shown in figures 2.23 and 2.24. The circle on the FCAL II plot shows where the central calorimeter shadows the FCAL II blocks. For E835 the FCAL was used primarily as a veto.

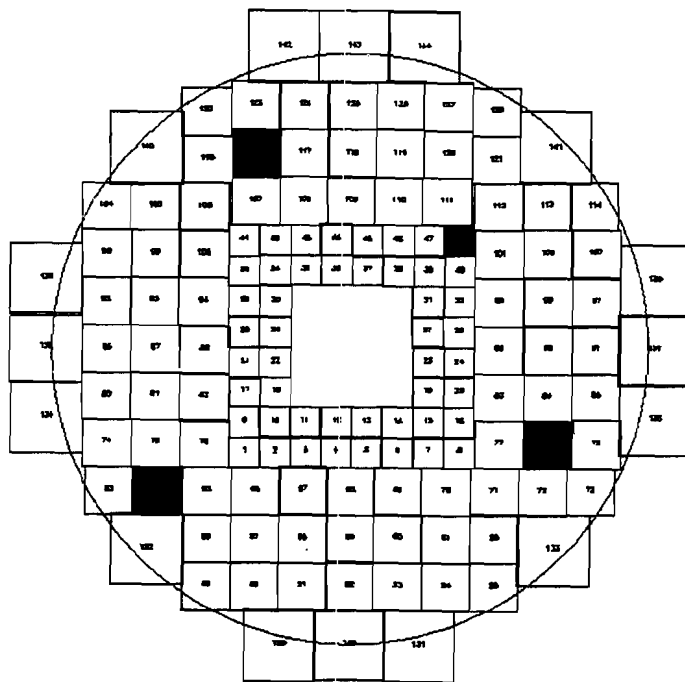


Figure 2.24: Forward Calorimeter II Schematic

Chapter 3

Data Acquisition

The E835 data acquisition system (DAQ) was built using DART (Data Acquisition for Real Time systems) [47] to process and record events. The DAQ system included methods for recording data from the various E835 detectors, a hardware trigger system designed to pick out potential events of interest, and a software trigger system for online analysis which allowed for the recording of data with specific physics interest by partial reconstruction and filtering of events.

Data from the luminosity monitor had its own DAQ [43, section 5.9] as did the data from parameters of the \bar{p} beam (called ACNET).

3.1 DAQ Hardware

The E835 Data Acquisition hardware is shown in figure 3.1. Data and logic signals from the individual detectors were read out by LeCroy 4300 and 4300b FERA ADCs and LeCroy 3377 TDCs situated in 19 CAMAC crates. The crates were addressed via two SCSI Jorway interfaces by an SGI Indigo computer used for run control

(fn835x). Most of the modules transferred data through their ECL ports to custom made Damn Yankee Controllers (DYCs). The modules used for triggering sent their logic signals via LeCroy CAMAC controllers and were used for triggering groups of ADCs and TDCs from the individual detector read-outs.

The DYCs stored data in their First-In First-Out (FIFO) buffers before sending them to two sets of two Access Dynamics DC2/DM115 modules. A DC2 module received data from a set of DYCs daisy chained via a DART cable. The DC2 then wrote the data to a Dual Port Memory (DPM) through the VSB backplane of a VME crate. The VME crate also contained a Motorola MMVME167 processor which used information from the triggering system and data from the DPMs to correctly construct the event information.

The Data Flow Manager (DFM), which ran on an SGI Challenge, distributed the events to its four 150 MHz CPUs for quick online analysis. The events were filtered and passed to disk and/or one or more of four tape drives depending on their identification by the trigger. All data was written to one of four streams, neutral, charged, $\phi\phi$, or calibration events, where each stream's data was put on an Exabyte 8500 8mm tape. Any events written to disk were subsets of what was on the tapes.

Another SGI Indigo (fn835z) was used for monitoring the detector and event displays.

3.2 E835 Trigger

E835 classified events into three major categories: charged triggers (whose final states included electrons and positrons), neutral triggers (events consisting of all photons in the final states), and a class of triggers (named the $\phi\phi$ triggers) designed

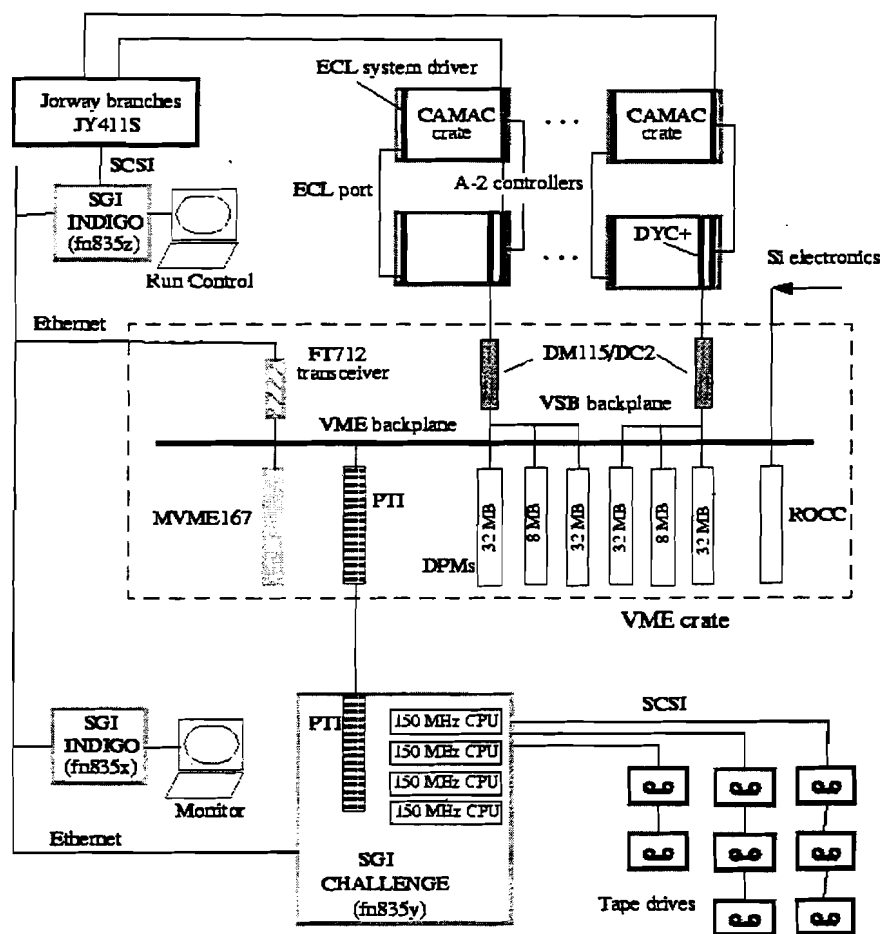


Figure 3.1: The E835 DAQ System

to tag specific final state charged hadron events such as $\bar{p}p$ and $2K^+2K^-$. This last class of triggers [48] is not used in this analysis and so will not be discussed in detail.

Each class of trigger was initiated by two levels of hardware trigger requirements followed by a software trigger which partially reconstructed events for final classification. The level one triggers were formed by one of three Memory Lookup Units (MLUs). Each MLU was a CAMAC module with 16 ECL inputs and eight NIM and 8 ECL output channels as well as a 16 channel buffered copy of the inputs. The three MLUs corresponding to the first level triggers were the charged MLU (CMLU), the neutral MLU (NMLU), and the $\phi\phi$ MLU (PMLU).

The second level of hardware triggering was formed when the outputs of the level one MLUs were used as input to a master MLU (MMLU). The MMLU checked the inputs against its lookup table to further classify the event. The data and the trigger information was then sent to the software trigger, called PRUDE (Program to Reject Unwanted Data Events), which ran on an SGI Challenge. PRUDE carried out a partial online event reconstruction to make the final trigger assignments so the data could be written to the proper stream. A diagram of the trigger system is shown as figure 3.2.

3.2.1 The Charged Trigger

The purpose of the charged trigger was to identify electron and charged hadron tracks in order to provide level one triggers for the events containing such candidate particles. For the charged trigger, the signals from the hodoscopes ($H1$, $H2$, $H2'$, and FCH), Čerenkov, and the forward calorimeter (see chapter 2) were discriminated to form fourteen input signals to the CMLU. The inputs and outputs of the CMLU are shown in table 3.1 and are explained below.

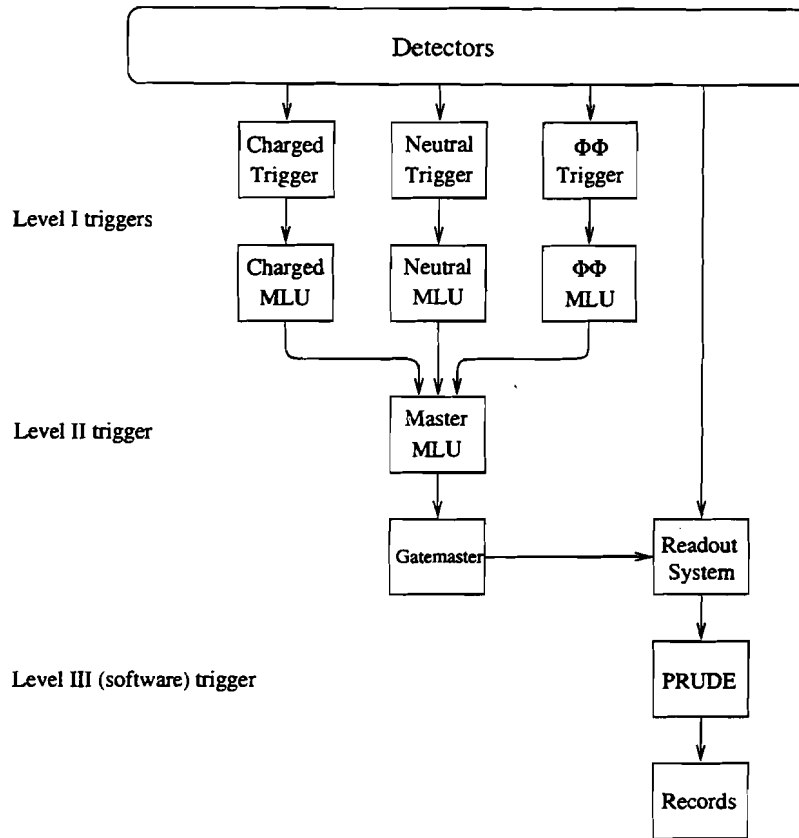


Figure 3.2: E835 Trigger System

The input signals of the CMLU were:

1. 1e (one electron): the AND of a hadron track (see input 3) and the OR of the two corresponding Čerenkov counters (upstream and downstream).
2. 2e: two electron tracks (i.e. 2 "1e"s – item 1 in this list).
3. 1h (one hadron): the AND between an $H1$ element and the OR of the six corresponding $H2$ elements.
4. 2h: two hadron tracks.

5. $H2 = 2$: exactly two $H2$ elements hit.
6. $H2 > 2$: more than two $H2$ elements hit.
7. $H2 > 4$: more four $H2$ elements hit.
8. $H1 > 2$: more than two $H1$ elements hit.
9. $H1 > 4$: more than four $H1$ elements hit.
10. COPL (coplanarity): the AND between an $H2$ element and the the OR of the three opposite $H2$ elements.
11. FCH_OR: the OR of all FCH elements.
12. FCAL_OR: the OR of all FCAL blocks.
13. $H1_OR$: the OR of all $H1$ elements.
14. $H2_OR$: the OR of all $H2$ elements.
15. Not Used.
16. Not Used.

The output signals of CMLU are:

1. $e^+e^-(1) = 2e \times \overline{H2 > 4} + 1e \times 2h \times (H2 = 2) \times COPL$
2. $e^+e^-(2) = 2e \times (H2 = 2) \times COPL \times \overline{FCH}$
3. $\Phi\Phi = 2h \times COPL \times \overline{FCH} \times \overline{FCAL}$
4. $p\bar{p} = 2h \times (H2 = 2) \times COPL \times \overline{FCH} \times \overline{FCAL}$

input channel	Description	output channel	Description
1	1e	1	$e^+e^-(1)$
2	2e	2	$e^+e^-(2)$
3	1h	3	$\phi\phi$
4	2h	4	$\bar{p}p$
5	$H2 = 2$	5	not used
6	$H2 > 2$	6	empty
7	$H2 > 4$	7	empty
8	$H1 > 2$	8	empty
9	$H1 > 4$		
10	COPL		
11	FCH_OR		
12	FCAL_OR		
13	H1_OR		
14	H2_OR		
15	empty		
16	empty		

Table 3.1: The Inputs and Outputs of the CMLU

$$5. \text{ unnamed} = \bar{1}e \times 2h \times (H2 = 2) \times COPL$$

Outputs 1 and 2 were used in forming the e^+e^- trigger, output 3 was used in forming the $\phi\phi$ trigger, and output 4 was used in forming the $\bar{p}p$ trigger. Output 5 was not used.

3.2.2 Neutral Trigger

The signals from the central calorimeter's 1280 blocks were input to the neutral trigger [49, 50]. The neutral trigger is made up of two trigger types – two-body triggers and total energy triggers. PBG1 (the acronym PBG is from Pb Glass) and PBG3 were the two-body event triggers for back to back events (PBG1), such as $\gamma\gamma$, e^+e^- ,

and $\pi^0\pi^0$, and loose back-to-back events (PBG3), such as $\bar{p}p \rightarrow \gamma J/\psi \rightarrow \gamma e^+e^-$. The total energy triggers, ETOT-HIGH and ETOT-LOW, triggered on events with a large portion of the total available energy deposited in the CCAL (e.g. multi-photon final states). The neutral trigger also provided a minimum bias strobe which was used by all MLUs and the gatemaster to synchronize the triggering process. A schematic of the neutral trigger is shown as figure 3.3.

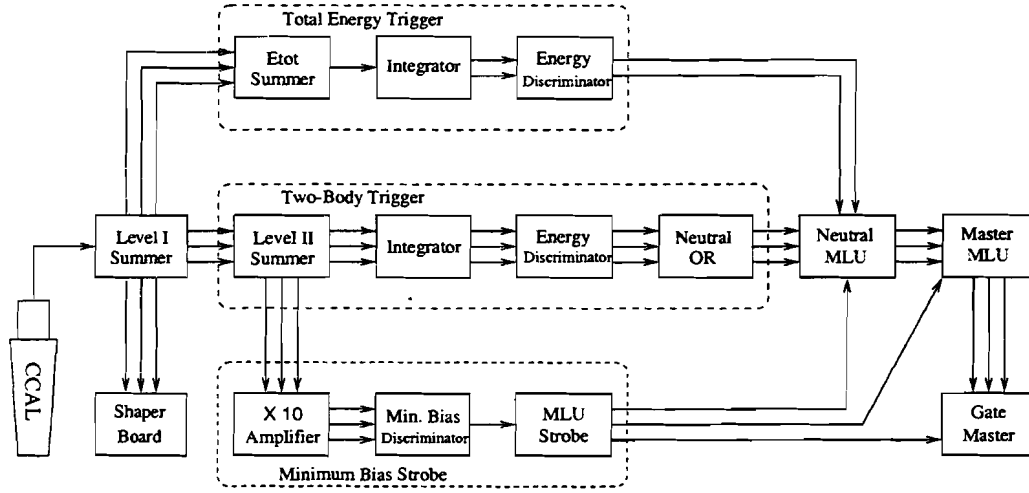


Figure 3.3: Schematic of the E835 Neutral Trigger

The large number of CCAL blocks made it unreasonable to directly trigger on each block's signal. Therefore, a two stage summer (level I and level II) was used to bring the total number of signals for input to the logic down to 40. These 40 signals would be the result of dividing the CCAL into 40 super-blocks and summing the signals of all blocks in the super-block. Each super-block consisted of nine wedges and five rings (except for the first super-ring which spans from rings one to four). A super-block had a one CCAL channel overlap (both wedge and ring)

Super-Wedge Number	Wedge Numbers For a Ring
1	1-9
2	9-17
3	17-25
4	25-33
5	33-41
6	41-49
7	49-57
8	57-1

Table 3.2: Blocks in a Ring Summed to Make a Super-Wedge

with the adjacent super-blocks to avoid the trigger inefficiency caused by electrons or photons hitting a boundary thus causing the electromagnetic shower to spread over more than one super-block (and perhaps then not passing the discriminators).

The summing patterns of the level I and level II summers are listed in tables 3.2 and 3.3. The segmentation of the 40 super-blocks is shown in figure 3.4.

Super-Ring Number	Ring Numbers For a Super Wedge
1	1-4
2	4-8
3	8-12
4	12-16
5	16-20

Table 3.3: Rings in a Super-Wedge Summed to Make a Super-Block.

In section 2.3.4 it was noted that the CCAL blocks had four different size PMTs. Since each size PMT has its own pulse shape characteristics, and the last super-ring included three different sizes of PMT, it was difficult to set discriminator thresholds based on the signal's amplitude, i.e. the same amount of energy may then give a

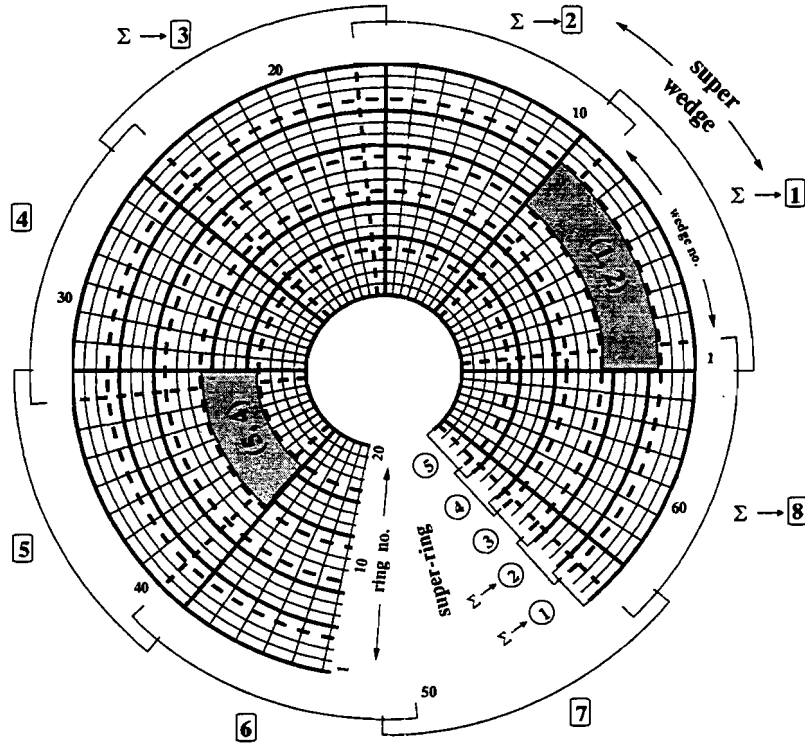


Figure 3.4: Beam's View of the Central Calorimeter. Structure of the 40 overlapping super-blocks in a 5 (Θ) \times 8 (Φ) array. The overlaps are indicated by the dashed lines and are described in tables 3.2 and 3.3. Super blocks (Φ, Θ) = (1,2) and (5,5) are shaded.

trigger in one block and not another. The total charge within a pulse, however, was proportional to the total energy deposited in that CCAL block, and furthermore, was independent of the pulse shape. Thus, integrator modules were used to convert the 40 super blocks' outputs to signals with amplitudes proportional to the total charge.

The 40 signals were then discriminated and fed to the neutral-OR modules to form eight CCAL octant signals (if at least one super-block in a super-wedge was above threshold a neutral-OR signal was created for that super-wedge octant). These eight signals, and the discriminated ETOT-HIGH and ETOT-LOW signals, were sent to the NMLU for simple pattern recognition to provide four level 1 neutral trigger signals, PBG1, PBG3, ETOT-HIGH, and ETOT-LOW, which were sent to the MMLU. The performance of the neutral trigger during E835 running is described in appendix A.

Level I Summer

There are 20 level I summers located in the E835 detector area. Each summer took as input one of the 64 signals from a particular CCAL ring. The input signal came directly from the PMT output of a CCAL block. After passing through a resistor network, 94% of the signal was sent to a CCAL shaper board where it was reshaped and sent to the FERA ADCs. The remaining 6% of the signal was split in half and used to form the super-wedge sums and the ring energy sum. For each overlap channel, half the signal was sent to each of its super-wedge sums. For the non-overlap channels half of the signal was sent to its super-wedge sum while the other half went into the ring energy sum. Both sums were inverted and amplified. The super-wedge sums were then sent to one of the 160 level II summer inputs. The

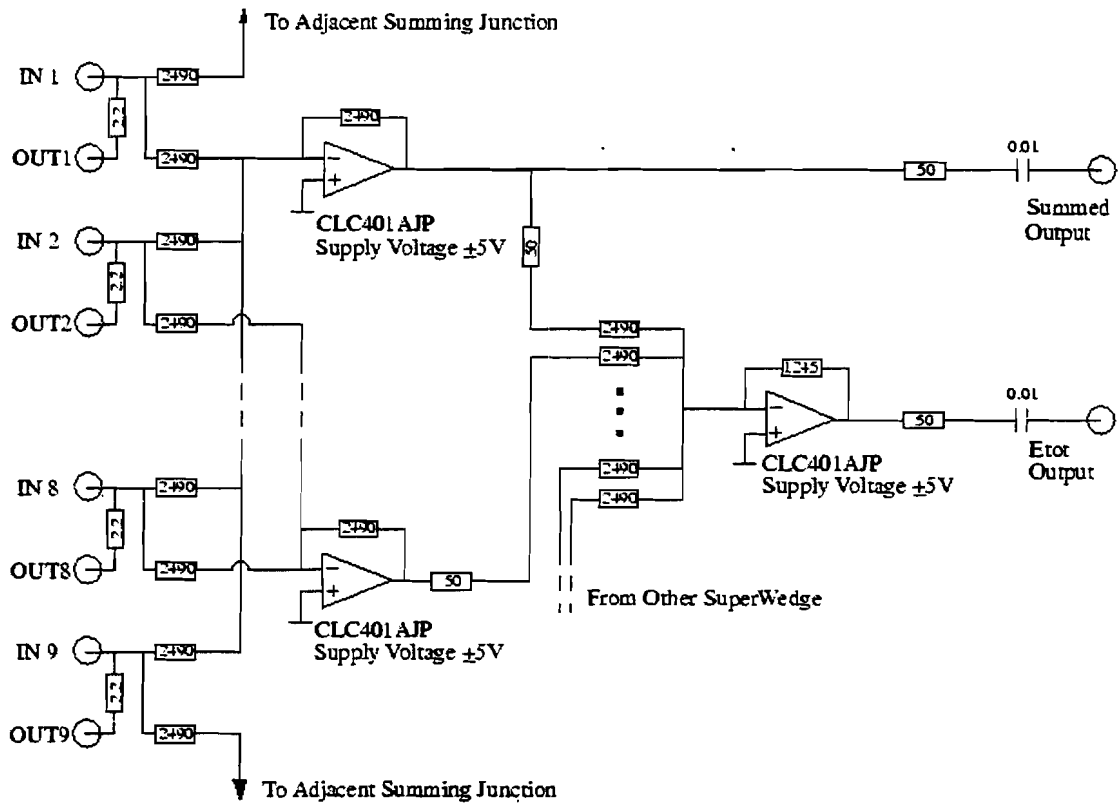


Figure 3.5: Circuit Diagram for the Level I Summers. Resistor values are in ohms and capacitor values are in pF.

eight signals meant to be the ring energy sums were then added to eight copies of the super-wedge sums. This signal was inverted by another amplifier to form the ring energy sum which was sent to the total energy summer. The circuit diagram of the level I summer is shown in figure 3.5.

Level II Summer

There were eight level II summers located in the E835 electronics/run control room, each of which processed the 20 signals (one per ring) from one of the eight super-wedges formed by the level I summers. Each input signal was split by a resistor network which sent 5% of the signal to a summing junction and the remaining 95% to an inverting feed through circuit to be used in forming the minimum bias strobe.

The summing circuit for the level II summers was similar to that of the level I summers. The module formed five overlapping sums by summing the 20 input signals according to the pattern listed in table 3.3. The group of five rings was a super-ring. Unlike the level I summer, the 20 inputs of the level II summer were weighted by the summing resistors in such a way as to equalized the expected energy deposited within the angular range of a super-ring (based on two-body kinematics). The weighting allowed for a cleaner threshold determination. This is demonstrated in figure 3.6 where a Monte Carlo simulation has been used to generate the decay kinematics for $\bar{p}p \rightarrow J/\psi \rightarrow e^+e^-$. The weighting factors and resistor values are listed in table 3.4. One set of weighting resistors worked for the entire range of the experiment. The signals of the overlapping channels were weighted differently for each of the two sums to which they contribute.

The summed signals were then inverted and amplified. This resulted in 40 super-blocks which contained all the energy deposited in the CCAL. The super-block sums

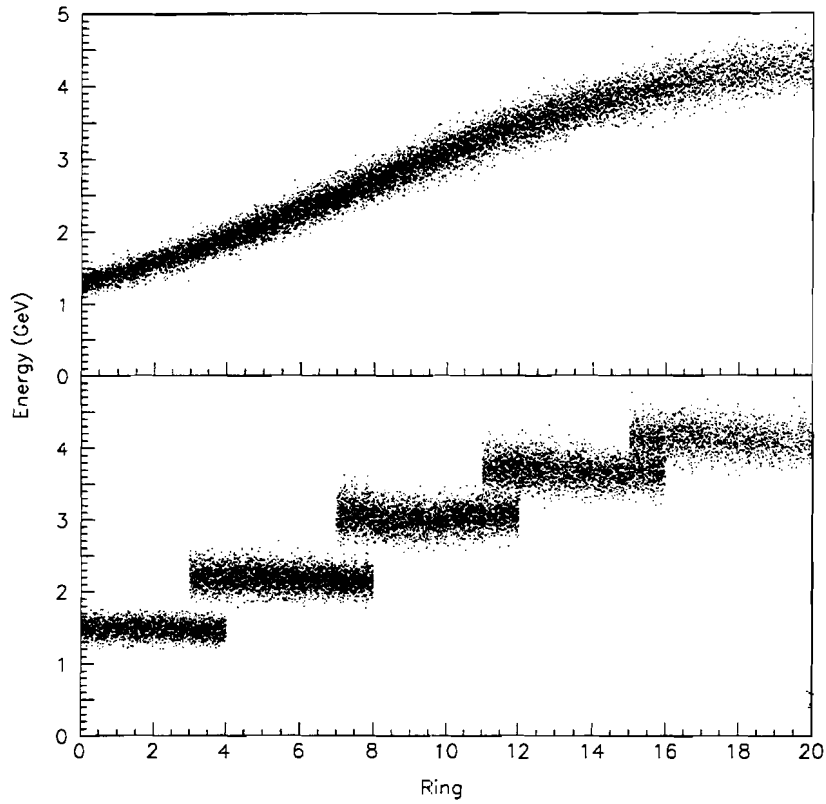


Figure 3.6: Monte Carlo simulation of the kinematics for $\bar{p}p \rightarrow J/\psi \rightarrow e^+e^-$. The electron energy as a function of ring number is shown in the top plot without the weighting factors and in the bottom plot with the weighting factors.

Input Channel	Resistor Value (ohm)	Relative Weight
1	2260	1.10
2	2490	1.00
3	2740	0.91
4	3090,2050	0.81,1.21
5	2260	1.10
6	2490	1.00
7	2740	0.91
8	3010,2100	0.83,1.19
9	2320	1.07
10	2490	1.00
11	2610	0.95
12	2740,2260	0.91,1.10
13	2370	1.05
14	2490	1.00
15	2610	0.95
16	2670,2370	0.93,1.05
17	2430	1.02
18	2490	1.00
19	2550	0.98
20	2610	0.95

Table 3.4: Values of the Weighting Resistors and the Relative Weights for each Input Channel of the Level II Summer. The overlapping channels had two weighting resistors. The ratios are calculated relative to the central channel in each sum (i.e. channel 2, 6, 10, 14 or 18)

were fanned out three times. The first output was sent to the next stage of the neutral trigger (see next section). The second was sent to ADCs to monitor the performance of the trigger and the settings of the energy thresholds. The third was also sent to the ADCs but with a 100 ns delay relative to the second to serve as a pretrigger snapshot indicating the presence of tails from previous interactions embedded in a particular event.

The feed through signals, which contained 95% of the input charge, were amplified ten times and sent to a set of minimum bias discriminators whose thresholds were set at 100 MeV. The low thresholds were intended to minimize the time jitter of the discriminator outputs. These outputs were then summed together and the resulting signal was discriminated with a threshold corresponding to two hits in the CCAL. This signal formed the minimum bias strobe which was fanned out to different MLUs and to the gatemaster.

Integrator

Since the super-block signals included contributions from different sized PMTs with different pulse shapes, setting a common threshold on the pulse amplitude was not trivial. The total charge contained within the pulse, however, was independent of the pulse shape and was proportional to the energy deposited in the CCAL blocks. In addition, the total charge experiences smaller fluctuations than the pulse amplitude. For these reasons, an integrating circuit was developed to process the signals from the level II summers. The input current was clipped with a 16 ns cable connected to the back of the integrator module thus producing a bipolar signal. The bipolar signal was integrated with a time constant of 500 ns. In spite of the long integration time constant, the clipping cable was able to bring the output from the integrator back

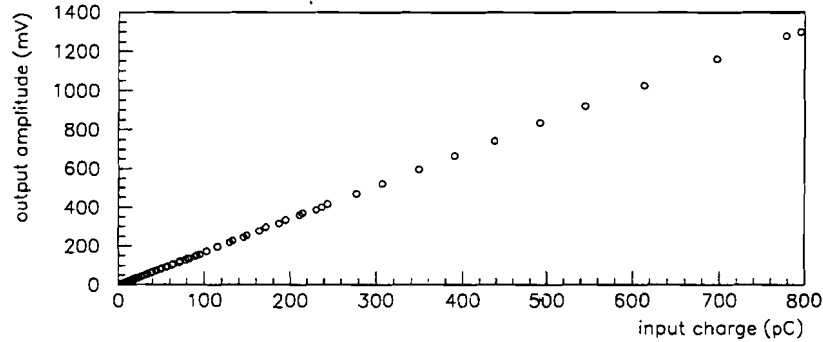


Figure 3.7: Integrator

to its baseline in about 100 ns. The amplitude of the output pulse was proportional to the total charge contained in the input pulse. Figure 3.7 shows the dependence of the output pulse amplitude on the input charge. It was linear up to about 500 pC which corresponded to about 8 GeV of energy deposited in the CCAL.

3.2.3 Energy Discriminators

The 40 outputs from the integrators were sent to the energy discriminators. The eight super-block signals from the same super-ring went to the same discriminator. Each discriminator had its threshold set according to the amount of energy that would be deposited in it for a particular two-body decay at the current center of mass energy. The channel to model was chosen based on the charmonium resonance that was nearest.

The energy thresholds were calculated with the above method by Monte Carlo simulations. The lowest energies (defined as the mean minus 3σ) were selected as the thresholds and increase with each successive super-ring. The thresholds were

Channel	Energy threshold (GeV) (60% of min. energy)					Energy discriminator threshold (mV)				
	SR1	SR2	SR3	SR4	SR5	SR1	SR2	SR3	SR4	SR5
$\eta_c \rightarrow \gamma\gamma$	0.70	1.05	1.46	1.79	—	52	81	119	146	—
$\psi \rightarrow e^+e^-$	0.72	1.08	1.54	1.91	—	53	84	125	155	—
$\chi_0 \rightarrow \gamma\psi$	0.61	0.95	1.41	1.81	2.09	45	73	115	147	217
$\chi_1 \rightarrow \gamma\psi$	0.57	0.89	1.34	1.74	2.03	42	69	109	142	212
$^1P_1 \rightarrow \pi^0\psi$	0.56	0.88	1.33	1.73	2.02	41	69	108	141	210
$\chi_2 \rightarrow \gamma\psi$	0.54	0.87	1.31	1.70	1.99	40	67	106	138	207
$\eta'_c \rightarrow \gamma\psi$	0.53	0.84	1.28	1.68	1.97	39	65	104	136	205
$\psi' \rightarrow X\psi$	0.55	0.88	1.35	1.80	2.17	41	68	110	146	225

Table 3.5: Energy and Discriminator Thresholds Values for Super-Blocks. For the η'_c region the value is calculated at 3.594 GeV in the center of mass. For $\eta_c \rightarrow \gamma\gamma$ and $J/\psi \rightarrow e^+e^-$, the thresholds for super-ring five are irrelevant since this region is kinematically inaccessible.

calculated in 5 MeV steps in center of mass energy to ensure consistency over the energy range of the experiment (2.9 GeV to 4.2 GeV). Since a photon (or electron) hitting the boundary of a CCAL block could loose up to 40% of its energy to the inactive material, the real energy thresholds used in the energy discriminators were set as 60% of the calculated values. The calculated thresholds, the channel they were based on, and the energy discriminators' set thresholds are listed in table 3.5.

Neutral-OR

The 40 outputs of the discriminators were then sent to the Neutral-OR module to form the eight CCAL octant signals. Each octant signal was the OR of the five super-ring signals from the same super-wedge and represented that there was energy deposition above threshold in that octant. The eight ECL octant signals were sent to the neutral MLU.

Total Energy Trigger

The total energy summer was identical in construction to the level I summers. It summed the 20 ring sums from the level I summers and used the output to form the total energy signal. As mentioned before, this signal contained contributions from different sized PMTs and thus needed to be integrated. After the integration, the total energy signal was fanned out twice and sent to discriminators whose thresholds were set at 70% and 80% of the total center of mass energy, respectively. The outputs were then sent to the neutral MLU.

Neutral MLU

In the NMLU a pattern recognition operation was performed on the eight CCAL octant signals. This lead to the creation of the PBG1 and PBG3 triggers. PBG1 required two large back to back energy deposits in opposing CCAL super-wedges. PBG3 required large energy deposits in a super-wedge and either its opposing super-wedge or a super-wedge adjacent to the opposing one. The ETOT-HIGH and ETOT-LOW were passed through to the NMLU output. The inputs and outputs of the NMLU are listed in table 3.6.

3.3 Master MLU

The level 1 triggers from the charged, $\phi\phi$, and neutral triggers, as well as some charged veto signals from the charged trigger, were used in the master MLU to build the level 2 triggers. The PBG3 (from the NMLU) and e^+e^- (from the CMLU) made up the e^+e^- trigger. The PBG1 (from the NMLU) and the charged veto made up the $\gamma\gamma$ trigger etc. The inputs and outputs of the master MLU are listed

input channel	Description	output channel	Description
1	CCAL octant 1	1	PBG1
2	CCAL octant 2	2	PBG3
3	CCAL octant 3	3	ETOT-HIGH
4	CCAL octant 4	4	ETOT-LOW
5	CCAL octant 5	5	empty
6	CCAL octant 6	6	empty
7	CCAL octant 7	7	empty
8	CCAL octant 8	8	empty
9	ETOT-HIGH		
10	ETOT-LOW		
11-16	empty		

Table 3.6: The Inputs and Outputs of the NMLU

in table 3.7 and are explained below.

The input signals have been previously explained. The outputs were:

- $e^+e^- = (e^+e^-(1)) \times PBG3 + (e^+e^-(2))$. Two electron tracks with two large loosely back to back energy deposits in the CCAL or two back to back electron tracks from the charged trigger.
- $\bar{p}p\ 90^\circ = PMLU2 \times CMLU4$ (i.e. $PMLU$ output 1 \times $CMLU$ output 4).
- $\phi\phi = PMLU1 \times CMLU3$.
- $\gamma\gamma = PBG1 \times \overline{(H1 \times H2')_OR} \times \overline{FCH_OR}$. Back to back CCAL trigger with charged veto in the central and forward regions.
- ETOT-HIGH veto = ETOT-HIGH $\times \overline{(H1 \times H2')_OR} \times \overline{FCH_OR}$. ETOT-HIGH with charged-veto in the central and forward regions.

input channel	Description	output channel	Description
1	PBG1	1	e^+e^-
2	PBG3	2	$\bar{p}p$ 90°
3	ETOT-HIGH	3	$\phi\phi$
4	ETOT-LOW	4	$\gamma\gamma$
5	(H1 \times H2')_OR	5	ETOT-HIGH veto
6	FCAL_OR	6	$\bar{p}p$ 55°
7	H2 > 2	7	ETOT-HIGH no veto
8	FCH_OR	8	ETOT-LOW veto
9	CMLU1 ($e^+e^-(1)$)		
10	CMLU2 ($e^+e^-(2)$)		
11	CMLU3 ($\phi\phi$)		
12	CMLU4 ($\bar{p}p$)		
13	CMLU5 (not used)		
14	PMLU1 ($\phi\phi$)		
15	PMLU2 ($\bar{p}p$ 90°)		
16	PMLU3 ($\bar{p}p$ control)		

Table 3.7: The Inputs and Outputs of the MMLU

- $\bar{p}p$ 55° = $PMLU3 \times CMLU4$.
- ETOT-HIGH no veto = $ETOT-HIGH \times \overline{H2 > 2}$.
- ETOT-LOW veto = $ETOT-LOW \times \overline{(H1 \times H2')_OR} \times \overline{FCH_OR}$.
ETOT-LOW with charged-veto in the central and forward regions.

3.4 Gatemaster

The gatemaster was used for generating a gate signal thus enabling the DAQ read-out system to collect data from the CAMAC modules and pass them to PRUDE. It had fourteen trigger inputs and was strobed by the minimum bias signal. After the

gate signal was generated, the gatemaster entered INHIBIT mode for about $10\ \mu\text{s}$ to allow the CAMAC modules to reset. Any strobe arriving during that period was ignored. The gatemaster maintained a trigger counter for each trigger input. The trigger counter was used by PRUDE to autopass a percentage of events in order to check trigger efficiencies.

The fourteen input triggers are listed in table 3.8. Eight of them were from the MMLU. The other six were special triggers for efficiency checking and monitoring. These triggers were:

- Laser Monitor: pulsed every 10 sec. to illuminate all CCAL blocks. The laser signal events were used to monitor the stability of the CCAL's gains.
- Silicon Strobe. Not Used.
- Minimum Bias: Minimum bias triggers used to check trigger efficiency.
- Random Gate: Generated by a 10kHz pulser. It was used to check the rate dependence of analysis cuts by looking at pileup in the detector.
- FCAL Cosmic Ray. Not Used.
- High Rate Minimum Bias: High rate minimum bias triggers used for debugging.

3.5 PRUDE Software Trigger

The event data and the trigger information were processed by the software trigger (PRUDE) in order to do quick online event reconstruction and filtering. This was to determine whether a specific event should be recorded or discarded. Each passed

input channel	Description	input channel	Description
1	e^+e^-	9	Laser Monitor
2	$\bar{p}p$ 90°	10	Silicon Strobe
3	$\phi\phi$	11	empty
4	$\gamma\gamma$	12	Minimum Bias
5	ETOT-HIGH veto	13	Random Gate
6	$\bar{p}p$ 55°	14	FCAL Cosmic Ray
7	ETOT-HIGH no veto	15	High Rate Minimum Bias
8	ETOT-LOW veto	16	empty

Table 3.8: The Inputs of the Gatemaster

event was assigned a special PRUDE ID, which could be used for fast offline event filtering. The passed data was logged onto one of three data streams: charged events (GK), $\phi\phi$ events (GP) or neutral events (GN). A subset of GK and GN data which contain “gold” events (defined below) were logged onto disk for quick access. Another subset of GK and GN data were logged onto the CCAL calibration tapes (GNA) which were used in calibrating the CCAL gains.

The software triggers in PRUDE are listed in table 3.9, along with their priorities, PRUDE IDs, and data streams to which they were written. The first fifteen are the autopass triggers which PRUDE passed to the data streams automatically. For the other triggers, PRUDE first used the CCAL information and online clusterization to find clusters and calculate their energies, masses and positions. PRUDE then calculated the invariant mass of cluster pairs and together with the trigger information made the final trigger id decision. If the event satisfied more than one software trigger, the one with the highest priority (lowest priority number) was assigned. The software triggers for the non-autopass events are explained below:

- goldee: GM1 (e^+e^-) with at least one invariant mass pair > 2.2 (2.0) GeV for

above (below) the antiproton beam transition point (about 3.4 GeV).

- goodee: GM1 with invariant mass pair > 2.0 GeV but below the goldee invariant mass cut.
- elec: GM1 events not tagged as goldee or goodee.
- $\phi\phi$: GM3 ($\phi\phi$) events selected based on the kinematics and opening angles as well as occupancy of hodoscopes and scintillating fiber bundles.
- goldgg: GM4 ($\gamma\gamma$) or GM5 (Etot-high with veto) with at least one invariant mass pair > 2.7 (2.5) GeV for above (below) transition.
- goodgg: GM4 or GM5 with at least one invariant mass pair > 2.5 GeV but below the goldgg invariant mass cut.
- etainvm: GM4 or GM5 with at least one exclusive η , less than six CCAL clusters, and at least one invariant mass pair > 2.0 GeV.
- piinvm: GM4 or GM5 with at least one exclusive π^0 , less than six CCAL clusters, and at least one invariant mass pair > 2.0 GeV.
- cmainvm: GM4 or GM5 where the largest energy cluster could be split (cluster mass > 100 MeV), less than five CCAL clusters, and at least one invariant mass pair > 2.0 GeV.
- cmbinvm: GM4 or GM5 where the second largest energy cluster could be split, less than five CCAL clusters, and at least one invariant mass pair > 2.0 GeV.
- invmass: GM4 or GM5 with at least one invariant mass pair > 2.0 GeV but not tagged as goldee, goodee, etainvm, piinvm, cmainvm, or cmbinvm.

- etaetot: GM4 or GM5 with at least one exclusive η , less than six CCAL clusters, all invariant mass pairs < 2.0 GeV, and 90% of the total energy in the CCAL.
- pietot: GM4 or GM5 with at least one exclusive π^0 , less than six CCAL clusters, all invariant mass pairs < 2.0 GeV, and 90% of the total energy in the CCAL.
- cmaetot: GM4 or GM5 where the largest energy cluster could be split, less than five CCAL clusters, all invariant mass pairs < 2.0 GeV, and 90% of the total energy in the CCAL.
- cmbetot: GM4 or GM5 where the second largest energy cluster could be split, less than five CCAL clusters, all invariant mass pairs < 2.0 GeV, and 90% of the total energy in the CCAL.
- etotsoft: GM4 or GM5 events with all invariant mass pairs < 2.0 GeV and 90% of the total energy in the CCAL but not tagged as etaetot, pietot, cmaetot, or cmbetot.
- neutr: all GM4 and GM5 events not tagged previously.

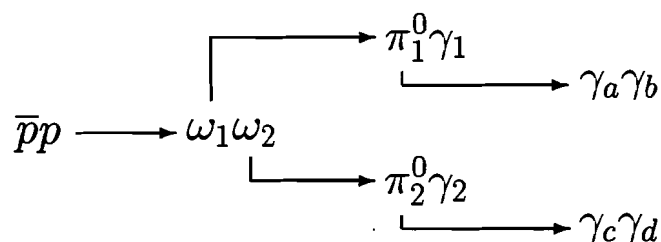
Priority	PRUDE ID	Name	Written to
1	90	GM9: Laser Monitor	GK
2	120	GM12: Minimum Bias	GK
3	130	GM13: Random Gate	GK
4	70	GM7: Etot-High no veto	GK
5	140	GM14: FCAL Cosmic Ray	GK
6	80	GM8: Etot-low veto	GK
7	150	GM15: High Rate Minimum Bias	GP
8	10	GM1: e^+e^-	GK
9	40	GM4: $\gamma\gamma$	GK
10	100	GM10: Silicon Strobe	GP
11	30	GM3: $\phi\phi$	GP
12	20	GM2: $\bar{p}p$ 90°	GP
13	60	GM6: $\bar{p}p$ 55°	GP
14	50	GM5: Etot-high veto	GK
15	110	GM11: All triggers	GK
16	13	goldee	GK Gold
17	12	goodee	GK
18	11	elec	GK
19	31	$\phi\phi$	GP
20	48	goldgg	GK GNA Gold
21	47	goodgg	GK GNA
22	42	etainvm	GK GNA
23	43	piinvm	GK GNA
24	44	cmainvm	GK GNA
25	45	cmbinvm	GK GNA
26	41	invmass	GK
27	52	etaetot	GN GNA
28	53	pietot	GN GNA
29	54	cmaetot	GN GNA
30	55	cmbetot	GN GNA
31	51	etotsoft	GN
32	170	neutr	GN

Table 3.9: PRUDE IDs, Priorities, Names, and Destination Data Streams

Chapter 4

$\omega\omega$ Event Selection

The decay channel under study is $\bar{p}p \rightarrow \omega\omega$ with each ω decaying via $\pi^0\gamma$ to three final state photons. The following diagram illustrates the notation used throughout the remainder of the chapters:



The process of selecting $\omega\omega$ events began with choosing the proper event class subset from the 8 mm data tapes. Included in this process was the creation of data summary tapes. Events were then examined to determine whether they were kinematically consistent with $\omega\omega$ decays. A large amount of non- $\omega\omega$ data remained after this initial selection process, and thus, a method for background subtracting to obtain clean $\omega\omega$ was employed. The method required knowing the relevant parameters

for the $\omega\omega$ angular distribution. This information could then be used to search for specific charmonium resonances, i.e. $\bar{p}p \rightarrow \bar{c}c \rightarrow \omega\omega$, based upon their spin and parity.

4.1 Preliminary $\omega\omega$ Candidate Selection

The following list shows the criteria used for preliminary selection of $\omega\omega$ candidate events. The list elements are explained in detail in the subsections that follow.

1. Data was taken from the 6 cluster Neutral Data Summary Tapes.
2. Events were required to come in on the total energy trigger (GM5).
3. A fiducial volume cut rejected events with clusters centered in rings 1, 19, or 20.
4. (a) There must have been exactly two unique two cluster invariant masses, $m_{2cluster}$, such that $|m_{2cluster} - m_{\pi^0}| < 35$ MeV.
 (b) For all other two cluster combinations, $|m_{2cluster} - m_{\pi^0}| > 55$ MeV.
 (c) For the two clusters not considered π^0 daughter particles (i.e. γ_1 and γ_2 on the page 94 diagram), $|m_{2cluster} - m_{\eta}| > 75$ MeV.
5. Events must fit a $2\pi^0 2\gamma$ hypothesis with a probability on the χ^2 greater than 5%.
6. There must exist at least one pairing of the neutral pions and photons such that $|m_{\pi^0\gamma} - m_{\omega}| < 300$ MeV for both groups.
7. A cut on the center of mass polar angle of the ω required $|\cos\theta^*| \leq 0.28$.

4.1.1 Neutral Data Summary Tapes

A subset of E835 data was made in which events were classified as neutral, meaning that any potential all neutral final state events (i.e., all CCAL clusters were identified as photons) were written in a summarized form to a Neutral Data Summary Tape (NDST) and classified by the number of intime or undetermined clusters in the central calorimeter. The process for making NDSTs is described in Appendix B.

For this analysis the six cluster NDST dataset was used. Real $\omega\omega$ events where one or more final state photons missed the calorimeter or did not register as a cluster since they were below the CCAL energy thresholds would not be included in this analysis. Corrections for these missed events were considered in the Monte Carlo simulation (see section 4.4.6).

Another possibility for losing events when using the six cluster NDSTs is when the event had 5 or less intime clusters and enough undetermined clusters to total more than six in the CCAL but enough of the undetermined clusters were associated with the $\omega\omega$ event to make six true clusters. By running the $\omega\omega$ analysis on the higher cluster NDSTs and allowing different combinations of the excess undetermined clusters to count in the six cluster set, this loss was found to be negligible (less than 1% of the six cluster dataset).

4.1.2 Total Energy Trigger Selection

Any recorded all neutral final state event would have to come in on, by definition, either the total energy trigger (GM5), the back to back trigger (GM4), or both. All candidate $\omega\omega$ events were required to come in on the total energy trigger GM5 (see section 3.3 and table 3.7 for the descriptions of GM4 and GM5). Real $\omega\omega$ events with all six clusters hitting the CCAL should register a total energy trigger. This

trigger was better than 95%, and for most energies better than 98%, efficient (see Appendix A).

Although there is no true physical reason to exclude events that came in on only the GM4 trigger, there was a large group of runs where the GM4 efficiency was unknown due to a mistimed neutral trigger discriminator (see Appendix A). This along with the very small percentage of real $\omega\omega$ data that would fail to obtain a total energy trigger led to the decision to use only GM5 triggers. Table 4.1 shows, for a subset of data in the η_c center of mass energy region, the numbers of events passing the preliminary $\omega\omega$ selection based on the trigger they came in on.

Gatmaster id	# of Events Passing Preliminary Selection	% of Total Events (in this sample)
GM4 only	6	0.03
GM5 only	9960	51.22
GM4 and GM5	9480	48.75

Table 4.1: Number of Events Passing the Preliminary $\omega\omega$ Selection and Their Percentage of the Total Sample Set for each Trigger Type

4.1.3 Fiducial Volume Cut

Any clusters whose position was determined to be in rings 1, 19, or 20 was discarded due to the inability to accurately determine the gain constants for the blocks in these rings. Reference [51] gives a more in depth description of gain constant calculations and the difficulties with calculating gains for end rings of the CCAL.

4.1.4 Cluster Invariant Mass Cuts

With the copious production of multi- π^0 states coming from the $\bar{p}p$ annihilation continuum, and with E835's ability to efficiently identify neutral pions, it became important to not only select potential $\omega\omega$ events by checking for π^0 invariant masses among the clusters (to identify $\omega \rightarrow \pi^0\gamma$ decays) but also to make sure that the other clusters were not from decays of pions.

To see how well neutral pions could be identified in the six cluster data sets, for each event from a subset of the NDSTs, the invariant masses of all possible combinations of two clusters were calculated. Figure 4.1 shows these values histogrammed for all six cluster NDST events with center of mass energy from 2.912 GeV to 2.985 GeV.

It was required that of the six clusters, four clusters and only four clusters be identified as photons from two distinct π^0 decays. The requisite for this was that the invariant mass of the photons be within 35 MeV of the π^0 mass (35 MeV lines are shown in figure 4.1). These photons are labeled $\gamma_{a,b,c,d}$ in the diagram at the beginning of this chapter and the pions are labeled $\pi_{1,2}^0$.

To exclude the large background from $3\pi^0$ or $4\pi^0$ events (feeding down by loss of two photons outside the CCAL or below the cluster energy threshold) masquerading as $\omega\omega$ events, it was required that no other two clusters come within 55 MeV of the π^0 mass. This also eliminated ambiguous events where one cluster could make a pion with two separate clusters. The larger 55 MeV cut was made to ensure that the events in the tails of the π^0 distribution as shown in figure 4.1 were completely removed. Events that were lost by this cut, but where the two photons causing the rejection were not really from neutral pions, i.e. the background under the pion peak, were corrected for by the Monte Carlo simulation (see section 4.4.6). Four pion events where a photon from two different pions was not detected could still

exist after these cuts. They uniformly populate the background, however, and so are removed by the background subtraction (section 4.3).

Figure 4.2 shows all combinations of two clusters' invariant masses where the pion peak has been removed to allow closer inspection of the higher mass part of the distribution. Evident on the plot is an η peak at 0.547 GeV, a pseudo- ω peak (where a soft photon was not recorded in the CCAL), and an η' peak at 0.958 GeV. Only the η peak was considered large enough to require removal. It was only visible in the invariant mass plot of the photons not already associated with a pion, that is, $m_{\gamma_1\gamma_2}$. These are probable $\pi^0\pi^0\eta$ events. They were removed by requiring that $m_{\gamma_1\gamma_2}$ was at least 75 MeV from the η mass.

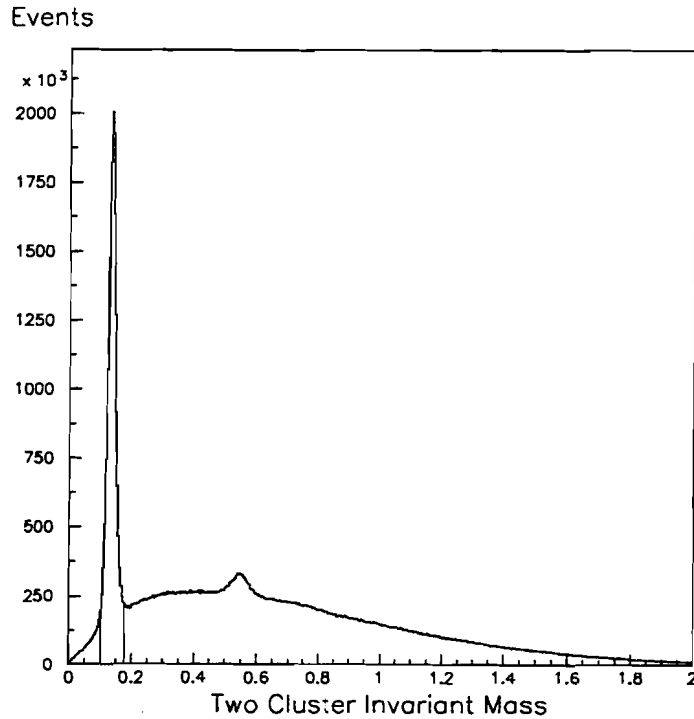


Figure 4.1: Invariant Mass of all Two Cluster Combinations for E_{cm} Less than 2.985 GeV. The vertical lines are at $m_{\pi^0} \pm 0.035$ GeV.

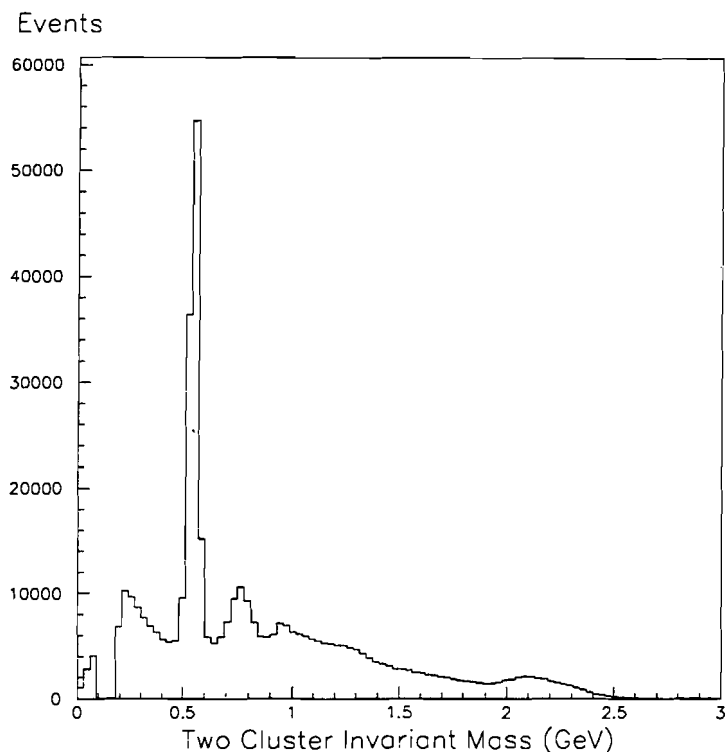


Figure 4.2: Invariant Mass of all Two Cluster Combinations for E_{cm} Less than 2.985 GeV Excluding any Mass within 35 MeV of the π^0 . The η (547 MeV), pseudo- ω (slightly less than 782 MeV), and η' (958 MeV) peaks are visible.

After the cuts described above, the omega peak becomes evident in a plot of all-three cluster combinations' invariant masses. Figure 4.3 shows the invariant masses of all three-cluster combinations for each event from the NDST data subset in the η_c energy region. Figure 4.4 shows the same distribution after cuts 1 through 4 (see page 95) have been applied.

4.1.5 Fit to $2\pi^0 2\gamma$ Hypothesis

It will be shown in section 4.3 that there was a large background of non- $\omega\omega$ events, even after the cuts carried out as mentioned previously. Thus, it was not practical to

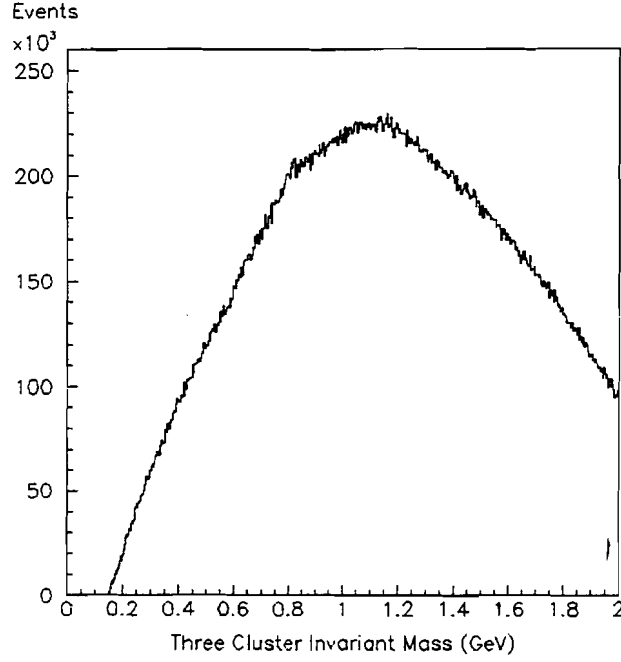


Figure 4.3: Invariant Mass of all Three Cluster Combinations in the η_c Energy Region

do a kinematic fit to a $\bar{p}p \rightarrow \omega\omega \rightarrow 2\pi^0 2\gamma \rightarrow 6\gamma$ hypothesis. Even with a fairly large probability cut on the χ^2 of the fit, non- $\omega\omega$ background events with both candidate $\pi^0\gamma$ invariant masses close to the ω mass pass the fit. This would make it impossible to interpolate the background under the $\omega\omega$ mass peak and subtract it. Instead, with the above mentioned cluster identifications, a fit was done on each event to a $2\pi^0 2\gamma$ hypothesis using SQUAW [52].

The kinematical fit using SQUAW is a χ^2 minimization of

$$\chi^2 = \sum_{i=1}^{18} \frac{(x_{i,fit} - x_{i,measured})^2}{\sigma_{x,i}^2} \quad (4.1)$$

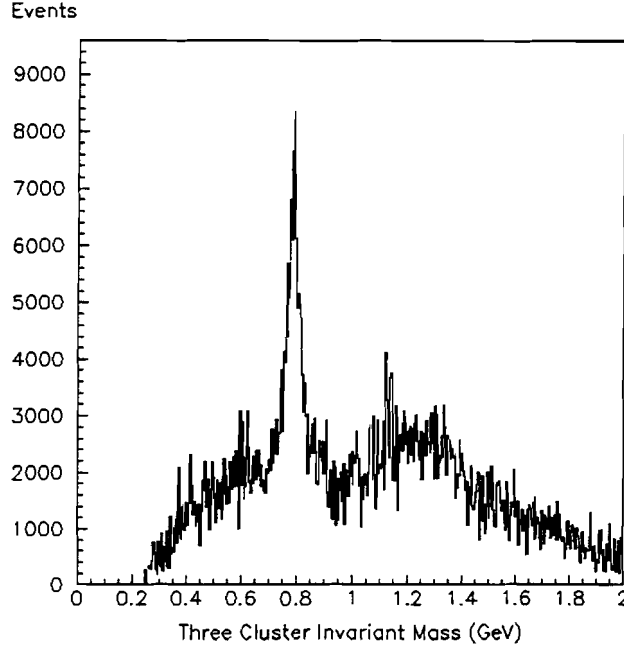


Figure 4.4: Invariant Mass of all Three Cluster Combinations for Events in the η_c Energy Region (Cuts 1-4 Have Been Applied). The ω mass peak is clearly visible.

where the x_i are the energies and the angles, ϕ and $\tan \theta$ (called the dip), of the 6 measured photon clusters. The $\sigma_{x,i}$ were determined from the errors on cluster energies and angles. Constraints were added requiring that two pairs of the clusters form pion masses. Energy and momentum conservation was required as well. Under the assumption that the measured values are distributed as Gaussian functions with variance $\sigma_{x,i}^2$, the probability for obtaining a value of χ^2 from a random $\omega\omega$ candidate, $P(\chi^2)$, is given by [53, pages 117-120]

$$P(\chi^2) = \frac{e^{-\chi^2/2} \left(\frac{\chi^2}{2}\right)^{\nu/2-1}}{\Gamma\left(\frac{\nu}{2}\right)} \quad (4.2)$$

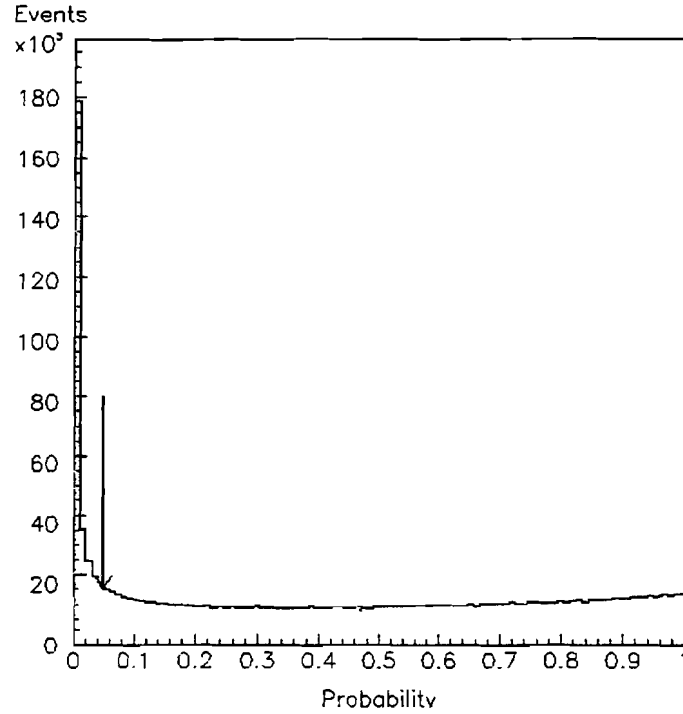


Figure 4.5: χ^2 Probability of Fit for $2\pi^0 2\gamma$ Hypothesis for a Typical Subset of the Six Cluster Data. The arrow is at $P(\chi^2) = 5\%$.

where ν is the number of terms in the χ^2 sum. Figure 4.5 shows the probability for a typical subset of the six cluster data. The arrow points to 5% which was where the goodness of fit cut was taken.

4.1.6 $\pi^0\gamma$ Pairings

Since the objective was to identify $\omega\omega$ candidate events, a cut was made on the invariant masses of the $\pi^0\gamma$ pairs for the events that passed all previous cuts. As was mentioned in the previous section, the size of the non- $\omega\omega$ background compared to the $\omega\omega$ signal was significant, thus, rather than making a tight cut on the invariant

mass of a $\pi^0\gamma$ pair, a large mass window about the ω mass was allowed so that the shape of the background under the $\omega\omega$ signal could be surmised. Events in which at least one *pairing* of the pions and photons led to an invariant mass such that $m_{\pi_1^0\gamma_1}, m_{\pi_2^0\gamma_2} \in [0.482, 1.082]$, i.e. within 300 MeV of m_ω , were kept. Events were rejected if there was not at least one topology such that both pairs had invariant masses within 300 MeV of m_ω .

Occasionally events had both combinations of π^0 's and γ 's invariant masses falling within 300 MeV of the ω mass. In these cases, the event was fit to a $\bar{p}p \rightarrow \omega\omega \rightarrow 2\pi^0 2\gamma \rightarrow 6\gamma$ hypothesis using SQUAW. The “correct” pairing was chosen based on which combination had the highest probability of fit, with the following caveat: if both pairings gave a fit probability of less than 5% or greater than 10%, the event was considered ambiguous and was rejected. The number of events that could be considered truly ambiguous, but that did not get thrown out by this cut (e.g., the two pairings have probabilities of fit of 8% and 9%, respectively) was negligible (less than 0.1% of the data).

4.1.7 $|\cos\theta^*|$ Cut

The cut that was imposed on the ω 's polar angle in the $\bar{p}p$ center of mass frame had two purposes. As the polar angle in the center of mass frame for an ω from a $\bar{p}p \rightarrow \omega\omega$ decay decreases (i.e. approaches the beam axis), the backward ω in the lab will become lower in energy. Since the omegas already have a large mass compared to the total available energy, this will create ever wider $\omega \rightarrow \pi^0\gamma$ opening angles as well as lower π^0 and γ energies. This makes the acceptance for the desired decay channel decrease significantly, both from final state particles falling outside the calorimeter's geometrical acceptance and from low energy clusters not being detected. Low energy

final states also have larger cluster parameter errors. These situations cause a great decrease in the efficiency of detecting the desired final state events. A cut on the polar angle of the omega ensures a stronger sample of $\omega\omega$ candidate events.

The second reason pertains to forward peaking. The events of interest to E835 for charmonium study are events resulting from total $\bar{p}p$ annihilation (class 3 as described in chapter 1.3.1). Part of the background, however, to $\omega\omega$ comes from reactions where all the valence quarks from the proton and antiproton do not annihilate (classes 0, 1, and 2 as described in section 1.3.1). See the quark flow diagram (figure 4.6) for an example of class 2 $\bar{p}p$ partial annihilation to $\omega\omega$. Spectator quarks in these reactions will tend to have larger longitudinal momentum components and will thus “pull” the forward ω to smaller polar angles. This contributes to the noticeable forward peaking in the $\cos\theta^*$ spectrum. Figure 4.7 shows the $\cos\theta^*$ distribution for a sample of $\omega\omega$ candidate events. Note the acceptance drop to zero close to $|\cos\theta^*| = 0.7$ which is where the backward ω misses the upstream boundary of the calorimeter. Based on this plot, the cut $|\cos\theta^*| < 0.28$ was chosen to maximize the influence of $L = 0$ relative $\bar{p}p$ angular momentum (the desired class 3 events).

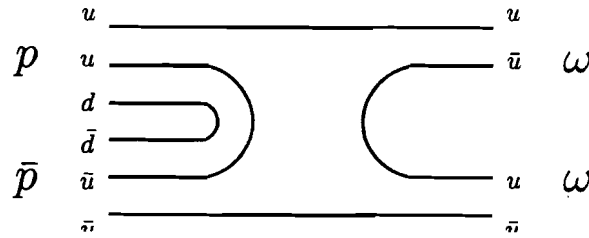


Figure 4.6: $\bar{p}p$ to $\omega\omega$ with Two Spectator Quarks (Class 2)

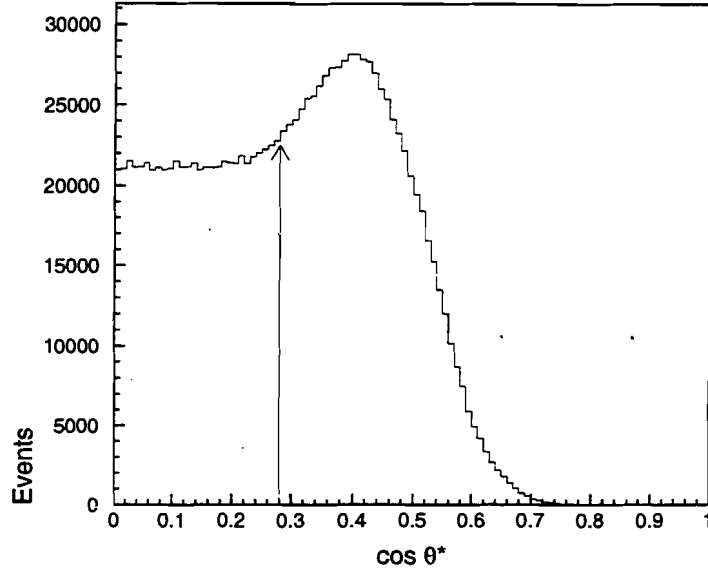


Figure 4.7: $|\cos \theta^*|$ Distribution for $\omega\omega$ Candidate Events in the η_c Region

4.2 Angular Distribution of $\omega\omega$

The decay of $\bar{p}p$ to $\omega\omega$ can proceed through many possible J^{PC} s. The nonresonant formation of $\omega\omega$ from $\bar{p}p$ annihilations could potentially overshadow the signal from the resonant production via $\bar{c}c$ bound states. In anticipation of this, the angular distribution for the process $\bar{p}p \rightarrow \omega\omega \rightarrow 2\pi^0 2\gamma \rightarrow 6\gamma$ was calculated to either aid in removing the $\omega\omega$ events whose J^{PC} do not match that of the charmonium state of interest, or at a minimum to allow a cut on the relevant kinematical parameters to enhance the $\omega\omega$ signal with the correct J^{PC} as compared to the other $\omega\omega$ events. Note that not all $\omega\omega$ with the J^{PC} of the charmonium state under study are necessarily resonant.

4.2.1 Possible $\omega\omega$ Quantum Numbers

The spin, parity, and charge conjugation quantum numbers for an ω are $J^{PC} = 1^{--}$, i.e. the ω is a vector particle. Two vector particles can form many possible sets of J^{PC} quantum numbers. Consider the following definitions for a system of two ω particles, ω_1, ω_2 :

$$\begin{aligned}
 \vec{S}_{\omega_{1,2}} &\equiv \text{Spin vector of } \omega_{1,2} \\
 \vec{L}' &\equiv \text{Relative angular momentum of the two } \omega\text{'s} \\
 \vec{S}_{\omega\omega} &\equiv \text{Total system spin } (\vec{S}_{\omega_1} + \vec{S}_{\omega_2}) \\
 \vec{J}_{\omega\omega} &\equiv \text{Total angular momentum } (\vec{L}' + \vec{S}_{\omega\omega}) \\
 P_{1,2}, C_{1,2} &\equiv \text{Parity, Charge conjugation quantum numbers of } \omega_{1,2} \\
 P, C &\equiv P = P_1 P_2 (-1)^{L'}, C = C_1 C_2
 \end{aligned}$$

Clearly, $C = +1$, $P = (-1)^{L'}$, and $|\vec{S}_{\omega\omega}| = 0, 1, 2$ since $|\vec{S}_{\omega_{1,2}}| = 1$. $|\vec{L}'|$ is an integer greater than or equal to zero. Since the two particles in the state are identical bosons, the wave function must be symmetric under the interchange of the two particles. The wave function, $\Psi(\omega\omega)$, is proportional to the spatial and total spin functional descriptions of the $\omega\omega$ system,

$$\Psi \propto \chi(\vec{S}_{\omega\omega}) \times Y(P) \quad (4.3)$$

so that if the total spin creates a symmetric χ (in this case if $|\vec{S}_{\omega\omega}| = \text{even}$) then the spatial part, Y , must be symmetric (i.e. $P = +1$ so $|\vec{L}'| = \text{even}$) or vice versa ($|\vec{S}_{\omega\omega}| = \text{odd} \Rightarrow P = -1 \Rightarrow |\vec{L}'| = \text{odd}$). Table 4.2 shows the possible J^{PC} constructions for a two ω system. The table only has up to $|\vec{L}'| = 3$ to illustrate that

$ \vec{S}_{\omega\omega} $	$ \vec{L}' $	J^{PC}
0	0	0^{++}
0	2	2^{++}
1	1	0^{-+} 1^{-+} 2^{-+}
1	3	2^{-+} 3^{-+} 4^{-+}
2	0	2^{++}
2	2	0^{++} 1^{++} 2^{++} 3^{++} 4^{++}

Table 4.2: Spin, Relative Angular Momentum (up to $|\vec{L}'| = 3$), and J^{PC} for $\omega\omega$

the possible $\omega\omega$ J^{PC} s are *even* $^{++}$, *even* $^{-+}$, and *odd* $^{-+}$. Note that, contrary to much conventional wisdom, two identical massive vector particles can in fact be in a spin one state (1^{-+} which is an exotic J^{PC} not produced by $\bar{p}p$ annihilation and 1^{++}). It will be shown below that this is not restricted by quantum number conservation or Bose statistics. It seems, rather, to be an inappropriate and unintended generalization of Yang's theorem [54] which states that two identical massless vector bosons (e.g. photons) cannot be in a spin 1 state. This is directly traceable to the lack of a longitudinal polarization for the massless vector particles. Massive identical vector bosons can be in a spin one state when one of them is longitudinally polarized.

A similar exercise as was done above for $\omega\omega$ can be done for the $\bar{p}p$ system. Since the proton and antiproton are not identical particles, no statistics need be obeyed. Also, by definition, a fermion-antifermion pair has relative opposite parity and so the relative angular momentum determines the parity with the equation, $P = (-1)^{L+1}$. The charge conjugation is determined from the spin and relative angular momentum by $C = (-1)^{L+S}$ [55, page 118]. With this knowledge it can be easily discovered that $\bar{p}p$ annihilation can exist in the following J^{PC} s: *even/odd* $^{++}$, *even* $^{-+}$, *odd* $^{+-}$, and *even/odd* $^{--}$ except 0^{--} . Table 4.3 shows which $\bar{p}p$ states create $\omega\omega$ and what the spin and relative angular momentum of each pair must be. Blank entries imply

$ \vec{S}_{\bar{p}p} $	$ \vec{L} (\bar{p}_L p)$	$J_{\bar{p}p}^{PC}$	$ \vec{S}_{\omega\omega} $	$ \vec{L}' $
0	0	0^{-+}	1	1
1	1	0^{++}	0 2	0 2
1 1	0 2	1^{--}		
0	1	1^{+-}		
1	1	1^{++}	2	2
1	2	2^{--}		
0	2	2^{-+}	1 1	1 3
1 1	1 3	2^{++}	0 2 2 2	2 0 2 4
1 1	2 2	3^{--}		
0	3	3^{+-}		
1	3	3^{++}	2 2	2 4

Table 4.3: How $\bar{p}p$ with Specified Quantum Numbers (up to $|\vec{L}| = 3$) Produces $\omega\omega$

that $\omega\omega$ is not accessible via that J^{PC} .

Notice that table 4.3 is only generated up to $\bar{p}p$ in a relative F-wave ($|\vec{L}| = 3$). Although there has been no successful theoretical model developed of $\bar{p}p$ total annihilation up to the writing of this thesis, it is reasonable to assume that increasing $\bar{p}p$ relative angular momentum (thus increasing the impact parameter) would result in a significant decrease in total annihilation production cross sections [see section 5.5 for a more detailed explanation]. For the low $|\cos\theta^*|$ cut made on this data, $L = 0$ $\bar{p}p$ annihilation can be expected to dominate. This is a very different situation

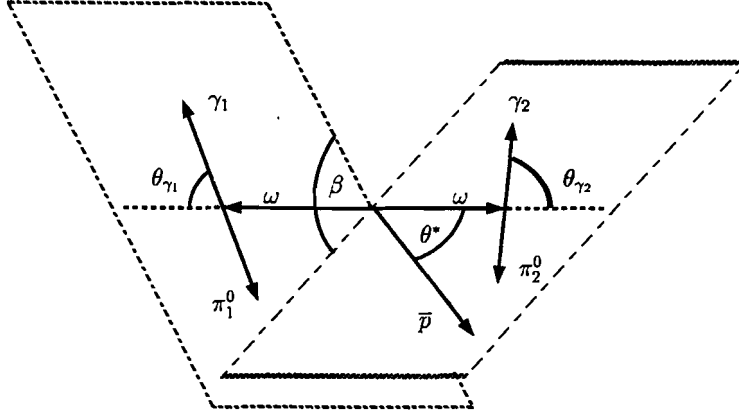


Figure 4.8: Angles Describing the $\omega\omega$ Production and Decay

than, for example, creation of $\omega\omega$ from a single $\bar{q}q$ annihilation where contributions from higher angular momenta can be large. This effect is noticed in the E835 $\pi^0\pi^0$ analyses [56, 57] where $|\vec{L}|$ contribution falls off greatly after 3. For this reason, calculations in following sections are done only for $\bar{p}p$ up to relative F-wave.

4.2.2 Helicity Formulation

To attempt to separate $\omega\omega$ events based on J^{PC} , the angular dependence of the differential cross section, $\frac{d\sigma}{d\Omega}$, was calculated. The helicity formalism of Jacob and Wick [58] was used. Using the notation shown in the diagram on page 94, figure 4.8 shows the relevant angles in the decay chain.

The decays of the pions are not shown since they decay uniformly in azimuth and cosine of the polar angles and thus contribute only a constant to the distribution.

The azimuthal angle of the ω is also necessarily uniform since the $\bar{p}p$ collision is head on along the \hat{z} -axis of the detector (the beam direction) and thus it also contributes only a constant to the angular cross section. The angles describing a

particle in figure 4.8 are defined in the frame of rest of the parent particle, with the parent's direction in the grandmother's rest frame defining the polar axis in the mother's rest frame.

The figure indicates there are five kinematically relevant angles needed to define the reaction. In fact, there are only four as the decay planes of the two $\pi^0\gamma$ pairs, and so ϕ_a and ϕ_c , are correlated. This is shown in Appendix C. The angle between the $\pi^0\gamma$ decay planes is denoted β . The helicity, λ , of a particle is defined as the projection of its spin vector, \vec{S} , along its momentum vector, \vec{p} ,

$$\lambda = \frac{\vec{S} \cdot \vec{p}}{|\vec{p}|} \quad (4.4)$$

For vector particles like the ω , spin one means there are three possible helicities, $\lambda_\omega = 0, \pm 1$ and whereas the photon is a vector particle, its lack of mass prevents it from obtaining helicity 0. That is, the photon must be transverse so that $\lambda_\gamma = \pm 1$ only. The spin 0 pion and spin $\frac{1}{2}$ proton/antiproton have helicities $\lambda_{\pi^0} = 0$ and $\lambda_{p,\bar{p}} = \pm \frac{1}{2}$ respectively. In Appendix C, the helicities are used to calculate the angular dependence, based on the four relevant parameters listed above, of the differential cross section. The result is, where $d\Omega$ includes differentials from only the four necessary angles, J is the total initial angular momentum, and η is the total parity quantum number,

$$\begin{aligned} \left(\frac{d\sigma}{d\Omega} \right)_J &\propto \quad (4.5) \\ &2|a_{11}|^2[|f_{\frac{1}{2},\frac{1}{2}}|^2(d_{0,0}^J(\theta^*))^2 + |f_{\frac{1}{2},-\frac{1}{2}}|^2(d_{1,0}^J(\theta^*))^2(1 + \frac{1}{2}P_2(\cos \theta_{\gamma_1}))] \\ &+ |a_{00}|^2[|f_{\frac{1}{2},\frac{1}{2}}|^2(d_{0,0}^J(\theta^*))^2 + |f_{\frac{1}{2},-\frac{1}{2}}|^2(d_{1,0}^J(\theta^*))^2(1 - P_2(\cos \theta_{\gamma_1}))] \\ &+ 2|a_{10}|^2[2|f_{\frac{1}{2},\frac{1}{2}}|^2(d_{1,0}^J(\theta^*))^2 + \end{aligned}$$

$$\begin{aligned}
& |f_{\frac{1}{2},-\frac{1}{2}}|^2((d_{1,1}^J(\theta^*))^2 + (d_{1,-1}^J(\theta^*))^2)(1 - \frac{1}{4}P_2(\cos \theta_{\gamma_1})) \\
& + |a_{1-1}|^2[2|f_{\frac{1}{2},\frac{1}{2}}|^2(d_{2,0}^J(\theta^*))^2 + \\
& |f_{\frac{1}{2},-\frac{1}{2}}|^2((d_{2,1}^J(\theta^*))^2 + (d_{2,-1}^J(\theta^*))^2)(1 + \frac{1}{2}P_2(\cos \theta_{\gamma_1}))] \\
& + \frac{\sqrt{6}}{2} \eta |a_{11}|^2 d_{2,0}^2(\theta_{\gamma_1}) \cos 2\beta [|f_{\frac{1}{2},\frac{1}{2}}|^2(d_{0,0}^J(\theta^*))^2 + |f_{\frac{1}{2},-\frac{1}{2}}|^2(d_{1,0}^J(\theta^*))^2]
\end{aligned}$$

where $a_{\lambda_1\lambda_2}$ are the complex, energy dependent amplitudes for a state with quantum numbers J^{PC} to go to an $\omega\omega$ state with ω helicities λ_1 and λ_2 , $f_{\lambda_p\lambda_{\bar{p}}}$ is the complex, energy dependent amplitude for $\bar{p}p$ with helicities λ_p and $\lambda_{\bar{p}}$ to form a state with quantum numbers J^{PC} , P_2 is the second order Legendre polynomial, and the d-functions, $d_{m,m'}^J(\theta)$, describe rotations of spin J states (see Appendix C). Parity, charge conjugation, and angular momentum conservation put the following restrictions on the amplitudes above:

$$\begin{aligned}
J = 0 & \Rightarrow a_{1,0} = a_{0,0} = 0 \\
J = 1 & \Rightarrow a_{1,-1} = 0 \\
J = odd & \Rightarrow f_{\frac{1}{2},\frac{1}{2}} = a_{1,1} = a_{0,0} = 0 \\
\eta = -1 & \Rightarrow f_{\frac{1}{2},-\frac{1}{2}} = a_{1,-1} = 0 \\
J = even \ \& \ \eta = -1 & \Rightarrow a_{0,0} = 0
\end{aligned}$$

These equations and conditions are not derived in any public forum and thus are fully derived in Appendix C. The method and results, however, are consistent with those published for other processes (see, for example, reference [67]). Note that completeness requires the normalizations

$$2|a_{1,1}|^2 + 4|a_{1,0}|^2 + |a_{0,0}|^2 + 2|a_{1,-1}|^2 = 1 \quad (4.6)$$

$$2|f_{\frac{1}{2},\frac{1}{2}}|^2 + 2|f_{\frac{1}{2},-\frac{1}{2}}|^2 = 1$$

so that, for example, if $f_{\frac{1}{2},\frac{1}{2}} = 0$ then $|f_{\frac{1}{2},-\frac{1}{2}}|^2 = \frac{1}{2}$.

By integrating over three of the angles in equation 4.5, four equations can be derived, each in terms of only one of the relevant angles. These distributions are (note that θ_{γ_1} and θ_{γ_2} will have the same distribution)

$$T(\cos \theta^*) \propto \quad (4.7)$$

$$\begin{aligned} & 4\pi \{ (2|a_{1,1}|^2 + |a_{0,0}|^2) (|f_{\frac{1}{2},\frac{1}{2}}|^2 (d_{0,0}^J(\theta^*))^2 + |f_{\frac{1}{2},-\frac{1}{2}}|^2 (d_{1,0}^J(\theta^*))^2) \\ & + 2|a_{1,0}|^2 (2|f_{\frac{1}{2},\frac{1}{2}}|^2 (d_{1,0}^J(\theta^*))^2 + |f_{\frac{1}{2},-\frac{1}{2}}|^2 ((d_{1,1}^J(\theta^*))^2 + (d_{1,-1}^J(\theta^*))^2) \\ & + |a_{1,-1}|^2 (2|f_{\frac{1}{2},\frac{1}{2}}|^2 (d_{2,0}^J(\theta^*))^2 + |f_{\frac{1}{2},-\frac{1}{2}}|^2 ((d_{2,1}^J(\theta^*))^2 + (d_{2,-1}^J(\theta^*))^2) \} \end{aligned}$$

$$Q(\cos \theta_{\gamma_1}) \propto \frac{\int T(\cos \theta^*) d\theta^*}{2} \{1 + \zeta P_2(\cos \theta_{\gamma_1})\} \quad \text{where} \quad (4.8)$$

$$\begin{aligned} \zeta &= \frac{4\pi}{\int d\theta^* T(\cos \theta^*)} \int d\theta^* \\ & \{ (|a_{1,1}|^2 - |a_{0,0}|^2) (|f_{\frac{1}{2},\frac{1}{2}}|^2 (d_{0,0}^J(\theta^*))^2 + |f_{\frac{1}{2},-\frac{1}{2}}|^2 (d_{1,0}^J(\theta^*))^2) \\ & - |a_{1,0}|^2 (2|f_{\frac{1}{2},\frac{1}{2}}|^2 (d_{1,0}^J(\theta^*))^2 + |f_{\frac{1}{2},-\frac{1}{2}}|^2 ((d_{1,1}^J(\theta^*))^2 + (d_{1,-1}^J(\theta^*))^2) \\ & + |a_{1,-1}|^2 (2|f_{\frac{1}{2},\frac{1}{2}}|^2 (d_{2,0}^J(\theta^*))^2 + |f_{\frac{1}{2},-\frac{1}{2}}|^2 ((d_{2,1}^J(\theta^*))^2 + (d_{2,-1}^J(\theta^*))^2) \} \end{aligned}$$

$$B(\cos 2\beta) \propto \frac{\int T(\cos \theta^*) d\theta^*}{2\pi} \{1 + \alpha \eta \cos 2\beta\} \quad \text{where} \quad (4.9)$$

$$\alpha = \frac{2\pi}{\int d\theta^* T(\cos \theta^*)} \int d\theta^* |a_{1,1}|^2 (|f_{\frac{1}{2},\frac{1}{2}}|^2 (d_{0,0}^J(\theta^*))^2 + |f_{\frac{1}{2},-\frac{1}{2}}|^2 (d_{1,0}^J(\theta^*))^2)$$

Next, these distributions are calculated for $J^{PC} = 0^{-+}, 0^{++}, 1^{++}, 2^{-+}$, and 2^{++} .

$$0^{-+} : \tag{4.10}$$

$$\begin{aligned} T(\cos \theta^*) &= 2\pi \\ Q(\cos \theta_\gamma) &= \frac{3}{2} (0.28) \pi (1 + \cos^2 \theta_\gamma) \\ B(\cos 2\beta) &= 2(0.28) (1 - \frac{1}{4} \cos 2\beta) \end{aligned}$$

$$0^{++} : \tag{4.11}$$

$$\begin{aligned} T(\cos \theta^*) &= 2\pi \\ Q(\cos \theta_\gamma) &= 3 (0.28) \pi (1 - |a_{1,1}|^2) (1 + \left(\frac{3|a_{1,1}|^2 - 1}{1 - |a_{1,1}|^2} \right) \cos^2 \theta_\gamma) \\ B(\cos 2\beta) &= 2(0.28) (1 + \frac{|a_{1,1}|^2}{2} \cos 2\beta) \end{aligned}$$

$$1^{++} : \tag{4.12}$$

$$\begin{aligned} T(\cos \theta^*) &= \frac{\pi}{2} (1 + \cos^2 \theta^*) \\ Q(\cos \theta_\gamma) &= \frac{9}{16} (0.287) \pi (1 - \frac{1}{3} \cos^2 \theta_\gamma) \\ B(\cos 2\beta) &= \frac{1}{2} (0.287) \end{aligned}$$

$$2^{-+} : \tag{4.13}$$

$$T(\cos \theta^*) = 3\pi [(5|a_{1,1}|^2 - 1) \cos^4 \theta^*]$$

$$\begin{aligned}
& + (1 - 4|a_{1,1}|^2) \cos^2 \theta^* + \frac{1}{3} |a_{1,1}|^2 \Big] \\
Q(\cos \theta_\gamma) = & \frac{3}{2} \pi [(0.088 |a_{1,1}|^2 + 0.016) \\
& + (0.13 |a_{1,1}|^2 - 0.0052) \cos^2 \theta_\gamma] \\
B(\cos 2\beta) = & (0.021 + 0.197 |a_{1,1}|^2) - 0.060 |a_{1,1}|^2 \cos 2\beta
\end{aligned}$$

$$2^{++} : \tag{4.14}$$

$$\begin{aligned}
T(\cos \theta^*) = & \pi \left[(5 |f_{\frac{1}{2}, \frac{1}{2}}|^2 - 1) \left(\frac{3}{4} - 5 |a_{1,0}|^2 - \frac{5}{4} |a_{1,-1}|^2 \right) \cos^4 \theta^* \right. \\
& + \frac{3}{2} \left((2 - 14 |a_{1,0}|^2 - 3 |a_{1,-1}|^2) |f_{\frac{1}{2}, \frac{1}{2}}|^2 \right. \\
& \left. \left. - \left(\frac{1}{2} - 8 |a_{1,0}|^2 - 2 |a_{1,-1}|^2 \right) \right) \cos^2 \theta^* \right. \\
& \left. + \frac{1}{4} (1 - 8 |a_{1,0}|^2 - |a_{1,-1}|^2) |f_{\frac{1}{2}, \frac{1}{2}}|^2 + (2 |a_{1,0}|^2 + |a_{1,-1}|^2) \right] \\
Q(\cos \theta_\gamma) = & \frac{3}{2} \pi \left[\left((0.12 |f_{\frac{1}{2}, \frac{1}{2}}|^2 + 0.021 |f_{\frac{1}{2}, -\frac{1}{2}}|^2) (|a_{1,1}|^2 + |a_{0,0}|^2) \right. \right. \\
& + 3 |a_{1,0}|^2 (0.021 |f_{\frac{1}{2}, \frac{1}{2}}|^2 + 0.13 |f_{\frac{1}{2}, -\frac{1}{2}}|^2) \\
& \left. + |a_{1,-1}|^2 (0.266 |f_{\frac{1}{2}, \frac{1}{2}}|^2 + 0.14 |f_{\frac{1}{2}, -\frac{1}{2}}|^2) \right) \\
& + \left((0.12 |f_{\frac{1}{2}, \frac{1}{2}}|^2 + 0.021 |f_{\frac{1}{2}, -\frac{1}{2}}|^2) (|a_{1,1}|^2 - |a_{0,0}|^2) \right. \\
& - |a_{1,0}|^2 (0.021 |f_{\frac{1}{2}, \frac{1}{2}}|^2 + 0.13 |f_{\frac{1}{2}, -\frac{1}{2}}|^2) \\
& \left. \left. + |a_{1,-1}|^2 (0.266 |f_{\frac{1}{2}, \frac{1}{2}}|^2 + 0.14 |f_{\frac{1}{2}, -\frac{1}{2}}|^2) \right) \cos^2 \theta_\gamma \right] \\
B(\cos 2\beta) = & \left((2 |a_{1,1}|^2 + |a_{0,0}|^2) (0.12 |f_{\frac{1}{2}, \frac{1}{2}}|^2 + 0.021 |f_{\frac{1}{2}, -\frac{1}{2}}|^2) \right. \\
& + 4 |a_{1,0}|^2 (0.021 |f_{\frac{1}{2}, \frac{1}{2}}|^2 + 0.13 |f_{\frac{1}{2}, -\frac{1}{2}}|^2) \\
& \left. + 2 |a_{1,-1}|^2 (0.266 |f_{\frac{1}{2}, \frac{1}{2}}|^2 + 0.14 |f_{\frac{1}{2}, -\frac{1}{2}}|^2) \right) \\
& + |a_{1,1}|^2 (0.12 |f_{\frac{1}{2}, \frac{1}{2}}|^2 + 0.021 |f_{\frac{1}{2}, -\frac{1}{2}}|^2) \cos 2\beta
\end{aligned}$$

Angle	No. of Bins	Range
$\cos \theta^*$	7	0.00 - 0.42
$\cos \theta_{\gamma_1}$	5	-1.0 - 1.0
$\cos \theta_{\gamma_2}$	5	-1.0 - 1.0
β	5	0 - π

Table 4.4: Numbers of Bins and Their Ranges for the Angles that Define the Differential Cross Section

All parameters are integrated over their entire range, except for $\cos \theta^*$ where the integral is from -0.28 to 0.28 since that cut was made in the data selection.

Note that interference among nonresonant angular momentum states, as well as interference between nonresonant $\omega\omega$ and resonant $\bar{c}c \rightarrow \omega\omega$ may be visible or even prominent. It may be necessary upon investigation of the distributions T, Q, and B for real $\omega\omega$ events that such terms as

$$\sum_{\substack{\text{final} \\ \text{helicities}}} \left(\frac{1}{2} \sum_{\substack{\text{initial} \\ \text{helicities}}} |A^{2^+} A^{0^+}| \right) \quad (4.15)$$

be studied. See Appendix C for the definition of A^{J^+} .

Before these angular distributions can be utilized, the real $\omega\omega$ events must be separated out from the fakes comprising the background. The data as selected by the procedure described in section 4.1 is gathered into 4-dimensional bins, one for each parameter (angle) that is necessary to describe the differential cross section. Table 4.4 shows, for each parameter, the number and range of bins. There are 750 total bins ($6 \times 5 \times 5 \times 5$). The range of $\cos \theta^*$ extends beyond the final cut. This is necessary in calculating the efficiency of the analysis cuts as is described in section 4.4. In the final event dataset, however, the $0.28 |\cos \theta^*|$ was enforced.

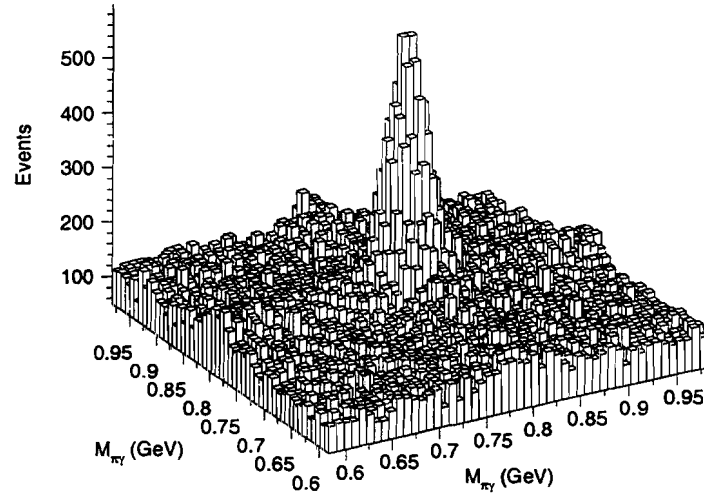


Figure 4.9: Two $\pi^0\gamma$ Pairs' Invariant Masses

4.3 Background Subtraction

After the analysis selection applied in section 4.1, there was still a large number of non- $\omega\omega$ background events in the data sample. Figure 4.9 is a two-dimensional histogram of the invariant masses of the two $\pi^0\gamma$ pairs for all data up to $E_{cm} = 2.985$ GeV. The plot shows three main features: A plane tilted from the low mass corner to the high mass corner (events with no omegas in them but kinematically similar enough to pass the cuts ... mostly $4\pi^0$ feeddown), a berm along each axis's ω mass value (ωX events), and a large peak where both masses are at the ω mass. Some of the peak centered at (m_ω, m_ω) is due to the addition of the two berms, but some is also real $\omega\omega$.

Figure 4.10 shows a fit made to figure 4.9. The fit consists of a plane, two one

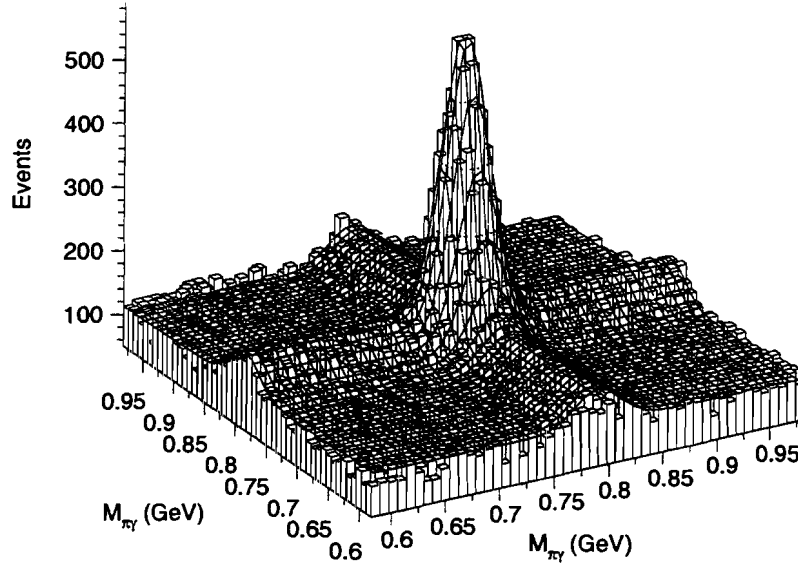


Figure 4.10: Two $\pi^0\gamma$ Pairs' Invariant Masses with a Fit

dimensional Gaussians (the berms), and one two dimensional Gaussian centered at (m_ω, m_ω) . Figure 4.11 shows just the fit, with the background part (the plane and two berms) plotted both with and without the 2 dimensional Gaussian peak.

When the projection along the “ \hat{x} ”-axis is viewed (figure 4.12), where the solid line is the projection of the data and the dashed line is the projection of just the background part of the fit (the two-dimensional Gaussian is not included), it is easy to see that some of the peak does, in fact, contain true $\omega\omega$ events, but that the addition of the berms is not negligible.

The goal eventually is to interpolate the background under the $\omega\omega$ peak so it can be subtracted. Examination of the berms has shown that the height of the berm from the plane does not change through the areas far ($> 6\sigma$ where σ is 22 MeV)

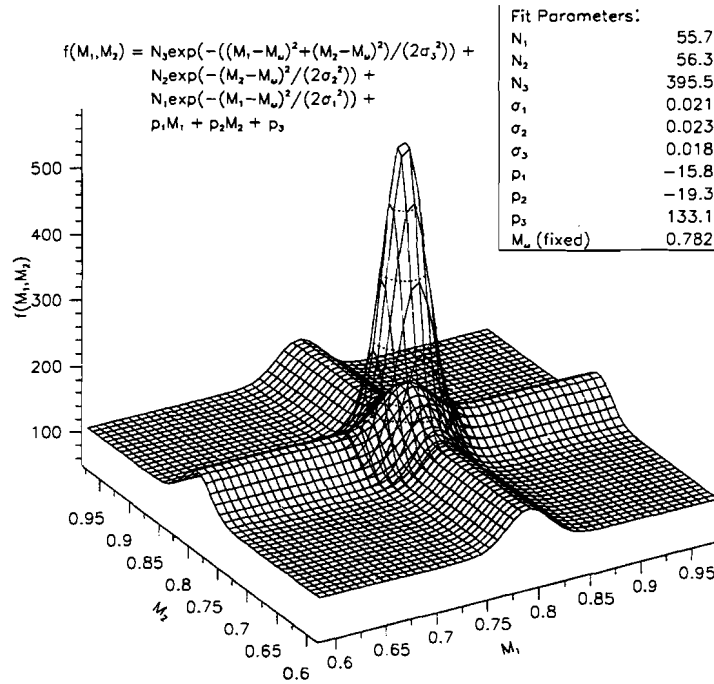


Figure 4.11: Fit with and without the 2-D Gaussian Peak (Real $\omega\omega$ Events)

from the two dimensional peak. It is also the case, as should be expected, that the plane only tilts from the corner with both sets of invariant masses at the lowest value to the corner with both sets of invariant masses at the highest value. Thus, the natural way to view projections of figure 4.9, in order to interpolate, is along 45° bands.

Figure 4.13 is a scatter plot version of figure 4.9 where the four corners have been cut off along 45° lines and $\pm 2\sigma$ bands are drawn about the ω mass on each axis so they include most of the berms.

The figure is then rotated counterclockwise by 45° about (m_ω, m_ω) and divided into 8 bands from 0.582 GeV to 0.982 GeV. Figure 4.14 shows this scenario for figure 4.13 with bands 1 and 8 identified.

It is obvious now that each slice in the new " \hat{x} " direction of this plot contains

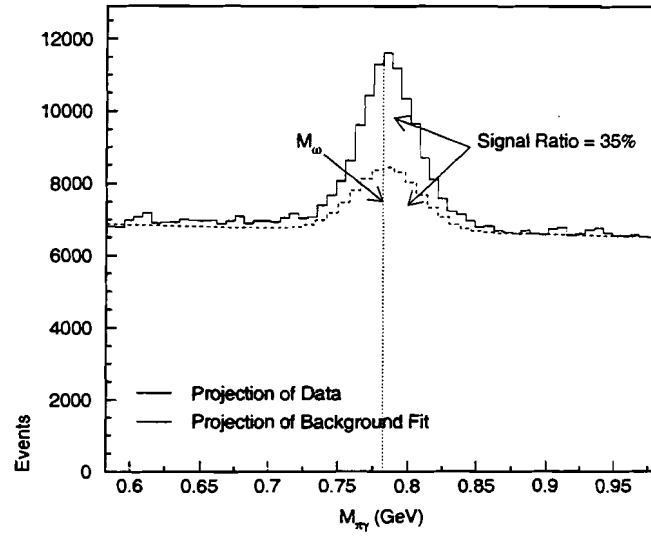


Figure 4.12: Projection of Real Data and Background Part of the Fit

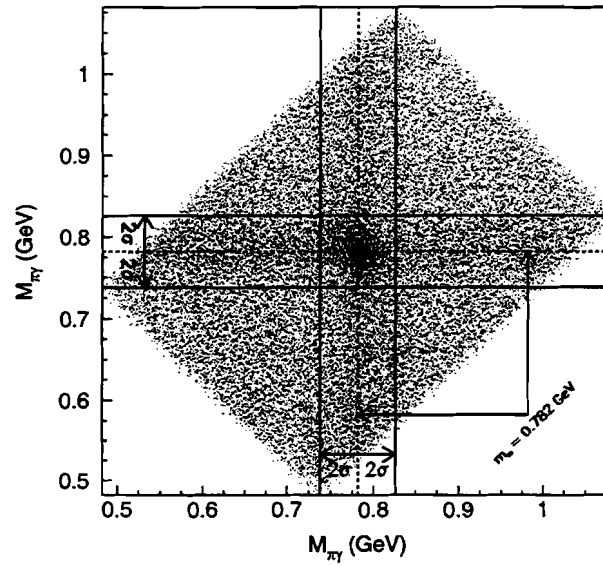


Figure 4.13: $\pi^0\gamma$ Invariant Mass Scatter Plot (Corners Removed and $m_{\omega} \pm 2\sigma$ Bands)

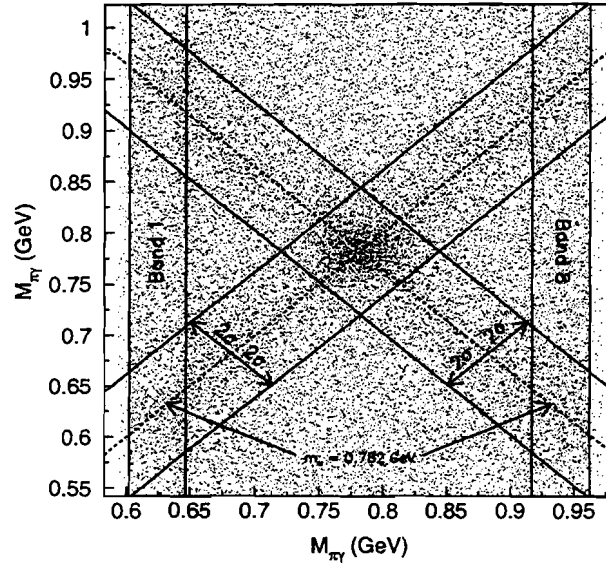


Figure 4.14: Rotation of scatter plot by 45° about (m_{ω}, m_{ω})

the same number of berm events and the same number plane events (within errors). Remember in this plot the plane tilts up along the new “ \hat{y} ”-axis. In fact, a projection along the new “ \hat{x} ”-axis of figure 4.14 is shown as figure 4.15 and is fit to a straight line and a Gaussian. Naively, then, the background could be subtracted by simply counting the number of events in the Gaussian peak. However, later in the analysis it will be necessary to know in which of the 4-d bins described in section 4.2 each event in the peak lies. This information would be lost once the background subtraction as mentioned above took place.

The method actually employed for background subtraction first requires finding the numbers of events, for each run, in each of the 750 bins described in table 4.4 for each of the 8 bands described above (bands 1 and 8 are drawn in figure 4.14). The events in each bin for each band are corrected for total efficiency with the exception of

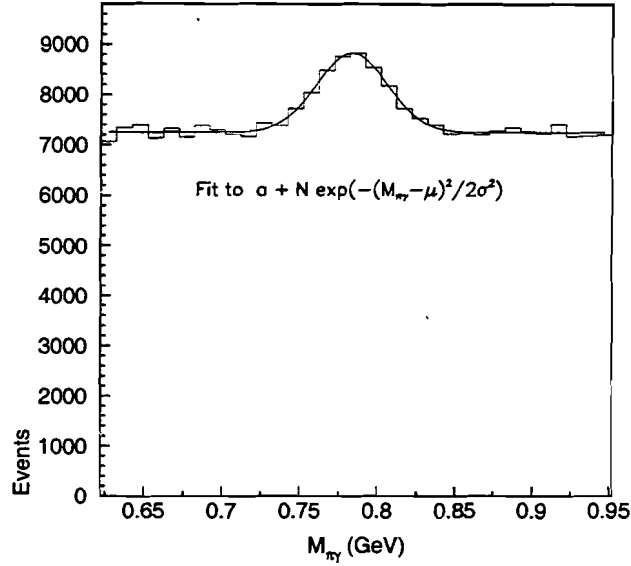


Figure 4.15: Projection of rotated scatter plot on the x-axis Fit to a Line and a Gaussian

the analysis efficiency, ϵ_{anal} (see section 4.4). This is because each event's correction depends on the trigger it came in on (ϵ_{anal} depends only on which of the 4-d bins the event is in) and the trigger information is lost once the background subtraction is performed¹.

Now, it is necessary to show that the shapes of the four angular distributions do not change as a function of band in the non- $\omega\omega$ areas ($> 6\sigma$ from (m_ω, m_ω)). Figures 4.16, 4.17, and 4.18 show the $\cos\theta^*$, $\cos\theta_\gamma$ (the distributions for θ_{γ_1} and θ_{γ_2} are the same), and $\cos 2\beta$ distributions respectively for bands 1, 2, 7, and 8 (i.e., the non- $\omega\omega$ background bands).

Since the shapes of the distributions do not change, the corrected number of

¹When there are N events at the $\omega\omega$ peak and N_b are background, *which* N_b specifically are background cannot be known.

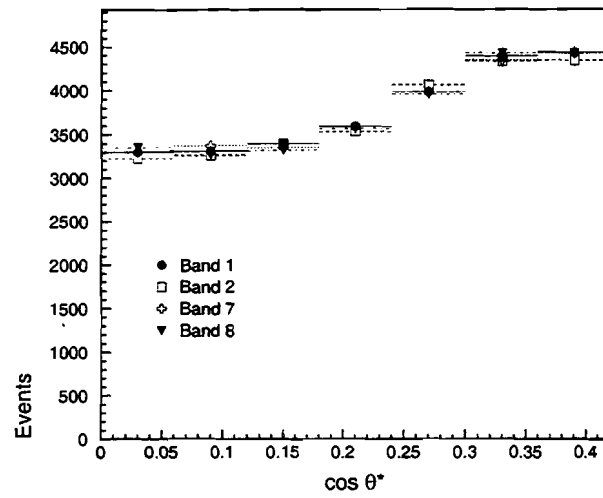


Figure 4.16: $\cos \theta^*$ Distributions for Bands 1, 2, 7, and 8 (Overlaid)

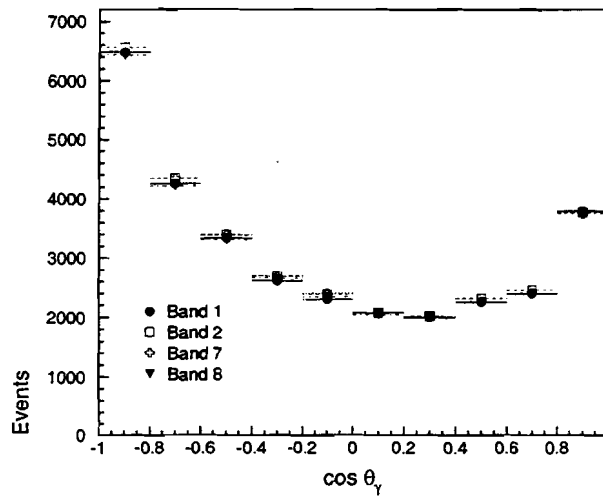


Figure 4.17: $\cos \theta_\gamma$ Distributions for Bands 1, 2, 7, and 8 (Overlaid)

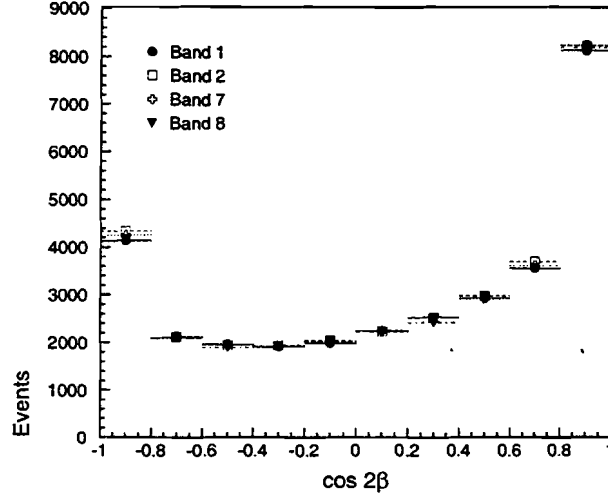


Figure 4.18: $\cos 2\beta$ Distributions for Bands 1, 2, 7, and 8 (Overlaid)

events for a bin due to background (non- $\omega\omega$) in the $\omega\omega$ peak region – defined as a 3σ band about m_ω – can be found by interpolating each bin from the background bins for each band into the correct band in the $\omega\omega$ region. Now, $N_{corr,j}$, the number of real $\omega\omega$ events in bin j corrected for all efficiencies but the analysis efficiency, is known. The next section will describe the efficiencies and how the analysis efficiency is corrected for after this background subtraction has taken place.

4.4 Efficiencies

Before a cross section for real $\omega\omega$ can be obtained, the number of events must be corrected for the efficiency and detector acceptance. For each event, i , the total efficiency, $\epsilon_{i,tot}$, is calculated so that the piece of the cross section, $\Delta\sigma_j$, for each bin,

j (see section 4.2), is given by

$$\Delta\sigma_j = \frac{1}{\int dt\mathcal{L}} \times \sum_{i=1}^{N_{raw,j}} \frac{1}{\epsilon_{i,tot}} \quad (4.16)$$

where $\int dt\mathcal{L}$ is the total integrated luminosity and $N_{raw,j}$ is the number of events in bin j . Note that equation 4.16 will only be used once the data has been background subtracted to remove non- $\omega\omega$ events (see section 4.3) and that the total cross section, σ is

$$\sigma = \alpha \sum_{j=1}^{750} \Delta\sigma_j \quad (4.17)$$

where α is the geometrical acceptance. It is worth noting that for the discrete set of data points (i.e. bins), the differential cross section is related to $\Delta\sigma_j$ as follows:

$$\begin{aligned} \Delta\sigma_j &= \frac{\Delta\sigma_j}{\Delta\Omega} \Delta\Omega \rightarrow \frac{d\sigma_j}{d\Omega} d\Omega && \text{so that} \\ \frac{d\sigma_j}{d\Omega} &= \frac{\Delta\sigma_j}{\Delta\Omega} \\ &= \frac{\Delta\sigma_j}{0.07 \times 0.4 \times 0.4 \times \pi/5} \end{aligned}$$

where $\Delta\Omega$ is the product of the bin widths.

The total efficiency can be broken down into the product of several efficiencies

$$\epsilon_{tot} = \epsilon_{trigger} \times \epsilon_{conv} \times \epsilon_{cont} \times \epsilon_{NDST} \times \epsilon_{analysis} \quad (4.18)$$

These individual efficiencies are described in detail in the next sections.

PRUDE trigger autopass ID	Efficiency	Efficiency	Runs
120 (MINBIAS)	$\epsilon_{auto-MINBIAS}$	0.99999	<3323
		0.999998	≥ 3323
80 (ETOT-NOVETO)	$\epsilon_{auto-ETOT80}$	0.999	≤ 800
		0.998	801 - 2097
		0.990	> 2097
70 (ETOT-LO)	$\epsilon_{auto-ETOT70}$	0.999	≤ 800
		0.998	801 - 2097
		0.990	> 2097
50 (NEUTRAL ETOT)	$\epsilon_{auto-50}$	0.999	

Table 4.5: Efficiencies for Autopass Triggers

4.4.1 Trigger Efficiencies

The trigger efficiency, $\epsilon_{trigger}$, can be further broken down as follows:

$$\begin{aligned} \epsilon_{trigger} = & \epsilon_{auto-MINBIAS} \times \epsilon_{auto-ETOT70} \times \epsilon_{auto-ETOT80} \\ & \times \epsilon_{auto-ETOT50} \times \epsilon_{ETOT-HI} \times \epsilon_{KPRID-51} \end{aligned} \quad (4.19)$$

The efficiencies indexed by the label “auto-” refer to the fraction of data that was not autopassed for specific trigger efficiency studies (see section 3.5). Table 4.5 lists the autopass trigger PRUDE id along with the fraction (efficiency) of data passing the trigger into the dataset written to 8 mm tapes. The $\epsilon_{ETOT-HI}$ are the efficiencies for the total energy trigger as described in section A.3. The values are repeated in table 4.6 for completeness.

The last of the trigger efficiencies is the PRUDE ID 51 prescale. In order to maximize the efficiency of data streaming to 8 mm tapes, the PRUDE ID 51 tagged data events (events where 90% of the available center of mass energy is deposited in the CCAL and no two clusters make an invariant mass greater than 2.0 GeV but

the event is not consistent with $\pi^0\pi^0$, $\pi^0\eta$, or $\eta\eta$) were prescaled by varying amounts depending on energy and run number. Table 4.7 lists the PRUDE ID 51 efficiencies.

4.4.2 Photon Conversions

A photon that converts to an e^+e^- pair in the beam pipe can be rejected by initiating a charged trigger. A study of this effect is presented in reference [45, Appendix C] using a clean sample of $\pi^0\pi^0$ events that came in on the total energy, no neutral veto trigger. The number of events having a pion that could be associated with a charged track were counted. Of the 12056 photons in the data, 198 were associated with charged tracks, and so the probability of an association is, $P_{track} = \frac{198}{12056}$. The efficiency of the charged particle rejection in the neutral veto is given by reference [60] as $\epsilon_{veto} = 0.85 \pm 0.05$. Noting that a photon conversion is indistinguishable from a Dalitz decay ($\pi^0 \rightarrow \gamma e^+e^-$), the probability for a photon conversion is given by

$$P_{conv} = \frac{P_{track}}{\epsilon_{veto}} - \frac{1}{2}P_{Dalitz} \quad (4.20)$$

where $P_{Dalitz} = 0.01213 \pm 0.00033$ is a well measured quantity [59]. The fraction of data, then, that do not lose events to photon conversions is, for a 6 photon final

$\epsilon_{ETOT-HIGH}$	Energy Range (GeV)
99%	< 3.2
98%	3.2 - 3.9
99%	> 3.9

Table 4.6: Total Energy Trigger (ETOT-HI) Efficiencies

Run and Energy (GeV) Range		$\epsilon_{KPRID-51}$
688-1098	2.9-3.25	1.0
688-1098	3.25-4.3	0.1
1098-3334	2.9-3.25	0.25
1098-3334	3.25-4.3	0.5
3335-3340	All Energies	0.1
3346	(Run has only 1 Energy)	0.25

Table 4.7: PRUDE ID 51 Efficiencies

state event such as $\omega\omega$

$$\epsilon_{conv} = (1 - \epsilon_{veto} P_{conv})^6 = (2.082 \pm 0.558) \times 10^{-12} \quad (4.21)$$

4.4.3 NDST Efficiency

As described in Appendix B, there are several cuts introduced into the making of the NDSTs that can cause the loss of good $\omega\omega$ candidate events. Those cuts are:

1. 6 intime or undetermined clusters (see section 2.3.4).
2. At most 10 PRUDE clusters (see section 3.5).
3. Total transverse momentum of all CCAL clusters less than 350 MeV.
4. The total longitudinal momentum of all CCAL clusters must not be further than 15% of the beam momentum away from the beam momentum.

To study the efficiency of these cuts, $\omega\omega$ candidate events from 11 runs were studied. The selections as described in section 4.1 were imposed on the 11 runs for both raw data and the summarized data on the NDSTs. The fraction of $\omega\omega$ candidates surviving the NDST selection as compared to the raw data selection is plotted as

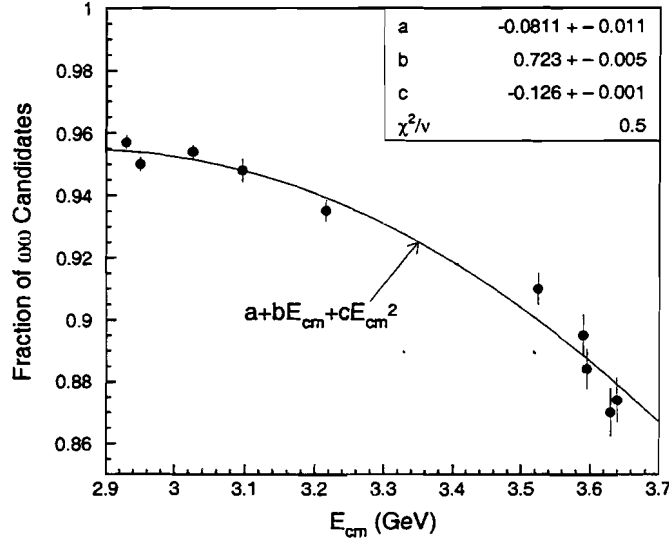


Figure 4.19: NDST Efficiency as a Function of Center of Mass Energy

figure 4.19. The quadratic fit and its errors were used to correct the data. The inefficiency ranges from 4% to 13% as a function of \sqrt{s} . No dependence on instantaneous luminosity was found. The non- $\omega\omega$ data that also passes the cuts in these data sets maintains its numbers relative to the numbers of $\omega\omega$ candidate events before and after creation of the NDSTs, thus the efficiency is not due to a loss in background events only.

4.4.4 Overlapping Event Contamination

When a previous event occurs shortly before a real $\omega\omega$ event, or when noise in the detector coincides with the event, extra clusters in the calorimeter can be recorded. This can cause rejection of a good $\omega\omega$ event. This can happen, for instance, because the extra clusters may be undetermined thus making more than 6 intime or

undetermined clusters in the calorimeter, or the overlapping event might trigger the neutral veto.

To study the effect of overlapping events, random gate data (see section 3.4) was used along with the E835 Monte Carlo. The Monte Carlo generates a random event according to the user's parameters. That is, the desired particle decay chain, particle masses and widths, center of mass energy, angular distribution, etc., are described by the user. The Monte Carlo then generates a random event within the expressed constraints and simulates the reaction's interaction in the detector. The energy crack loss, smearing, pedestal insertion, and calibration constants for a particular run are used to give each cluster an ADC value. These values are then put through the offline clusterizer routines and subject to the proper reaction analysis. This type of Monte Carlo is efficient enough for the type of neutral analysis presented here and is much faster, by about an order of magnitude, than a full lead glass reaction simulation.

Random gate data was a snapshot of what was in the detector at a random moment in time (random in the sense that what happens in the detector does not hold to a pattern ... the snapshot was taken using a 10 kHz clock). A Monte Carlo simulation of $\bar{p}p \rightarrow \omega\omega \rightarrow 2\pi^0 2\gamma \rightarrow 6\gamma$ was developed with the Monte Carlo. First, the analysis cuts described in section 4.1 were performed for data from each run. Then, the Monte Carlo generated events were overlayed with real random gate data and the analysis cuts were applied again. The ratio of the numbers of events surviving for the Monte Carlo with random overlaying events as compared to the regular Monte Carlo was the probability of losing an event, P_{cont} , for that run due to overlapping event contamination.

Figure 4.20 shows the efficiency for detecting an $\omega\omega$ event, $\epsilon_{cont} = 1 - P_{cont}$, where overlap loss is possible. The rate dependence seen in the plot is expected since noise

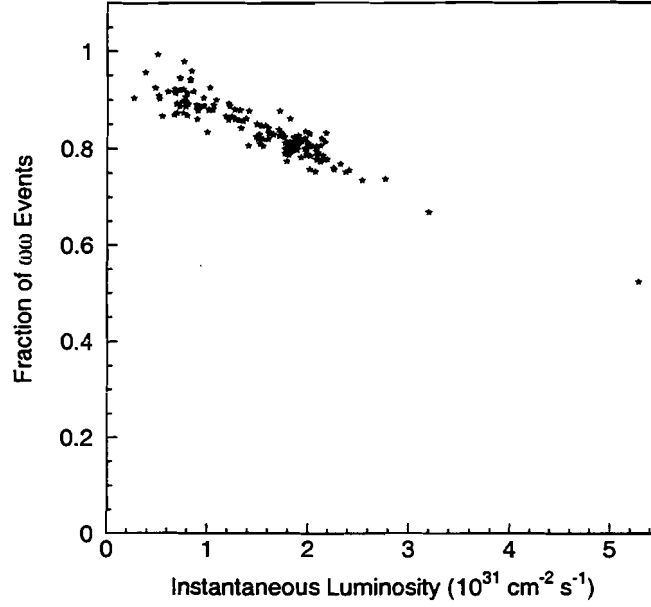


Figure 4.20: Overlapping Event Detection Efficiency vs. Instantaneous Luminosity

as well as proximity in time of energy deposits increases with higher instantaneous luminosity.

4.4.5 Analysis Efficiency

The analysis efficiency, ϵ_{anal} , is a correction for data loss due to analysis cuts, such as the events where γ_1 and γ_2 do not form a pion but $|m_{\gamma_1, \gamma_2} - m_{\pi^0}| < 35 \text{ MeV}$ (see section 4.1.4), or for instance, data lost from low energy photons not being detected by the calorimeter, clusters lost due to hitting one of the four dead CCAL blocks, etc. To correct for these types of circumstances, Monte Carlo simulated $\bar{p}p \rightarrow \omega\omega \rightarrow 2\pi^0 2\gamma \rightarrow 6\gamma$ events were generated so that the number of $\omega\omega$ events it takes to obtain the number observed after the analysis cuts can be determined.

To correctly simulate a reaction in the Monte Carlo, the events should be randomly generated according to the decay chain's angular distribution. This is partly because the efficiency of detecting a particle depends on where it strikes the detector (even which specific block is hit) and partly because certain topologies will be lost more frequently in the detector. For example, for $\omega\omega$ it was shown in section 4.2 that the $\pi^0\gamma$ decay planes are correlated. It is also apparent that the calorimeter has greater acceptance when the $\pi^0\gamma$ lands in a ring (full azimuthal symmetry) rather than in a wedge ($\approx 60^\circ$ coverage in θ) where one particle could fall out the back or front. So, for finding the analysis efficiency, it matters how the relative numbers of events distribute in the physical detector volume.

In the case of the $\omega\omega$ analysis, however, the angular distribution is not known. There are many possible angular momentum states that can be present (see table 4.3) and it is not known in what ratio they will be. When the angular distribution can not be known in advance, the analysis efficiency can be found on a per bin basis where the binned parameters are the relevant angles in the differential cross section. The 4 parameters chosen for binning and the bin range and width are described in table 4.4. The idea is to generate Monte Carlo events in a particular 4-dimensional bin, find the efficiency of detecting those events, then correct the real data on a bin by bin basis.

The major difficulty to overcome in this procedure is bin spillover. Events that are generated in a particular 4-d bin can, through clusterization, event fitting, decay widths, etc., end up after the fit in another bin. Each bin, j , has not only some acceptance, α_j , for how many events generated in it will survive, but other surrounding bins will have some acceptance, $\alpha_{k \rightarrow j}$, for the fraction of events generated in bin k that will spillover to bin j . Then, the number of original events, N_j , in a

bin would be

$$N_j = \sum_k \frac{N_{obs,k}}{\alpha_{k \rightarrow j}} \quad (4.22)$$

where $N_{obs,k}$ is the number of events observed in bin k after the $\omega\omega$ selection is complete and $\alpha_{j \rightarrow j} \equiv \alpha_j$. For this analysis, with 750 bins, this becomes a system of 750 coupled equations and 750 unknowns.

An alternative to solving this equation is to use an iterative procedure to converge on the correct original numbers of events in the bins. The real data for each run was background subtracted bin by bin (see section 4.4) after being corrected for all the other efficiencies. $N_{corr,j}$ then represents the number of real $\omega\omega$ events in a particular 4-d bin (bin j) corrected by all efficiencies with the obvious exception of ϵ_{anal} . The Monte Carlo is run with the proper $\omega\omega$ decay chain input where 10,000 events are generated in each of the 750 bins. The number of events after the analysis cuts, $N_{output1,j}$, is found for each bin. A weight is then calculated for each bin as

$$W_{step2,j} = \frac{N_{corr,j}}{N_{output1,j}} \quad (4.23)$$

This is seen as a first correction to find the original events generated in bin j . Now, the Monte Carlo is run again with 10,000 events/bin, but an event that makes it through the analysis and ends up in bin j is counted as $W_{step2,j}$ events. The total number of events at the end of the second iteration is $N_{output2,j}$. The weight for the next iteration is then,

$$W_{step3,j} = \frac{N_{corr,j} W_{step2,j}}{N_{output2,j}} \quad (4.24)$$

This process was repeated until the values after iteration m , $N_{output[m],j}$, were within 0.1% of $N_{corr,j}$. The original numbers of events that would have been generated in

bin j to give the real data values, $N_{corr,j}$ is then given by

$$N_j = \frac{10000 \times W_{step[m],j} \times N_{corr,j}}{N_{output[m],j}} \quad (4.25)$$

Note that N_j is the number of events in bin j corrected by ϵ_{tot} . The value ϵ_{anal} does not need to be explicitly found in this method (it would be circular to use N_j to find ϵ_{anal} for each bin just to correct $N_{corr,j}$ back to N_j). The typical number of iterations needed to meet the convergence criterion was 4 to 5.

Figures 4.21, 4.22, and 4.23 show the acceptances in two dimensional histograms of the various angular distribution variables for the sample of data from center of mass energies below 2.985 GeV.

The plots show, as expected, a decrease in acceptance along increasing $\cos \theta^*$

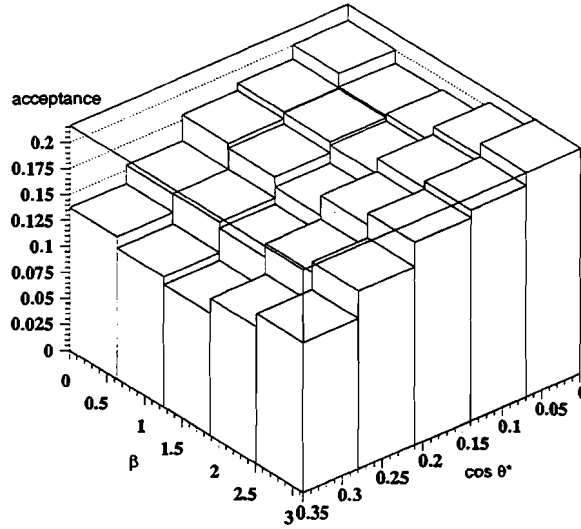


Figure 4.21: Acceptance in Bins of $\cos \theta^*$ and β

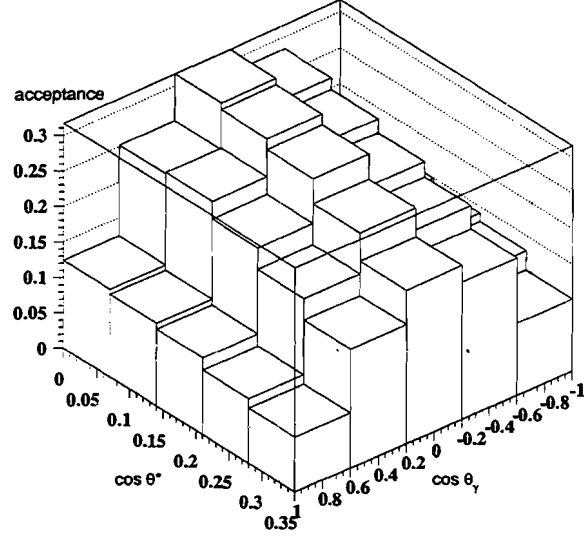


Figure 4.22: Acceptance in Bins of $\cos \theta_\gamma$ and $\cos \theta^*$

(photons from the backward ω begin to miss the upstream end of the calorimeter), an increase of acceptance at $\cos \theta_\gamma = 0$ (when the $\omega \rightarrow \pi^0 \gamma$ decay is symmetric), and a decrease in acceptance near $\beta = 90^\circ$. The average overall acceptance for this data subset is 16%.

Now that the preselection has been performed, i.e. the N_j real $\omega\omega$ events in each 4-d bin for each center of mass energy is known, an attempt can be made to extract specific charmonium resonances.

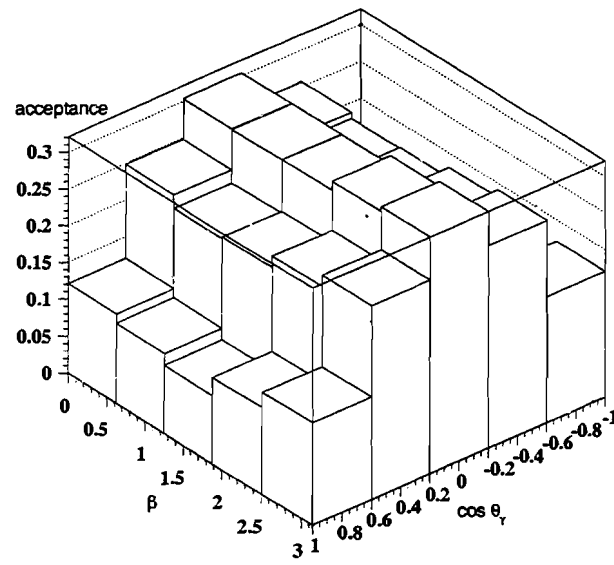


Figure 4.23: Acceptance in Bins of $\cos \theta_\gamma$ and β

Chapter 5

Results and Conclusions

With a selection of real $\omega\omega$ events, the search for charmonium can proceed. The angular distributions can be examined in an attempt to either single out the desired J^{PC} by fitting the distribution as a function of energy, or perhaps to make a cut on the four relevant angles to enhance the desired J^{PC} of the charmonium state and therefore potentially a signal.

In the event that the distributions can not be fit, but an enhancement appears after an angular distribution cut, the width and mass of the charmonium state can still be determined. In the event that no signal appears, the angular distribution must be determined in order to correct for the geometrical acceptance and thus to get an upper bound on the transition.

5.1 Results of the Selection

In the previous chapter, the process for selection of real $\omega\omega$ events was described, as was the correction of the data for all efficiencies. The data that follows represents

10,762 observed $\omega\omega$ events taken with 53.58 pb^{-1} of luminosity, which, after efficiency corrections represents 209,947 $\omega\omega$ events for $\cos\theta^* < 0.28$. In the η_c region there are 6970 observed $\omega\omega$ events for 13.24 pb^{-1} of luminosity representing 189,907 $\omega\omega$ events with $\cos\theta^* < 0.28$ and for the η'_c region there are 2470 observed events for 31.33 pb^{-1} representing 13,433 events for $\cos\theta^* < 0.28$.

Only the geometrical acceptance correction remains to be inserted. Figure 5.1 shows the $\omega\omega$ cross section (efficiency corrected events divided by luminosity) as a function of center of mass energy for these data events over nearly the entire range of energies for the experiment¹ – the second plot is a log plot of the same data.

The next three figures show regions of the same dataset in more detail. Figure 5.2 shows data in the η_c range of energies (2.9 GeV to 3.1 GeV), figure 5.3 shows the data in the triplet P energy range (3.2 GeV to 3.6 GeV), and figure 5.4 shows the data in the expected η'_c region (3.5 GeV to 3.7 GeV). Note that all data is a cut at $|\cos\theta^*| = 0.28$.

There are no apparent resonant structures in any of the plots.

5.2 Hard Cuts on Angular Distribution

Each J^{PC} intermediate $\omega\omega$ state in the reaction has its own unique angular distribution in the four defining angles of the reaction (see section 4.2). From the equations derived in section 4.3, the following properties of various angular momenta and parity states can be deduced:

- The even J states have $\cos\theta_\gamma$ maxima close to ± 1
- The odd J states have $\cos\theta_\gamma$ maximum close to 0

¹Data taken at 4.3 GeV is excluded.

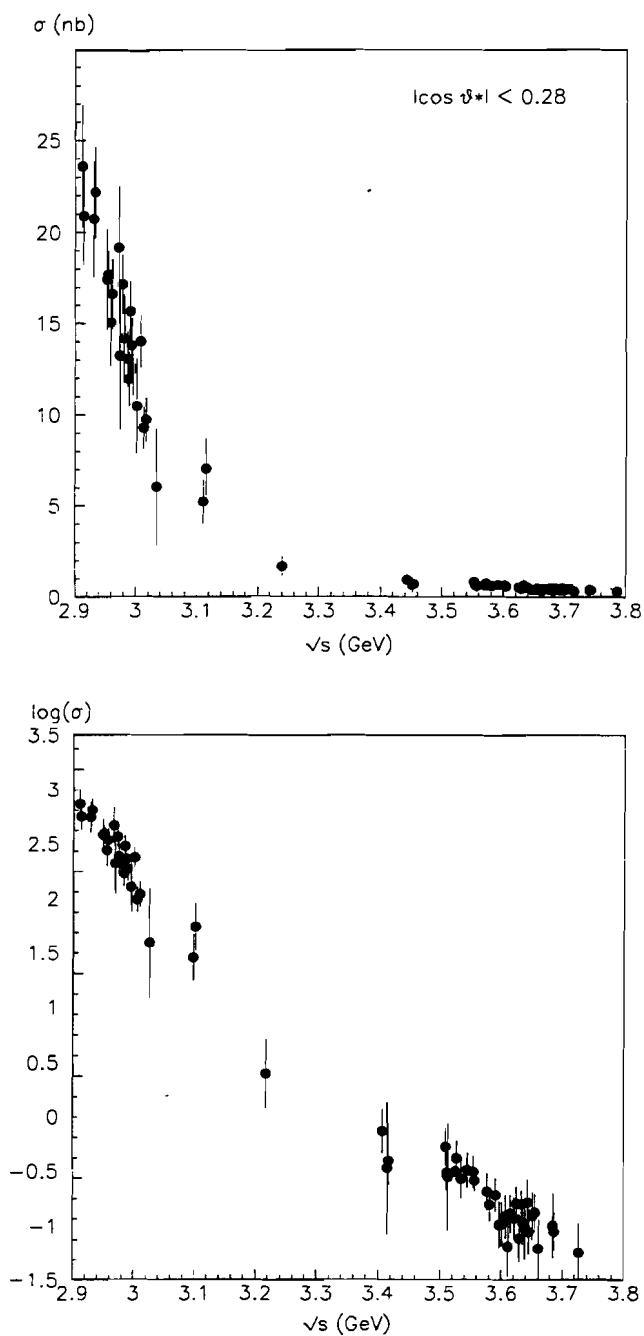


Figure 5.1: $\omega\omega$ Cross Section in the Energy Range 2.91 GeV to 3.8 GeV. Data is in 2 MeV bins. Lower figure is a log plot of the upper figure.

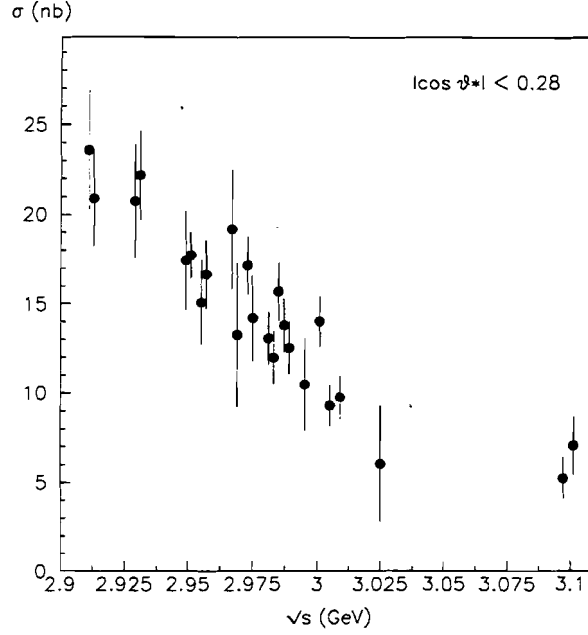


Figure 5.2: $\omega\omega$ Cross Section in the Energy Range 2.91 GeV to 3.1 GeV. Data is in 2 MeV bins.

- Even parity states have $\cos 2\beta$ maxima close to 0 or π (parallel $\pi^0\gamma$ decay planes)
- Odd parity states have $\cos 2\beta$ maximum close to $\frac{\pi}{2}$ (perpendicular $\pi^0\gamma$ decay planes)

Also, as stated in section 4.3, the angles relevant to the angular distribution were organized in bins as follows:

- $\cos \theta^*$ – seven bins of size 0.07 from 0.0 to 0.42 (data was cut at 0.28, i.e. after the fourth bin)
- $\cos \theta_\gamma$ – five bins from -1.0 to 1.0
- $\cos 2\beta$ – five bins from -1.0 to 1.0

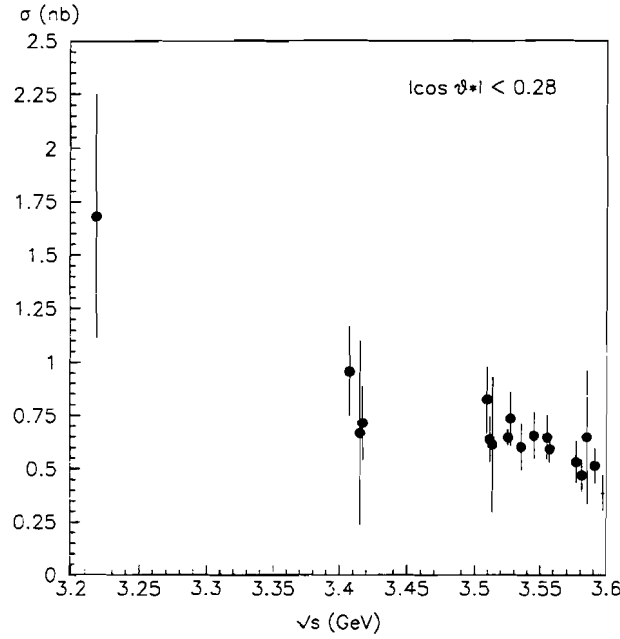


Figure 5.3: $\omega\omega$ Cross Section in the Energy Range 3.2 GeV to 3.6 GeV. Data is in 2 MeV bins.

This information can be used to make hard cuts on these parameters in an attempt to extract a buried charmonium signal. From the shapes of the angular distributions (see next section), and a concern over limited statistics, it was determined that in the η_c and η'_c regions only a cut on β was necessary to attempt this. The requirement that $\beta \in [\frac{\pi}{5}, \frac{4\pi}{5}]$ does not show any structure in the η_c and η'_c regions as shown in figures 5.5 and 5.6. An even more strict cut requiring $\beta \in [\frac{2\pi}{5}, \frac{3\pi}{5}]$ similarly did not show any new structure.

In the χ region, the requirement $\beta \in [0, \frac{2\pi}{5}]$ or $\beta \in [\frac{3\pi}{5}, \pi]$ (for these even parity states) also showed no enhancement of resonant structure (see figure 5.7).

With no visible resonance appearing, it is necessary to examine the angular distributions themselves to attempt to extract additional information.

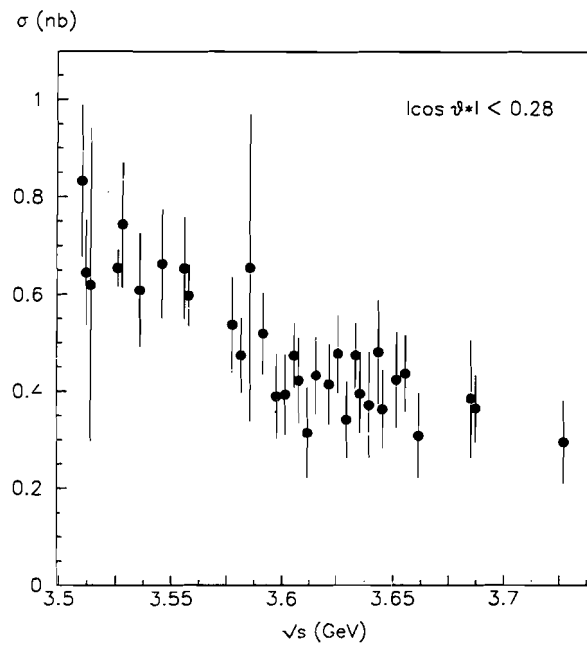


Figure 5.4: $\omega\omega$ Cross Section in the Energy Range 3.5 GeV to 3.6 GeV. Data is in 2 MeV bins.

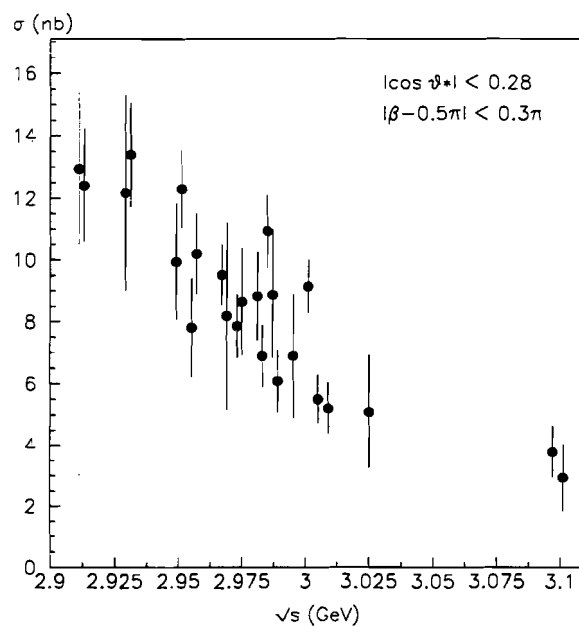


Figure 5.5: Data from Figure 5.2 with $\beta \in [\frac{\pi}{5}, \frac{4\pi}{5}]$. Data is in 2 MeV bins.

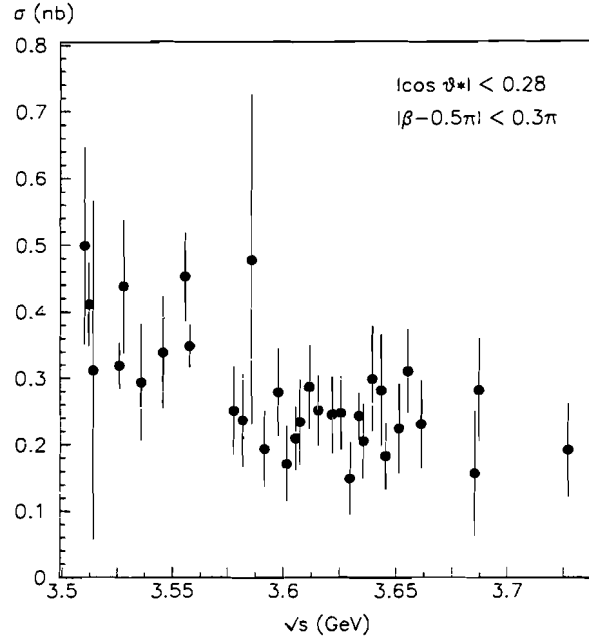


Figure 5.6: Data from Figure 5.4 with $\beta \in [\frac{\pi}{5}, \frac{4\pi}{5}]$. Data is in 2 MeV bins.

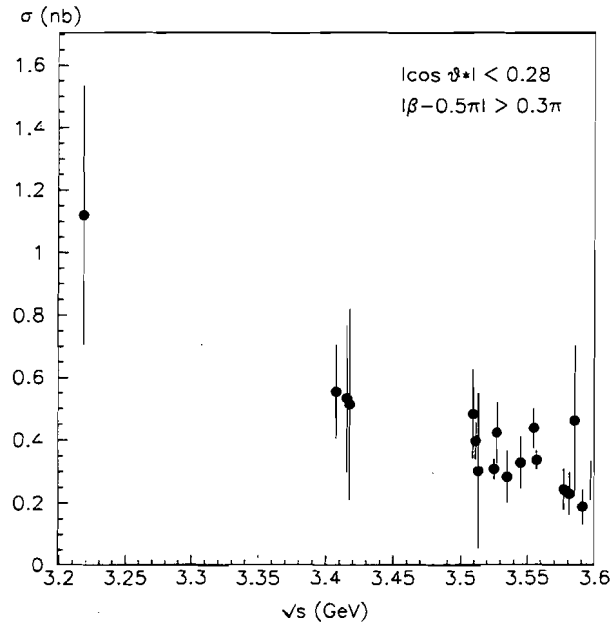


Figure 5.7: Data from Figure 5.3 with $\beta \in [0, \frac{2\pi}{5}]$ or $\beta \in [\frac{3\pi}{5}, \pi]$. Data is in 2 MeV bins.

5.3 Angular Distributions

The next series of plots show the angular distributions for five energy points. Note that the distributions, $\cos \theta_{\gamma_1}$ and $\cos \theta_{\gamma_2}$, for the photons from the ω decays are the same (there is no bias in the choices of ω_1 and ω_2) and so it is only necessary to show one of them. The other plots in each group are the $\cos \theta^*$ and $\cos 2\beta$ distributions.

The first three energy points are representative of data on the η_c peak and the two wings. They are in energy bins 2.950 GeV to 2.952 GeV (figure 5.8), 2.982 GeV to 2.984 GeV (figure 5.9), and 3.096 GeV to 3.098 GeV (figure 5.10).

The last two energy points are data in the χ_0 and η'_c regions, respectively. They are in energy bins 3.316 GeV to 3.418 GeV (figure 5.11), and 3.596 GeV to 3.598 GeV (figure 5.12).

The fits could not be done to a four dimensional function since there were not enough statistics in each 4-d bin to get a sensible result. Within the errors on the plots, no change in the angular distributions is clear across any of the resonances (including the η'_c search region). The drawn fits are done independently on each plot.

Note that the data in plots 5.8 to 5.12 were corrected for total efficiencies (ϵ_{TOT} – see section 4.4), but they were not normalized to the luminosity. It is convenient to first discuss the $\cos \theta_\gamma$ and $\cos 2\beta$ plots.

The distributions for the $\cos \theta_\gamma$ are all consistent with the form $c + d P_2(\cos \theta_\gamma)$ as is dictated for all possible J^{PC} s by equation 4.8. The fit parameters are included in table 5.1. Perhaps the most interesting quantity for this distribution is the ratio, d/c . As seen from equations 4.10 to 4.14, the J^{PC} quantum numbers relate to this value. For instance, even J has positive d/c (e.g. pseudoscalar production has $d/c = 1$) whereas odd J has negative d/c (e.g. pseudovector has $d/c = -1/3$). Figure 5.13

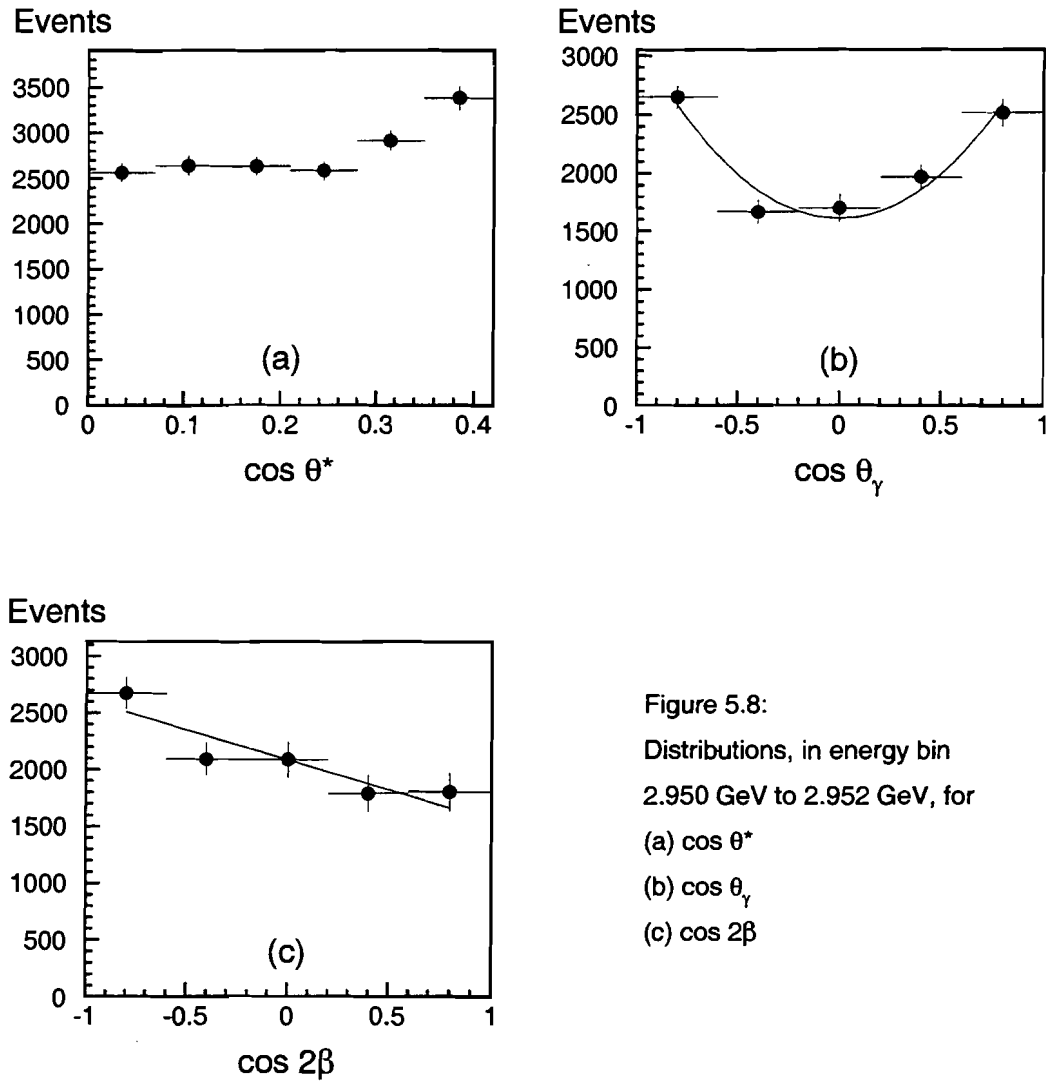


Figure 5.8:
Distributions, in energy bin
2.950 GeV to 2.952 GeV, for
(a) $\cos \theta^*$
(b) $\cos \theta_\gamma$
(c) $\cos 2\beta$

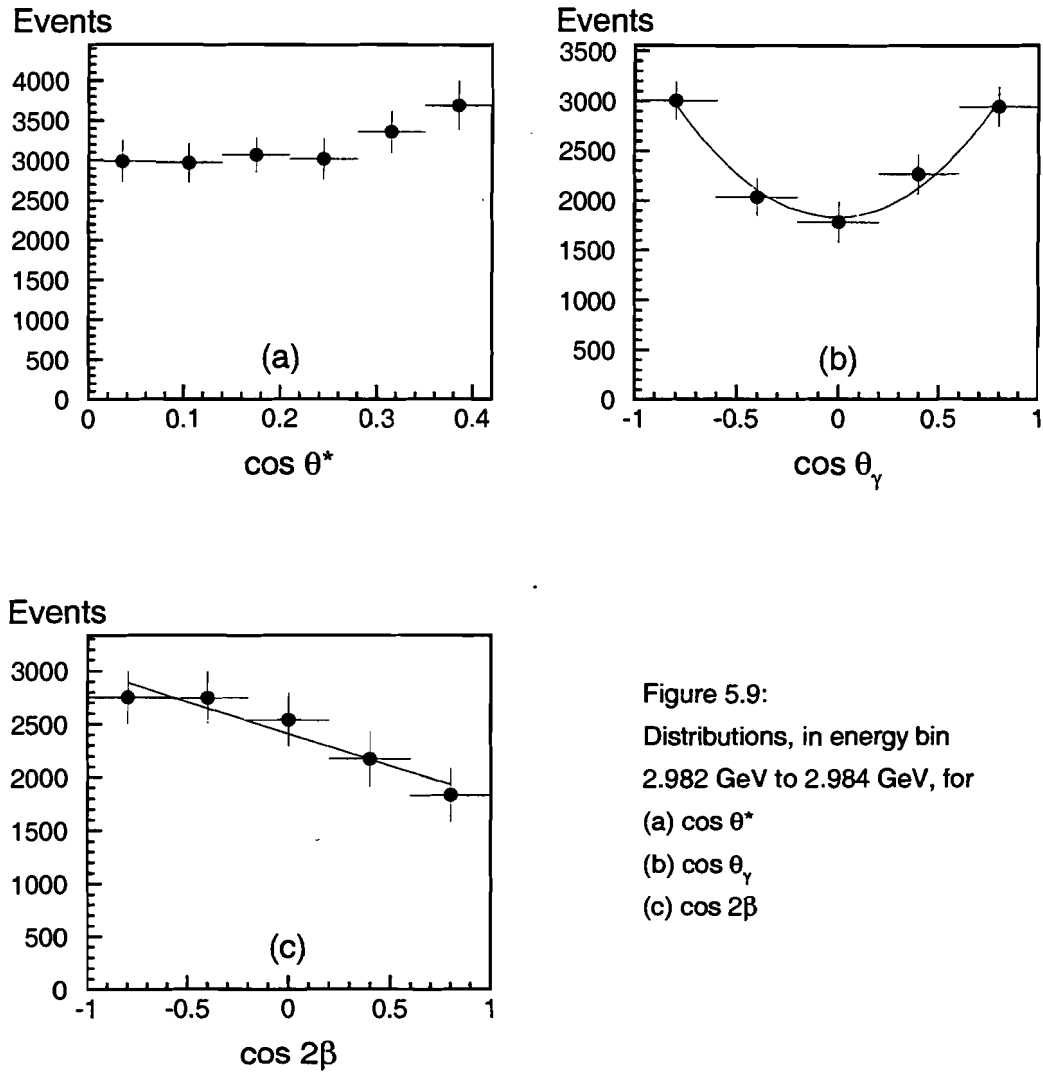


Figure 5.9:
Distributions, in energy bin
2.982 GeV to 2.984 GeV, for
(a) $\cos \theta^*$
(b) $\cos \theta_\gamma$
(c) $\cos 2\beta$

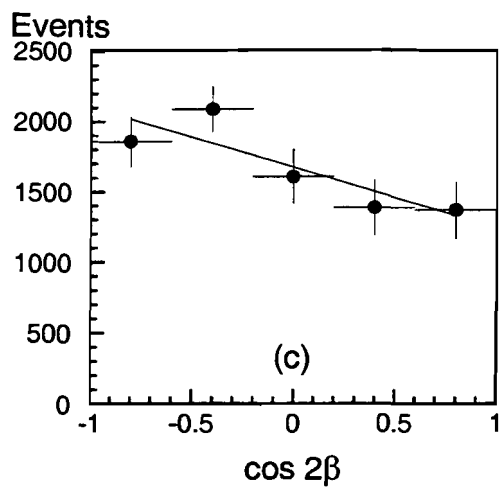
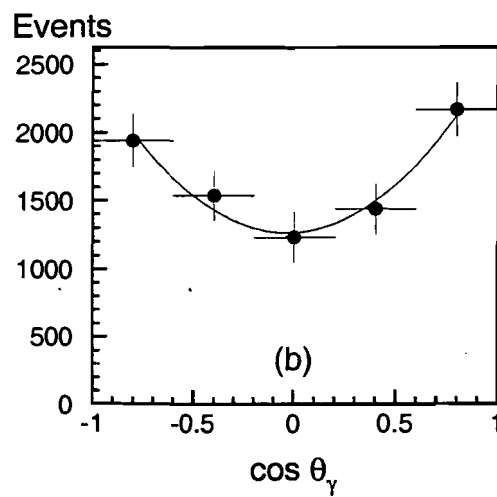
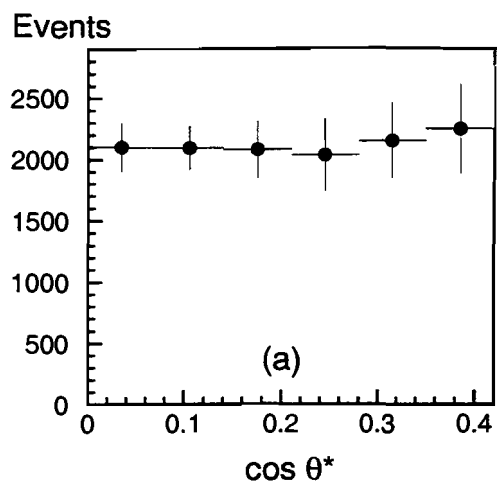


Figure 5.10:
Distributions, in energy bin
3.096 GeV to 3.098 GeV, for
(a) $\cos \theta^*$
(b) $\cos \theta_\gamma$
(c) $\cos 2\beta$

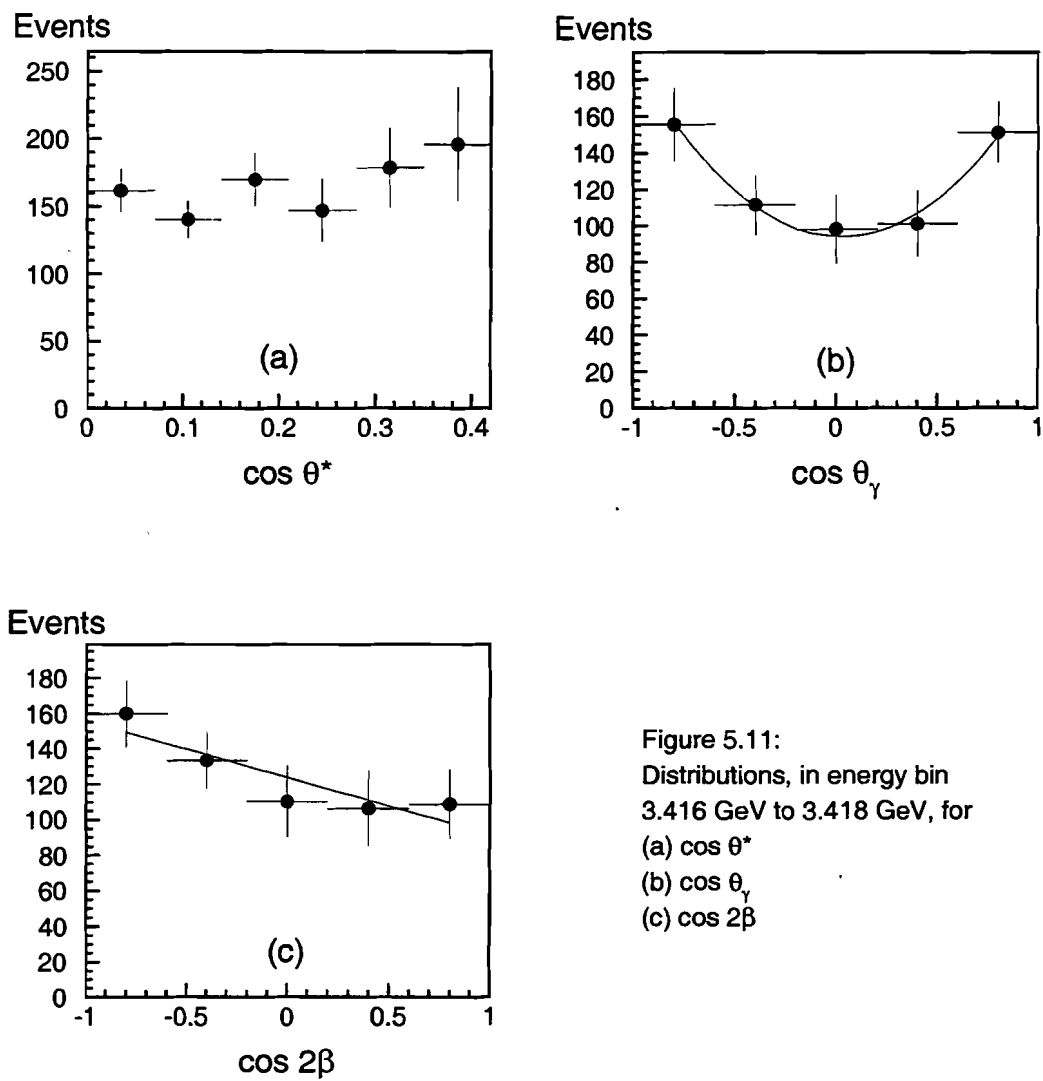


Figure 5.11:
Distributions, in energy bin
3.416 GeV to 3.418 GeV, for
(a) $\cos \theta^*$
(b) $\cos \theta_\gamma$
(c) $\cos 2\beta$

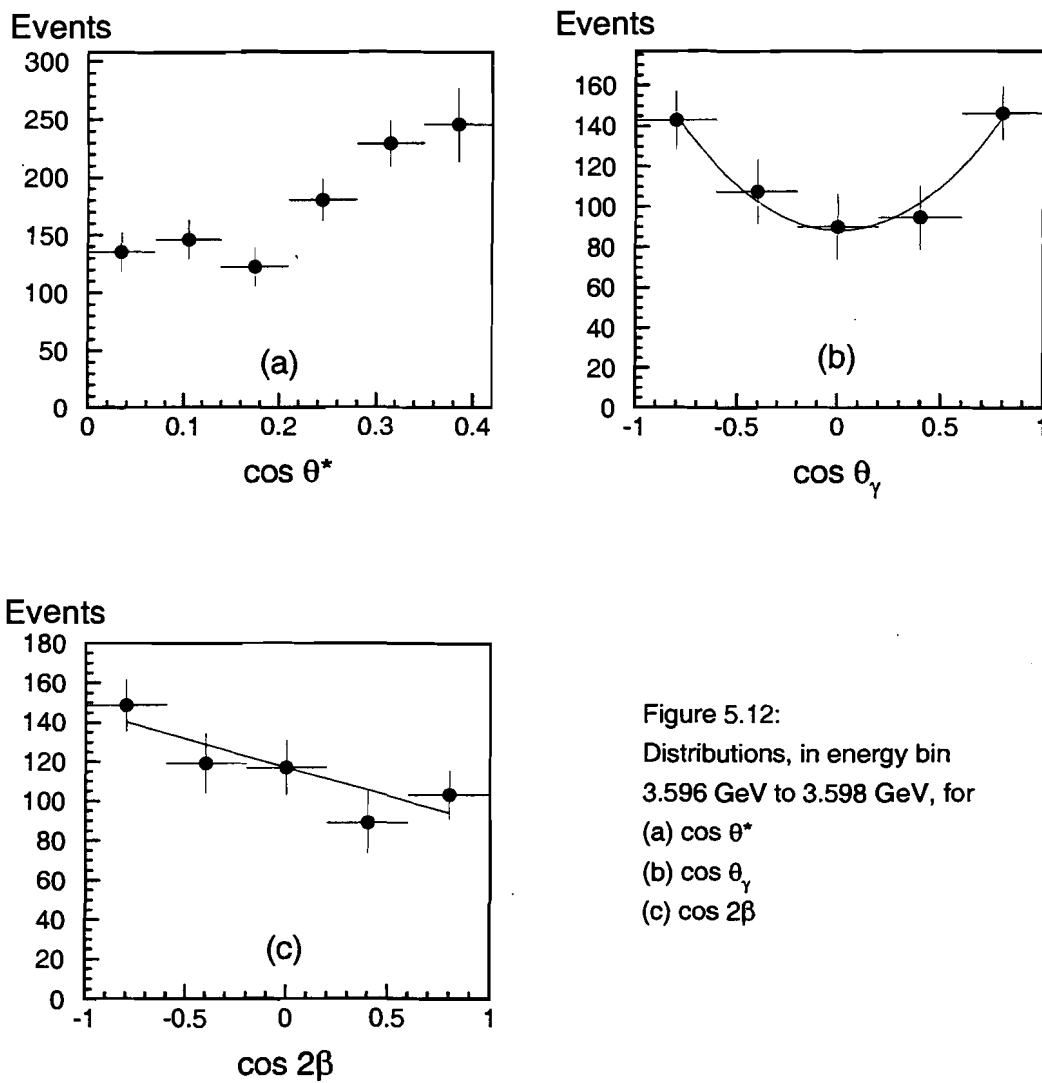


Figure 5.12:
Distributions, in energy bin
3.596 GeV to 3.598 GeV, for
(a) $\cos \theta^*$
(b) $\cos \theta_\gamma$
(c) $\cos 2\beta$

energy (GeV)	$c + d \cos^2 \theta_\gamma$		
	c	d	χ^2/dof
2.950	1609.9 ± 79.5	1519.6 ± 187.0	0.27
2.982	1830.8 ± 141.9	1808.0 ± 337.6	0.39
3.096	1263.1 ± 128.5	1243.0 ± 317.1	0.29
3.416	94.1 ± 12.7	92.4 ± 30.8	0.38
3.596	88.3 ± 11.2	87.7 ± 24.7	0.48

Table 5.1: Fit Values for the θ_γ Angular Distributions at each of the Sample Energies

energy (GeV)	$a + b \cos 2\beta$		
	a	b	χ^2/dof
2.950	2085.7 ± 70.0	-528.3 ± 123.9	1.2
2.982	2408.6 ± 113.3	-602.0 ± 199.6	0.30
3.096	1674.3 ± 84.6	-429.0 ± 151.4	0.41
3.416	123.7 ± 8.5	-31.9 ± 15.1	0.38
3.596	116.9 ± 6.2	-29.0 ± 10.5	0.81

Table 5.2: Fit Values for the β Angular Distributions at each of the Sample Energies

shows this quantity over the E835 range of energies. Notice that d/c is close to 1 (the average value is 0.96), thus showing the dominance of even J .

The $\cos 2\beta$ distributions are fit to $a + b \cos 2\beta$. This form is dictated by equation 4.9. The fit parameters are shown in table 5.2. Again, equations 4.10 to 4.14 suggest that the quantity b/a (i.e. the slope of the $\cos 2\beta$ distribution) contains useful information. States of even J and odd parity have negative slopes (e.g. pseudoscalar has $b/a = -1/4$), even J with even parity have positive slopes, and odd J have flat slopes (i.e. $b/a = 0$). The slope for the data is plotted versus energy in figure 5.14.

Note that the slope is negative indicating the dominance of even J odd parity

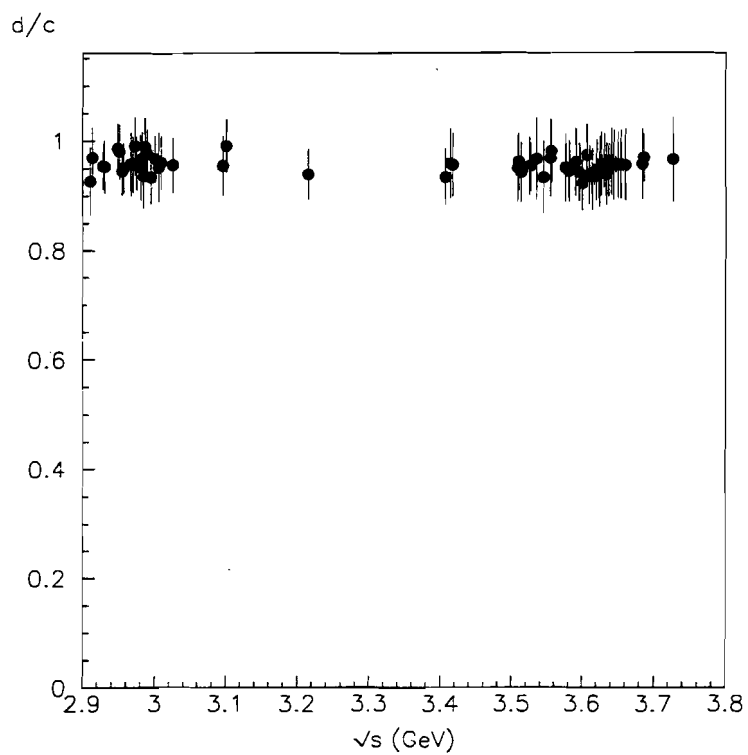


Figure 5.13: d/c vs. Energy

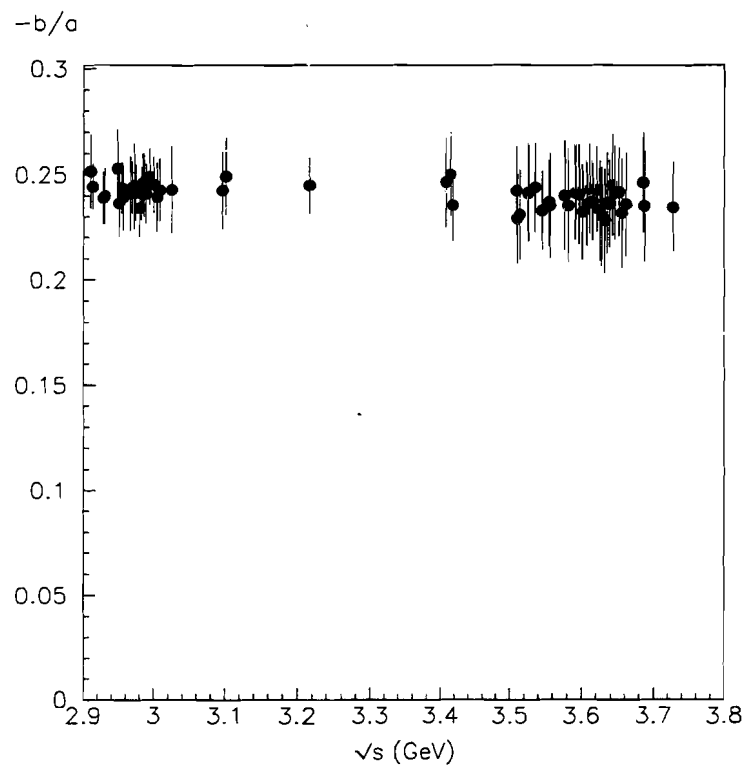


Figure 5.14: $-b/a$ vs. Energy

production. One note of caution at this point – the values seem to indicate that the data is dominantly pseudoscalar production. However, notice (see equation 4.13) that if $|a_{1,1}|^2$ were close to its maximum possible value, 0.5, the $\cos 2\beta$ and $\cos \theta_\gamma$ distributions for 2^{-+} would become identical to those for 0^{-+} . The maximum degree to which 2^{-+} could be present in the data can be estimated, though, as will be discussed later.

In the low $\cos \theta^*$ region where this data was cut ($\cos \theta^* < 0.28$), it is reasonable to speculate that $\bar{p}p$ annihilation is dominated by $L = 0$. This argument was made in section 4.2.1. Referring to table 4.3, initial $\bar{p}p$ relative angular momentum leads to J^{PC} production as follows:

- $L=0 \rightarrow 0^{-+}$
- $L=1 \rightarrow 0^{++}, 1^{++}, 2^{++}$
- $L=2 \rightarrow 2^{-+}$

Thus it is expected that the pseudoscalar production from $L=0$ should dominate with $L=1$ suppressed and $L=2$ even more suppressed. States higher than $L=2$ need not be further considered.

It was shown above that the data is dominated by even J and odd parity which based on previous arguments should indicate predominately $0^{-+} \omega\omega$ production. This is also shown in the $\cos \theta^*$ distributions that are effectively flat up to 0.28. After that value, forward peaking is evident, however, that does not necessarily imply large amounts of additional partial waves exist as the peaking is not extensive. It is not necessary to classify the quantum numbers of the forward peaking, but as it exists it is necessary to estimate the amount.

As the $L=1$ initial state is expected to dominate the $L=2$, it will be considered first. Considering the differences in the $B(\cos 2\beta)$ distributions among the various J^{PC} s, the ratio b/a as defined previously provides the best method for estimating the potential contribution from $L=1$. The ratio b/a is stable within errors at an average value of -0.240 ± 0.007 . The question is then, how much $L=1$ can be present to deviate b/a (i.e. the slope of the $\cos 2\beta$ distribution) from the -0.25 required for pure pseudoscalar production?

The slopes (i.e. b/a) for 0^{++} and 2^{++} are not known as they contain unknown amplitudes (the $|a_{\lambda_{\omega_1}, \lambda_{\omega_2}}|^2$), however, they are positive. The slope for the 1^{++} is flat. The flat slope represents the “worst case scenario” for the $L=1$ (their slopes can not be negative and the more positive they are the less their contribution could be to maintain the slope seen in the data). Therefore, it is legitimate to use the flat slope assumption to get a limit on the amount of all $L=1$ – including the contributions of the scalar and tensor states. For a zero slope and the -0.25 slope of the pseudoscalar to give the average -0.24 slope seen in the data suggests

$$a_{L=0}(0.25) + a_{L=1}(0.0) = 0.24a \quad (5.1)$$

where $a_{L=0}$ is the amount of pseudoscalar data, $a_{L=1}$ is the amount of $L = 1$ data, and $a_{L=0} + a_{L=1} = a$ is the total amount of data. This simple equation then yields that 0^{-+} production is dominant at the level of 96% for $\cos \theta^* < 0.28$.

Next, consider $L = 2$ production. Since the $Q(\cos \theta_\gamma)$ and $B(\cos 2\beta)$ distributions have the potential (when $|a_{1,1}|^2$ nears 0.5) of becoming identical to the pseudoscalar distributions, a different method must be used for estimating its maximum contribution. Consider the form of the $\cos \theta^*$ distribution for 2^{-+}

$$T(\cos \theta^*) \propto \frac{1}{3}|a_{1,1}|^2 + (1 - 4|a_{1,1}|^2) \cos^2 \theta^* + (5|a_{1,1}|^2 - 1) \cos^4 \theta^* \quad (5.2)$$

Figure 5.15 shows this distribution plotted for various values of $|a_{1,1}|^2$ (i.e. for 0.5, 0.4, 0.3, 0.25, 0.2, and 0.0). It is obvious from these plots that the forward peaking seen in the data is not possible from 2^{-+} production unless values of $|a_{1,1}|^2$ are less than 0.25 (where the sign of the $\cos^2 \theta^*$ argument changes), and in fact, in the region we are interested in $-\cos \theta^* < 0.28$ – the peaking is not pronounced for values greater than 0.15. Again, with the “worst case scenario” that $|a_{1,1}|^2 = 0.15$, we derive a slope for the ratio b/a of 0.18. Using an equation similar to 5.1, the amount of 2^{-+} that could be present in the data can be estimated as less than 14%. Any mix of $L=1$ and $L=2$ will not provide for less than 86% 0^{-+} .

Since there are no visible resonances, this information can be used to find an upper limit for the pseudoscalar particles – η_c and η'_c – in the next section. The geometric acceptance is used to take into account the numbers of events that would exist at least partially outside of the detector volume. It is therefore necessary to know the angular distribution of the $\omega\omega$ data so that an accurate estimate of the total events can be established. Since the data is consistent with 86% 0^{-+} production, and the data is cut at $\cos \theta^* < 0.28$ where the distribution is flat (dominated by S-wave production), the geometrical acceptance correction, α , can be fairly estimated as 0.28.

Unfortunately, since all other partial waves are overpowered by 0^{-+} , it is not possible to obtain upper limits for the non-pseudoscalar charmonium states.

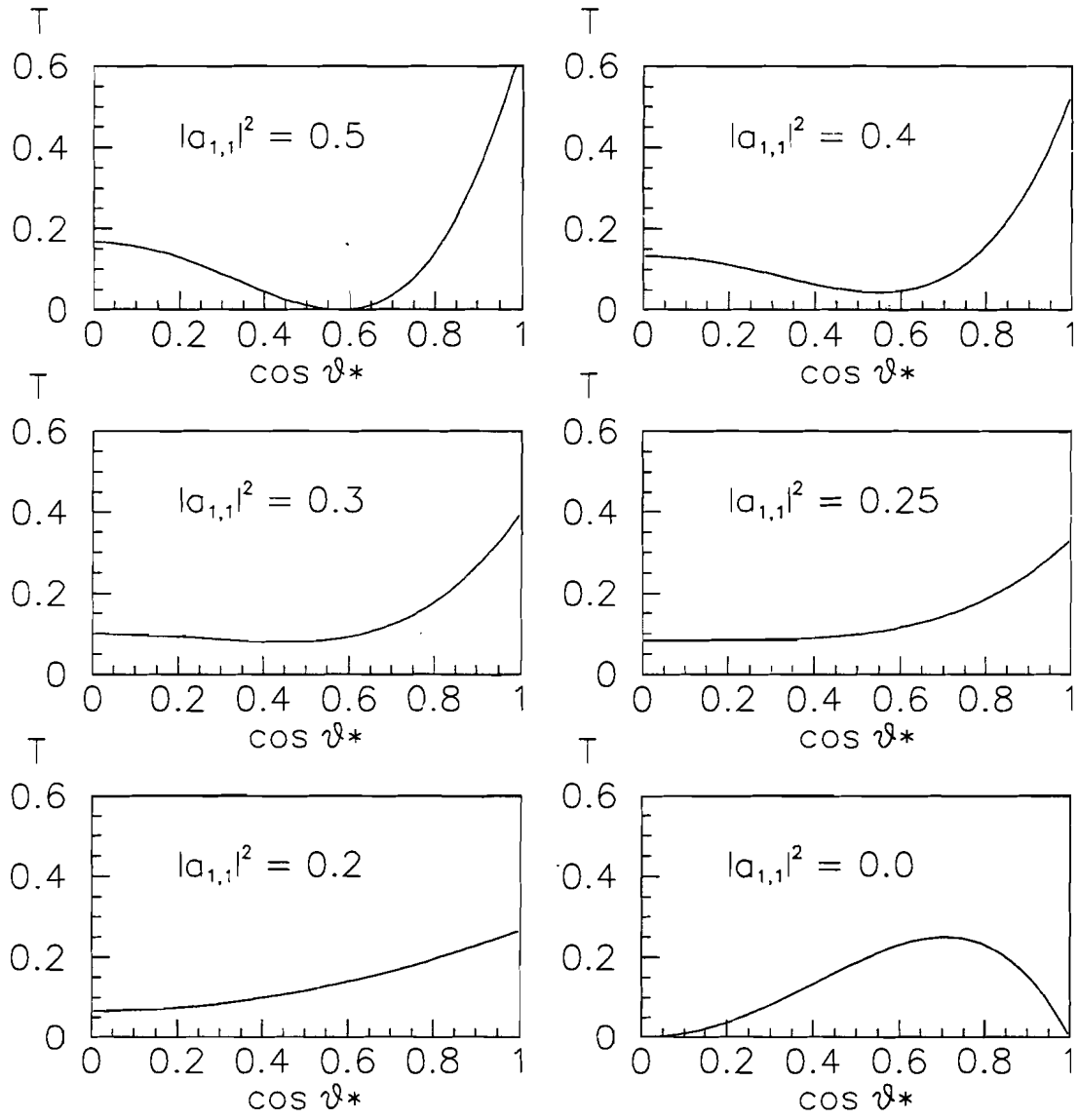


Figure 5.15: $\cos \theta^*$ Distribution for 2^{-+} with Various Values of $|a_{1,1}|^2$

5.4 Upper Limits

With no visible $\omega\omega$ resonant signal in the charmonium regions below the open charm threshold, an upper limit on the branching ratios of the pseudoscalar $\bar{c}c$ states can be calculated.

5.4.1 Technique for Determining Limits

In general, finding parameters for this type of fit is done by minimizing a function representing the difference in the values of the experimentally obtained cross sections, σ_i , for each energy data point i , from the expected value of the cross section, $\sigma_{expected}$. Assuming 0^{-+} dominance and calculating an upper limit for a pseudoscalar resonance on a large nonresonant continuum, interference plays an essential role. Again, this is seen in the current $\pi^0\pi^0$ analyses [56, 57] where large interference effects are evident in the χ_0 resonance. With A representing the non-resonant amplitude, A_R the resonant amplitude, and δ the phase between the two processes, the expected cross section is given by

$$\begin{aligned}\sigma_{expected} &= \left| \left(\frac{M_R}{\sqrt{s}} \right)^{\frac{D}{2}} \left(Ae^{i\delta} - \frac{A_R}{x+i} \right) \right|^2 \\ &= \left(\frac{M_R}{\sqrt{s}} \right)^D \left(A^2 + \frac{A_R^2 - 2AA_R(x \cos \delta - \sin \delta)}{x^2 + 1} \right)\end{aligned}\quad (5.3)$$

where M_R is the mass of the resonance for which the limit is being calculated, the quantity $(M_R/\sqrt{s})^D$ parameterizes the cross section's fall off as center of mass energy increases, and $x = (\sqrt{s} - M_R)/\Gamma_R$ (Γ_R is the width of the resonance). The fact that up to 14% of the data in the $\cos \theta^* < 0.28$ region may be non-pseudoscalar will not effect the upper limit calculations to any significant degree. The non-pseudoscalar

would likely add incoherently and simply absorb into the parameter A , thus not affecting the value of A_R .

Note that the beam does have a shape and so for narrow resonance searches, its distribution should be deconvoluted from the expected cross section. For the η_c search, with energy bins of 2 MeV and a beam width on the order of hundreds of keV, it is not necessary.

A least squares fit is done on the function

$$\chi^2 = \sum_{i=1}^N \left(\frac{\sigma_i - \sigma_{expected}(\sqrt{s_i})}{\Delta_{\sigma_i}} \right)^2 \quad (5.4)$$

using the Cern library routines Migrad and Minos from the Minuit software package. Note that Δ_{σ_i} is the experimental error – statistical and systematic added in quadrature – on σ_i .

5.4.2 Upper Limit of the η_c

For the calculation of the η_c upper limit, M_{η_c} and Γ_{η_c} are taken from the E835 two gamma analysis – $M_{\eta_c} = 2985.9 \pm 2.0$ and $\Gamma_{\eta_c} = 21.6 \pm_{5.7}^{6.9}$ [45]. The 24 data points from 2.9 GeV to 3.1 GeV are used in the fit. In the upper limit, the phase shift can not be determined, so the upper limit is calculated over the entire range of possible values of δ (0 to 2π). As an example of the details of such a calculation, consider $\delta = 180^\circ$ (as of this writing it is unclear if limitations can be put on δ). The result of this fit is plotted in figure 5.16 and the parameter values listed in table 5.3. The results are consistent with no resonant signal.

To determine an upper limit on the branching ratio $B(\bar{p}p \rightarrow \bar{c}c) \times B(\bar{c}c \rightarrow \omega\omega)$ note that A_R is related to the peak cross section via the equation

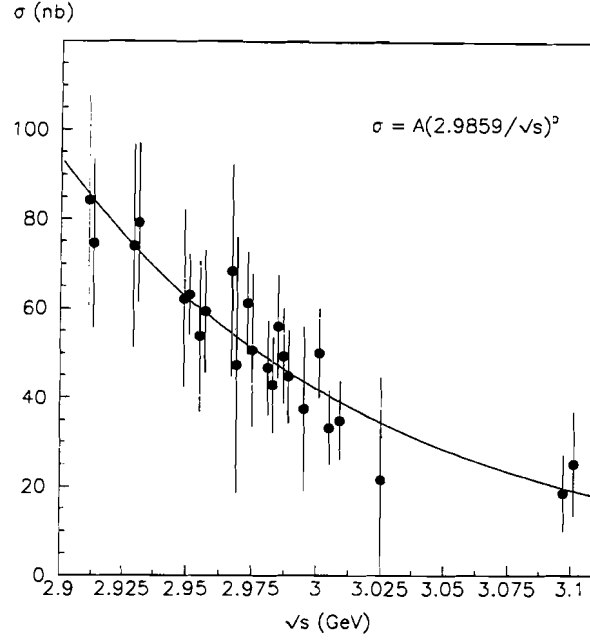


Figure 5.16: Fit to η_c Data with Free Parameters for the Nonresonant Continuum A, D and Resonant Amplitude A_R

$$A_R^2 = \sigma_{peak} = \frac{4\pi}{(M_R^2 - 4m_p^2)} (\hbar c)^2 B_{in} B_{out} \quad (5.5)$$

where the following definitions apply: m_p is the proton mass (all masses in MeV), $B_{in} = B(\bar{p}p \rightarrow \bar{c}c)$ (unknown quantity), and $B_{out} = B(\bar{c}c \rightarrow \omega\omega) \times B(\omega \rightarrow \pi^0\gamma)^2 \times B(\pi^0 \rightarrow \gamma\gamma)^2$ where $B(\omega \rightarrow \pi^0\gamma)$ and $B(\pi^0 \rightarrow \gamma\gamma)$ are taken from the PDG.

A (nb)	6.89 ± 0.11
D	22.0 ± 2.5
$\sigma_{peak} \equiv A_R^2$ (nb)	0.0036 ± 0.0211
$COV_{A,D}$	0.265
COV_{A,A_R}	0.021
COV_{D,A_R}	0.005

Table 5.3: Results from the Fit to η_c Data

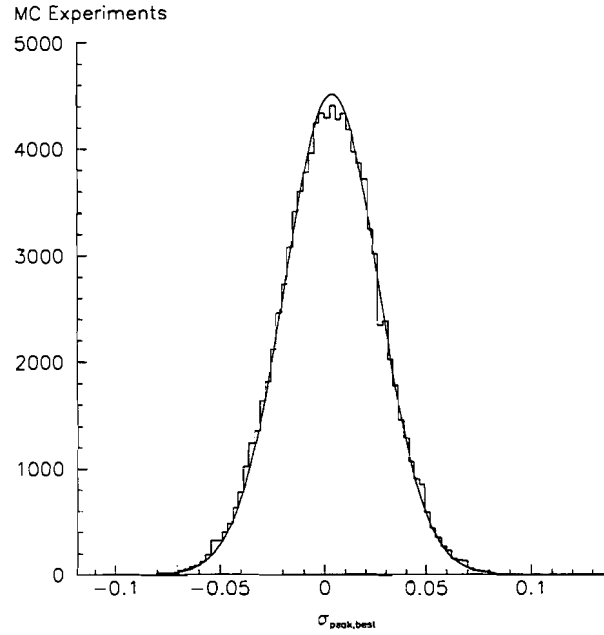


Figure 5.17: Best Fit Values for σ_{peak} for 10^5 MC Experiments

$B(\omega \rightarrow \pi^0 \gamma) = 8.5\%$ and $B(\pi^0 \rightarrow \gamma \gamma) = 98.0\%$.

Since the fit value for σ_{peak} is consistent with 0, it is problematic trusting the errors returned by Minos. For this reason, a Monte Carlo set of 10^5 experiments was run using the parameters as listed above, but treating the inputs (efficiencies, luminosity, etc.) as Gaussian random variables and the number of events at an energy as Poisson random variables.

The fit was done for each “experiment” and the results of $\sigma_{peak,best}$ for each is plotted as figure 5.17. The plots fits nicely to a Gaussian with mean $\sigma_{peak,best} = 0.0035$ and standard deviation $\Delta_{\sigma_{peak,best}} = 0.0234$.

The fact that the mean value distribution spans the physical boundary (i.e. the cross section must be non-negative) makes this an ideal problem for using the frequentist (anti-Bayesian) confidence level calculation approach of Feldman and Cousins [61]. The approach to calculating confidence levels discussed in their paper

allows for proper full coverage of the confidence interval not always achieved in the Bayesian approach (e.g. sometimes the “90%” confidence interval contains less – or more – than 90% of the probability), particularly when a parameter encounters a physical boundary. In addition, it does not require an a prior subjective probability density function or using the “hypothesis of desperation” [62, pages 102-117].

Using the tables calculated in Feldman and Cousins’s paper, the upper limit can be found for σ_{peak} . Through equation 5.5, the 90% upper limit on $B(\bar{p}p \rightarrow \eta_c) \times B(\eta_c \rightarrow \omega\omega)$ is

$$B(\bar{p}p \rightarrow \eta_c) \times B(\eta_c \rightarrow \omega\omega) < 6.55 \times 10^{-6} \quad (5.6)$$

Taking the PDG value for the branching ratio $B(\bar{p}p \rightarrow \eta_c) = (1.2 \pm 0.4) \times 10^{-3}$, the upper limit for $\omega\omega$ production in the $\delta = 180^\circ$ case is

$$B(\eta_c \rightarrow \omega\omega) < 5.4 \times 10^{-3} \quad 90\% \text{ Confidence Interval} \quad (5.7)$$

$$B(\eta_c \rightarrow \omega\omega) < 3.1 \times 10^{-3} \quad \text{PDG value} \quad (5.8)$$

Using this technique, the upper limit can be calculated over the entire range of possible phase shifts. The result is shown as figure 5.18.

The ranges on the plot may seem large at first glance – from a low at 180° of 0.54% to a high at 0° of 16%. Consider figure 5.19 where an arbitrary value for A_R , $A_R = 3.4$, is entered in equation 5.3 with the values for A and D taken from table 5.3. The upper limit is a calculation of how likely it is to see a curve due to the size of a particular parameter, given the real data and errors on the data. Curves that are most “dramatic” in shape will be fit easier with smaller parameter

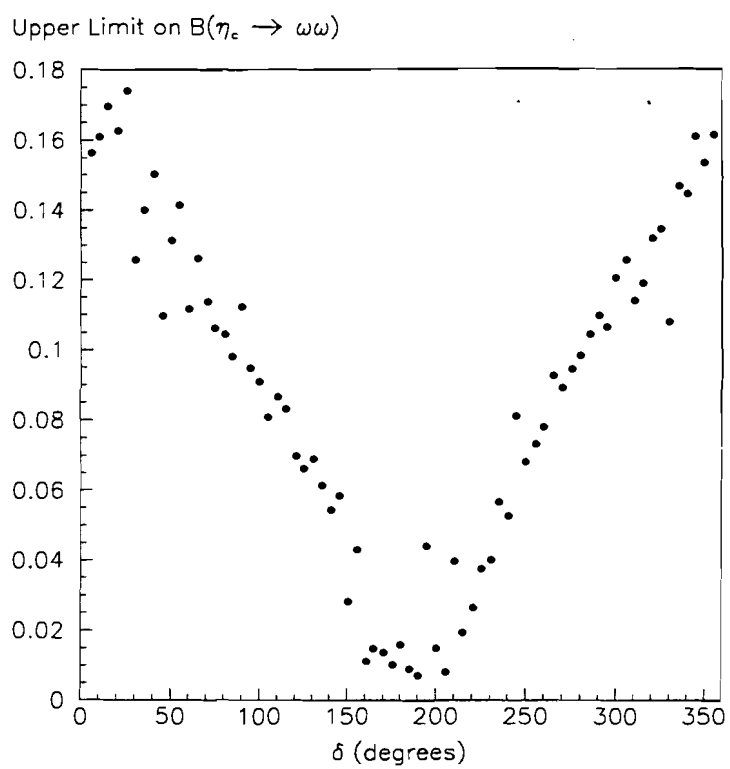


Figure 5.18: Upper Limit of $B(\eta_c \rightarrow \omega\omega)$ versus Phase Shift

upper limits. For example, in figure 5.19, the $\delta = 0^\circ$ phase shift cascades down the nonresonant background, whereas $\delta = 180^\circ$ has the steepest incline over the shortest energy range. It is apparent from the figure that the upper limit on the peak cross section will be very different in these cases.

When the assumption is made that there is no interference and the data fits simply to a Breit-Wigner plus a nonresonant background falling with center of mass energy, the upper limit obtained is (on a 90% confidence interval),

$$B(\bar{p}p \rightarrow \eta_c) \times B(\eta_c \rightarrow \omega\omega) < 7.1 \times 10^{-5} \quad (5.9)$$

$$B(\eta_c \rightarrow \omega\omega) < 5.9\% \quad (5.10)$$

5.4.3 Upper Limit of the η'_c

The E835 search for the η'_c was conducted via data taking in the range 3.575 GeV to 3.665 GeV. No η'_c signal was seen in the two photon channel [63]. The unconfirmed Crystal Ball observation of the η'_c was roughly 3594 MeV [64]. Theoretical estimates based on the potential modeled spectroscopy of $\bar{c}c$ tend to place this second radial excitation of the pseudoscalar $\bar{c}c$ bound state near 3.6 GeV. Though no signal was seen in the $\omega\omega$ channel, an upper limit on $B(\bar{p}p \rightarrow \eta'_c) \times B(\eta'_c \rightarrow \omega\omega)$ is given.

As the mass and width of the η'_c are unknown, the upper limit was calculated for a variety of possibilities. With assumed total widths of 5.0 MeV, 10.0 MeV, and 15.0 MeV, the mass of the η'_c was allowed to vary from 3.575 GeV to 3.665 GeV in steps of 0.5 MeV.

These widths and masses were then used to calculate for each set, according

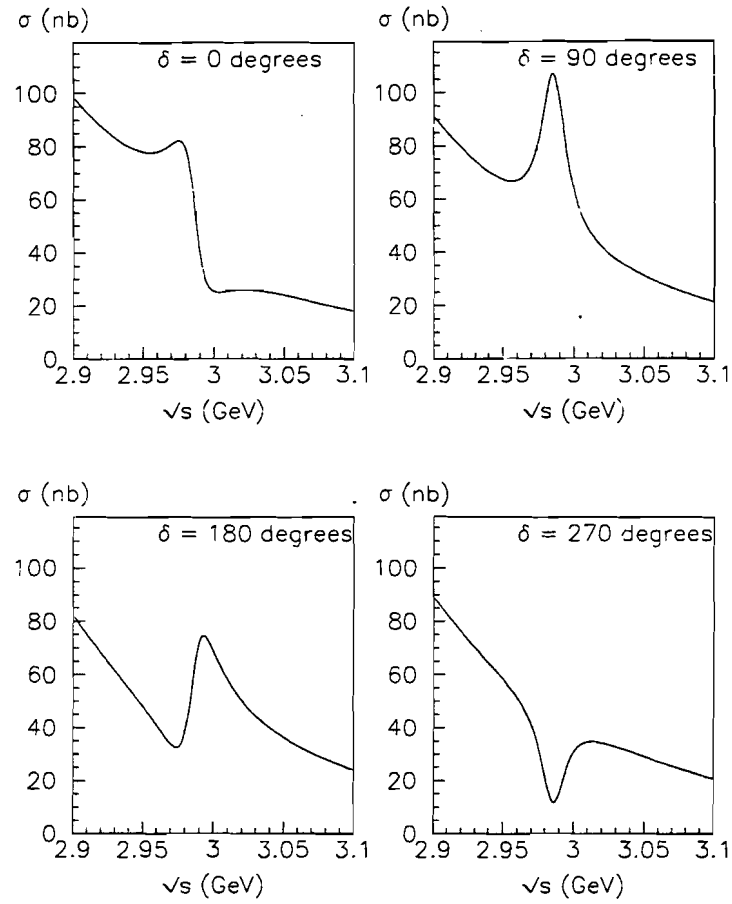


Figure 5.19: Interference when Cross Section Falls with \sqrt{s} for A_R Arbitrarily Chosen as Half the Nonresonant Continuum Amplitude and for Various Values of Phase Shift

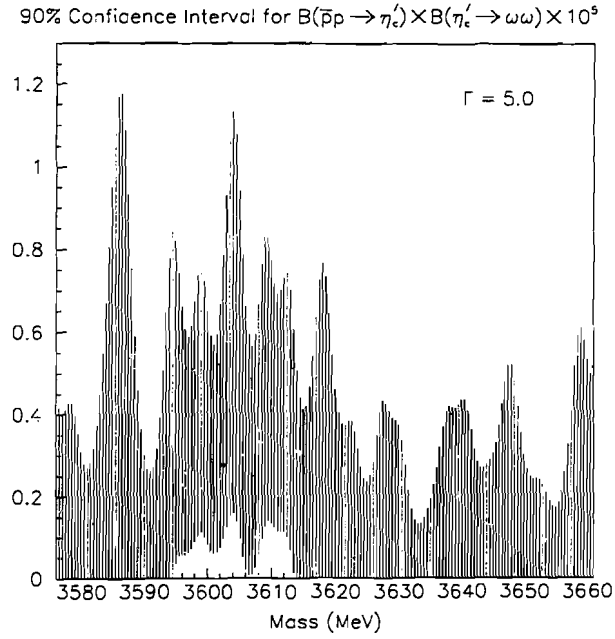


Figure 5.20: 90% Confidence Interval Upper Limit for $B(\bar{p}p \rightarrow \eta'_c) \times B(\eta'_c \rightarrow \omega\omega)$ for Various η'_c Masses, a Width of 5.0 MeV, and $\delta = 90^\circ$

to equations 5.3 and 5.4, a 90% confidence level bound on the product of the aforementioned branching ratios under the assumption of a 90° phase shift. Figures 5.20, 5.21, and 5.22 show these bounds as a function of the η'_c (assumed) mass for $\Gamma = 5.0, 10.0$, and 15.0 MeV respectively.

The background parameters, A and D , from equation 5.3 for the entire grid point search were all consistent with $A = 1.22 \pm 0.16$ and $D = 1.33 \pm 0.06$ with a high correlation between them on the order of -0.8 .

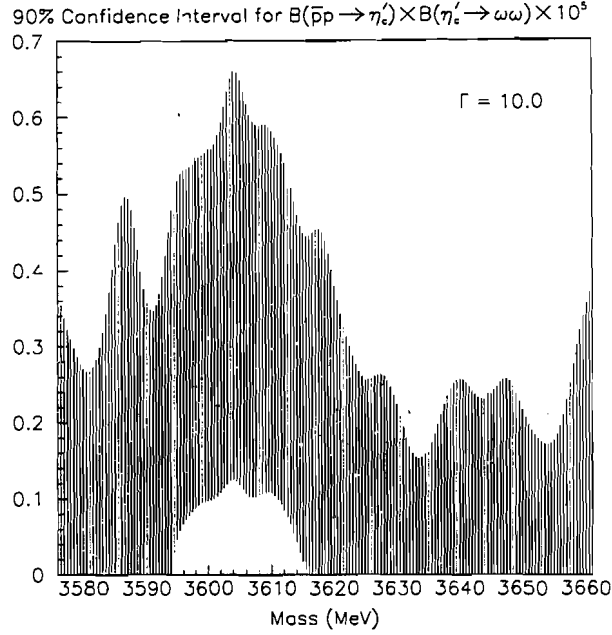


Figure 5.21: 90% Confidence Interval Upper Limit for $B(\bar{p}p \rightarrow \eta'_c) \times B(\eta'_c \rightarrow \omega\omega)$ for Various η'_c Masses, a Width of 10.0 MeV, and $\delta = 90^\circ$

The energy dependence of the upper limit is much smoother for the larger widths, $\Gamma = 10.0$ and 15.0 MeV, than for the $\Gamma = 5.0$ MeV assumptions. This results from the spacing of the energy points at which data was taken – they are too separated for an accurate search for such a width. Thus, the valleys in the $\Gamma = 5.0$ MeV plot are all at the energy points where data was actually taken. The peaks are highest where the energy points' luminosity weighted center of gravity is smallest.

The upper limit is taken to be the largest upper limit in the range of masses and is (for $\delta = 90^\circ$),

$$B(\bar{p}p \rightarrow \eta'_c) \times B(\eta'_c \rightarrow \omega\omega) < 1.18 \times 10^{-6} \quad \Gamma = 5.0 \text{ MeV} \quad (5.11)$$

$$B(\bar{p}p \rightarrow \eta'_c) \times B(\eta'_c \rightarrow \omega\omega) < 0.66 \times 10^{-6} \quad \Gamma = 10.0 \text{ MeV} \quad (5.12)$$

$$B(\bar{p}p \rightarrow \eta'_c) \times B(\eta'_c \rightarrow \omega\omega) < 0.56 \times 10^{-6} \quad \Gamma = 15.0 \text{ MeV} \quad (5.13)$$

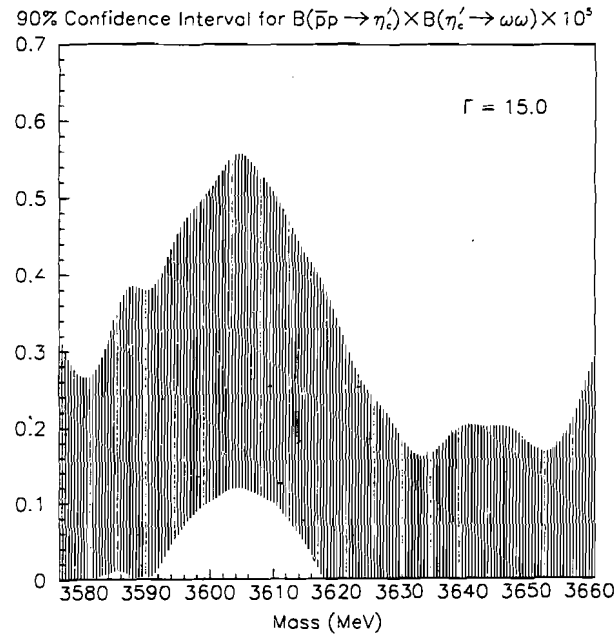


Figure 5.22: 90% Confidence Interval Upper Limit for $B(\bar{p}p \rightarrow \eta'_c) \times B(\eta'_c \rightarrow \omega\omega)$ for Various η'_c Masses, a Width of 15.0 MeV, and $\delta = 90^\circ$

The upper limits on the η'_c production and decay branching ratios are about an order of magnitude smaller than for the η_c . This is the result of primarily three items: the continuum is somewhat flatter in the η'_c region, there was more luminosity taken there (about 2.5 times as much as in the η_c region), and the nonresonant continuum is much smaller (by almost two orders of magnitude).

5.5 Conclusions

Below the open charm threshold only a few pure hadronic final states have been measured using $\bar{p}p$ annihilation. Since the ω is a vector particle, $\omega\omega$ is accessible

via several J^{PC} intermediate states (in fact all the even C states – see table 4.3). Potentially it can provide a common channel to study many of the $\bar{c}c$ resonances, especially the singlet states. If the η_c could be measured via $\omega\omega$, there is greater hope of confirming the 1P_1 as it should predominantly decay via an E1 radiative transition to $\gamma\eta_c$.

It is reasonable to expect that annihilating all six valence quarks in a $\bar{p}p$ pair is dependent on the incoming relative angular momentum (L) of the particles. That is, if we think in terms of classical impact parameters, the larger the impact parameter, and so the larger L , the harder it will be for the six quarks to each annihilate. In the quantum mechanical case this is more complicated since the momentum of particles is spread out. A detailed calculation along these lines is beyond the scope of this thesis and to the author's knowledge no such calculation has been performed. Realize, however, it is not the overlap of the proton and antiproton de Broglie wavelengths that is relevant in total annihilation of $\bar{p}p$, but rather the overlap of *all* the valence quarks' de Broglie wavelengths.

As we are searching for charmonium, these class 3 reactions (see section 1.3.1) are the ones of interest. Class 3 events are strongest in the initial $L = 0$ state and since for $\omega\omega$, $L = 0$ results in an intermediate pseudoscalar state (and so flat in $\cos\theta^*$), the low $\cos\theta^*$ region of the $\omega\omega$ data is the most relevant place to look. In fact, in this region it was estimated, based on the angular distribution, that 0^{-+} is dominant at the level of at most 86%. This effect is seen also in the current $\pi^0\pi^0$ analyses where the $L = 1$ $\bar{p}p$ relative angular momentum dominates over the $L = 3$ for low $\cos\theta^*$ values [56, 57].

With that estimate and assuming interference of resonant and nonresonant continuum s-wave $\omega\omega$, upper limits on the unknown branching ratios, $B(\bar{p}p \rightarrow \eta_c) \times B(\eta_c \rightarrow \omega\omega)$ were calculated for all possible phase differences, $\delta \in [0^\circ, 360^\circ]$. The

minimum value obtained was for $\delta = 180^\circ$, the maximum was for $\delta = 0^\circ$ and the value obtained at $\delta = 90^\circ, 270^\circ$ was the same as the value obtained assuming no interference takes place. Table 5.4 summarizes the η_c results – note that the Particle Data Group lists the $\bar{p}p$ to η_c branching ratio as $B(\bar{p}p \rightarrow \eta_c) = (1.2 \pm 0.4) \times 10^{-3}$.

δ	Upper Limit For	
	$B(\bar{p}p \rightarrow \eta_c) \times B(\eta_c \rightarrow \omega\omega) \times 10^{-5}$	$B(\eta_c \rightarrow \omega\omega) \times 10^{-3}$
180°	0.655	5.4
$90^\circ, 270^\circ$	7.2	59
0°	207	170
—	PDG Value \rightarrow	3.1

Table 5.4: 90% Confidence Level Upper Limit for Branching Ratios for η_c to $\omega\omega$ and $\bar{p}p$ to η_c to $\omega\omega$

The upper limit on the η'_c unknown branching ratios was calculated over a range of phase shifts (deltas), masses, and widths. The results come in about an order of magnitude lower than for the η_c due to the large drop off of continuum $\omega\omega$ at the higher energies. For $\delta = 90^\circ$, for example, the largest upper limits for the entire range of masses searched are listed in table 5.5.

One of the more puzzling questions to arise is why should, η_c for instance, have such a relatively small branching ratio to $\omega\omega$ as compared to other vector-vector final states. Consider table 5.6.

Haber and Perrier [28], among others, suggest that with unbroken flavor SU(3) symmetry, the reduced branching ratios, defined as $\tilde{B}(\eta_c \rightarrow VV) = B(\eta_c \rightarrow VV)/|\vec{p}_V|^3$ for vector mesons, V, with center of mass momentum, \vec{p}_V , would be equal for the final states in table 5.6 (except $K^*\bar{K}^*$ which must be reduced by a

Γ (MeV)	Upper Limit For $B(\bar{p}p \rightarrow \eta'_c) \times B(\eta'_c \rightarrow \omega\omega) \times 10^{-6}$
5.0	1.18
10.0	0.66
15.0	0.56

Table 5.5: 90% Confidence Level Upper Limit for Branching Ratios of $\bar{p}p$ to η'_c to $\omega\omega$ for a 90° Phase Shift and Assumed η'_c Width Γ

final state	$B(\eta_c \rightarrow \text{final state}) \times 10^{-3}$
$\rho\rho$	26 ± 9
$K^*\bar{K}^*$	8.5 ± 3.1
$\phi\phi$	7.1 ± 2.8
$\omega\omega$	< 3.1

Table 5.6: Branching Ratios of η_c to Various Vector-Vector Final States

factor of two). Or in terms of standard branching ratios,

$$B(\eta_c \rightarrow \omega\omega) \approx B(\eta_c \rightarrow \rho\rho) \approx 1.17B(\eta_c \rightarrow \phi\phi) \approx 0.53B(\eta_c \rightarrow K^*\bar{K}^*) \quad (5.14)$$

It has been suggested that a possible strange quark dependence on the charmonium production of vector-vector final states develops from the SU(3) flavor symmetry breaking [28], but this doesn't hold up when one looks at $\rho\rho$. Equation 5.14 applies before SU(3) flavor symmetry breaking. The data we see puts the ratios of the reduced branching ratios, $\tilde{B}(\eta_c \rightarrow \rho\rho) : \tilde{B}(\eta_c \rightarrow \phi\phi) : \frac{1}{2}\tilde{B}(\eta_c \rightarrow K^*\bar{K}^*) : \tilde{B}(\eta_c \rightarrow \omega\omega)$ in the ratio (assuming the upper limit for $\omega\omega$), 8.5:2.7:1.5:1. Why should $\rho\rho$ have such a relatively large partial width?

Consider again the class 3 subprocesses in figure 1.11 repeated here as figure 5.23. Again, $K^*\bar{K}^*$ can not come from (b) and, for example, $\phi\omega$ can only come from (b),

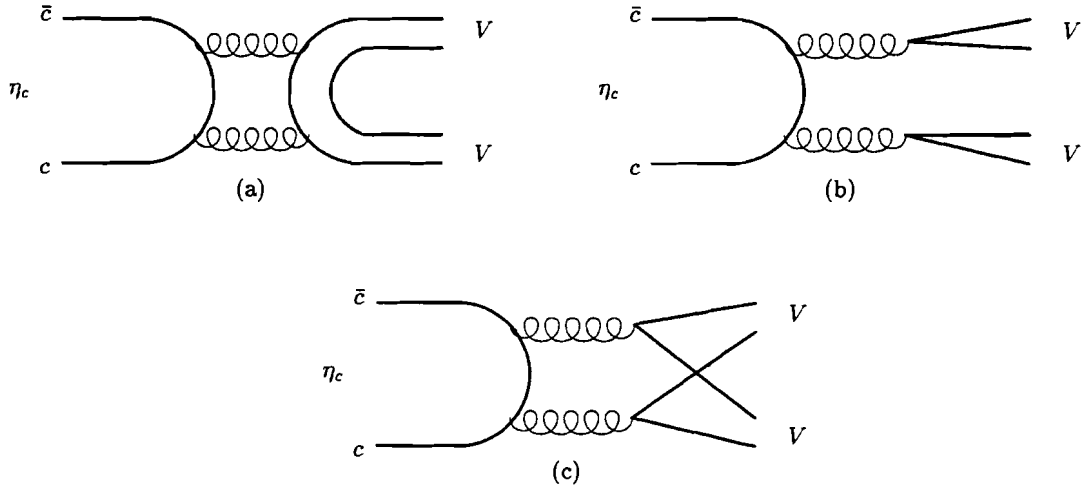


Figure 5.23: Mechanisms for η_c Decay to Two Mesons. Note (b) results in a color octet that is assumed to become singlet under a final state gluon exchange.

whereas the identical vector-vector final states can result from all three. Calculations (again see reference [28]) suggest that (b) may dominate (color vector dominance [65]) as $\rho\rho$ has a higher branching ratio than $\phi\phi$ and $\frac{1}{2}K^*\bar{K}^*$ is relatively suppressed. Once the $\omega\omega$ ratio is known, the picture may clear up on how these processes contribute to η_c decay to hadrons.

Our detector is optimized for electromagnetic particle detection, and though omega mesons are seen quite easily, the continuum is large and the acceptance of $\omega\omega$ detection is low enough so as to make a discovery improbable. The necessity of looking for $\omega\omega$ through the ω decay to $\pi^0\gamma$ – and note that $B(\omega \rightarrow \pi^0\gamma)^2 = 0.7 \times 10^{-2}$ – instead of the more copious $\pi^+\pi^-\pi^0$ channel with $B(\omega \rightarrow \pi^+\pi^-\pi^0)^2 = 0.79$ provided another hurdle.

Perhaps a similar experiment, run with a magnet to identify Kaons, could use

the techniques presented here to detect charmonium in $\phi\phi$. This channel would suffer less nonresonant continuum (classes 0, 1, and 2 are automatically excluded for this $\bar{s}s$ state) and, since $B(\phi \rightarrow K^+K^-) = 49.2\%$ it would not suffer from the small branching ratio which plagues $\bar{c}c$ detection by $\omega\omega$ in all neutral ω decays.

Appendix A

Neutral Trigger Performance

During E835 running it was important to monitor the neutral trigger performance since it provided the triggers from the CCAL, including the total energy and PBG triggers (see section 3.2.2), as well as the strobe for clocking most of the logic modules. Any failure of neutral trigger hardware or unintended changes in thresholds of discriminators could seriously affect data sets and introduce unknown inefficiencies.

While data taking was in progress, online histograms of all neutral trigger ADCs and TDCs, from total energy signals, ring sums, super-block signals, and logic modules' TDCs down to level II summer outputs (minimum bias signals) were monitored. Trigger rates were also checked periodically for unusual occurrences. Between these two checks, most problems could be quickly found and remedied. After the run ended, data for that run was analyzed to obtain a better performance report. Most important was examination of the thresholds set by the discriminators which sent the logic signals to the NMLU and created the strobe.

Although we determined what energy we desired each discriminator to be set at, the actual setting must be in units of millivolts. The conversion from energy to

mV is a function of the electronics and hardware leading up to the discriminator. It is particularly sensitive to the high voltage used to set the CCAL block gains since that directly relates to pulse shape and height of PMT signals and thus, after integration, to the signal height entering the discriminator.

The conversion (MeV/mV) was initially calculated at the beginning of the experiment and used each time in the software setup before data taking at a particular energy began. The thresholds were then monitored to ensure the wrong mV setting had not been used or that the conversion constant had not changed (which would be possible when high voltages were changed to adjust gains for the effects of radiation damage to blocks or when neutral trigger hardware upstream of the discriminator was replaced, etc.).

A.1 Threshold Monitoring

To calculate the energy that the thresholds were set to, the signals from the 1280 CCAL blocks were used to duplicate offline what happened in the hardware during data taking. Minimum bias data (PRUDE id 120 ... see table 3.9) was used for the calculation.

The first task was to sum the energies from the 1280 blocks into the 40 super-blocks (as was done by the level 1 and 2 summers). For each super-block, the energy distribution for a run was found and divided by the energy distribution when there was a TDC hit from the super-block discriminator (i.e. there was a hit above threshold in that super-block). This gave a threshold curve. The curves for the super-blocks were fit to a hyperbolic tangent function of the form

$$\text{fraction} = \frac{1}{2} + \frac{1}{2} \tanh(\sigma(\text{energy} - \mu)) \quad (\text{A.1})$$

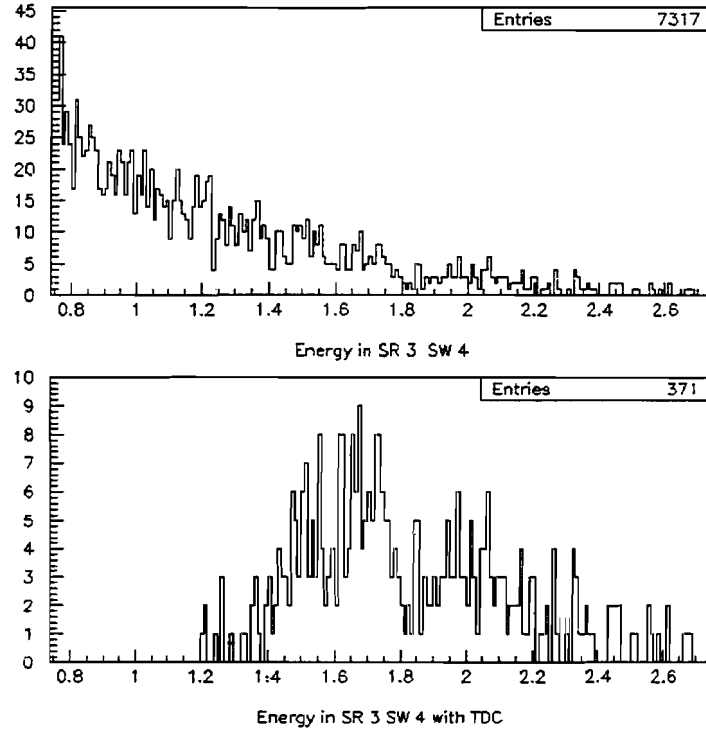


Figure A.1: Super-Block (3,4) Energy Distribution in GeV (top) and When There was a TDC Hit (bottom)

where σ is the resolution and μ is the *fraction* = 50% value of the fit. The set discriminator value could then be compared to the curve. Generally, it was considered acceptable when the set value of the energy fell within *fraction* = 10% to 90%. A sample of the distributions described above is shown as figures A.1 and A.2. This technique also allowed for checking the consistency of thresholds among super-blocks in a common super-ring (which should all have the same settings).

The same technique was modified to check the thresholds of the other energy discriminators, e.g. total energy, ring sum, and minimum bias discriminators. Fig-

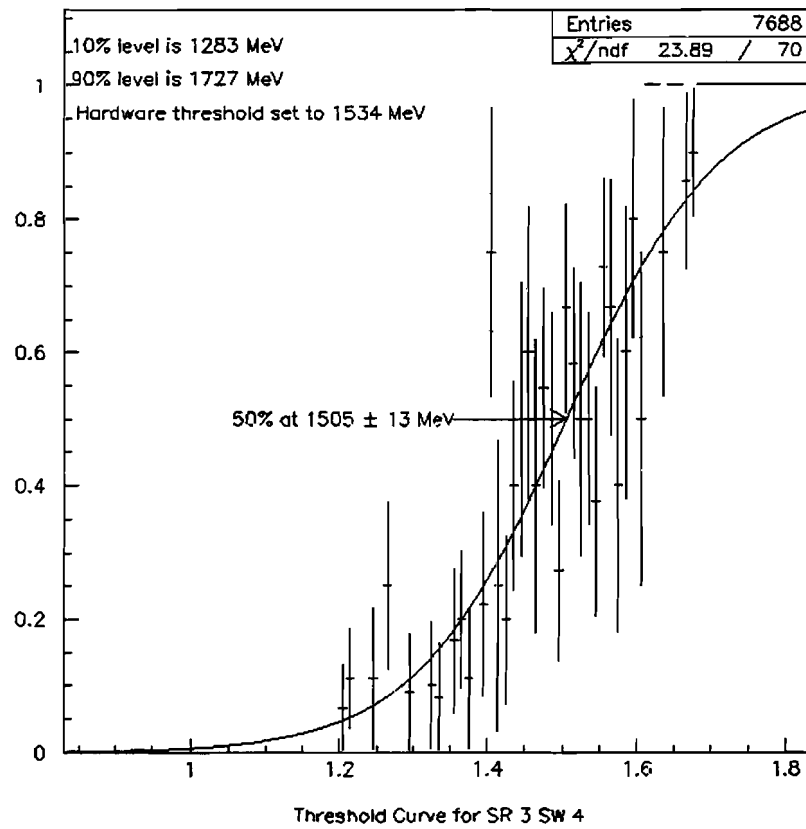


Figure A.2: Threshold Curve. The error bars are binomial.

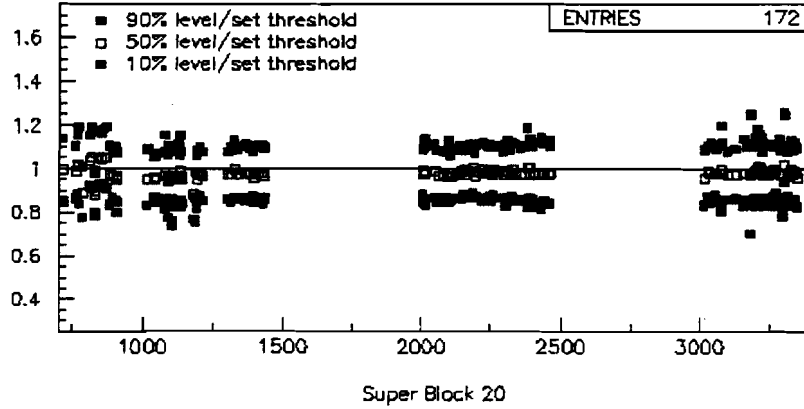


Figure A.3: Threshold Levels vs. Run for Super-Block 20

Figure A.3 shows the 10%, 50%, and 90% values from the fit versus run for one super-block as an example showing the consistency of the super-block settings.

A.2 PBG Efficiencies

For efficiency calculations, real physics events were used since it must be known that the event should have been assigned a specific trigger. Since our detector was well suited for identification of neutral pions, $\pi^0\pi^0 \rightarrow 4\gamma$ events were chosen for efficiency studies. The following selection criteria were used:

- There must be exactly four intime clusters in the calorimeter (see section 2.3.4 for definitions of intime).
- The π^0 candidates must be back to back to within 25 mrad.
- Using one candidate π^0 's energy and angles, the θ for the other π^0 candidate must be within 12 mrad of its predicted value (based on $\pi^0\pi^0$ kinematics).

- Each π^0 candidate invariant mass must be within 35 MeV of the known π^0 mass.

Once the $\pi^0\pi^0$ events were selected, much of the procedure outlined above for threshold determination was followed. That is, the energies for the super-blocks were found and compared with the set discriminator values. If the energy for some super-block in a super-wedge was greater than the threshold set for its super-ring, and the opposing super-wedge (one of the three opposing super-wedges) had a super-block energy above its super-ring threshold, a PBG1 (PBG3) software trigger was recorded. A hardware trigger was present when the MMLU input bit 1 was set (a PBG1 trigger) or when MMLU input bit 2 was set (a PBG3 trigger). The calculated efficiency was the ratio of the number of events with both the hardware and software trigger to the number of events with a software trigger only.

The PBG3 efficiency was consistent with 100% for the entire run. The PBG1 efficiency was essentially over 99% for the entire run. One exception was for runs 1371-2108 during which time a replaced discriminator for super-ring 4 was mistakenly set with too narrow of a window causing a substantial decrease in efficiency for those runs¹. Figures A.4 and A.5 show the efficiency as a function of run and energy respectively.

A.3 Total Energy Efficiencies

Only the efficiency for the ETOT-HIGH trigger was calculated as ETOT-LOW was only used for diagnostics. The method followed was analogous to the method

¹This range is not as large as it appears since most runs from the late 1300's to the late 2090's did not exist.

$\epsilon_{ETOT-HIGH}$	Energy Range (GeV)
99%	< 3.2
98%	3.2 - 3.9
99%	> 3.9

Table A.1: ETOT-HIGH Efficiencies

followed for the PBG triggers. The total energy trigger efficiency was about 95% for all runs. Table A.1 shows the values used for this analysis.

Figures A.6 and A.7 show the ETOT-HIGH efficiency versus run and energy respectively. Note that the total energy efficiency was not affected by the misset PBG discriminator since it was along a different electronics stream.

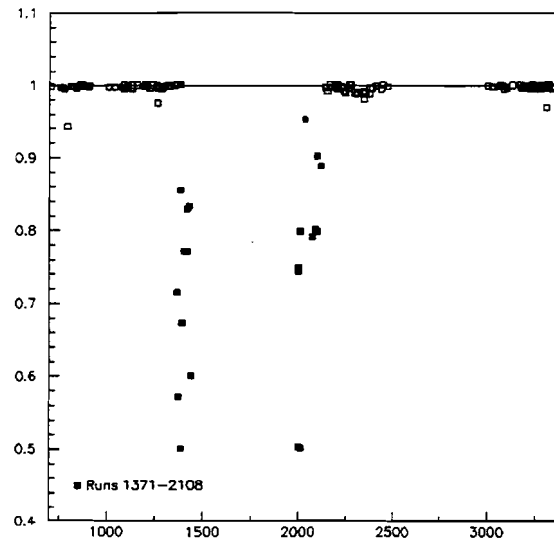


Figure A.4: PBG1 Trigger Efficiency versus Run. The low efficiencies are from runs 1371-2108 when a discriminator width was improperly set.

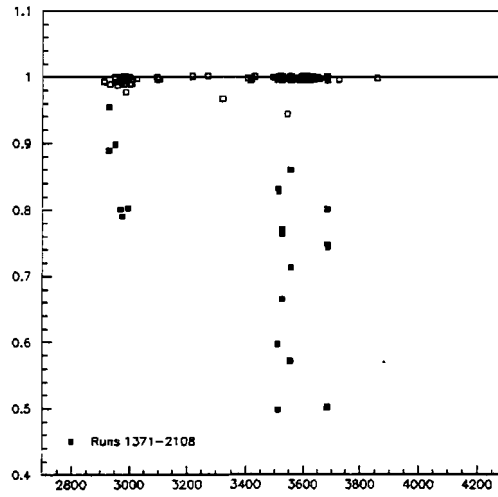


Figure A.5: PBG1 Trigger Efficiency versus Energy (MeV). The low efficiencies are from runs 1371-2108 when a discriminator width was improperly set.

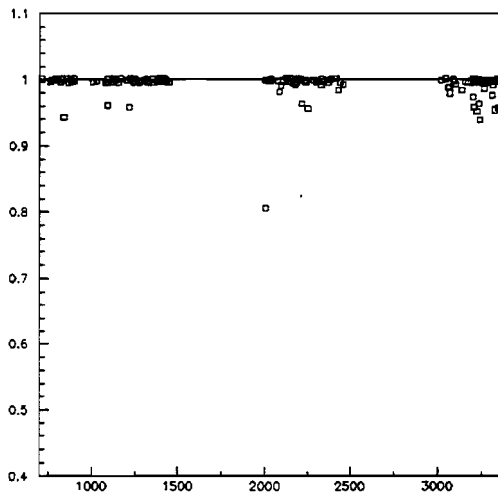


Figure A.6: ETOT-HIGH Trigger Efficiency versus Run

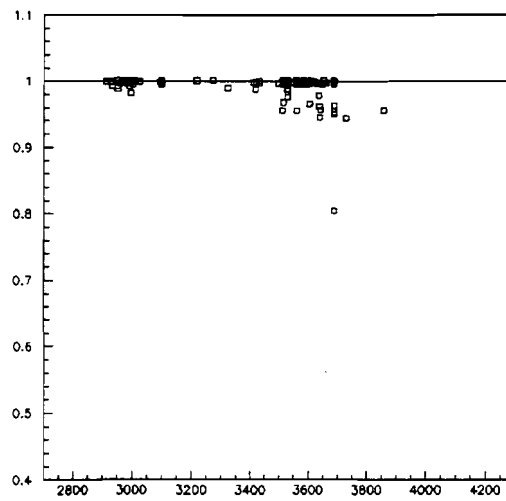


Figure A.7: ETOT-HIGH Trigger Efficiency versus Energy (MeV)

Appendix B

Neutral Data Summary Tapes

The Neutral Data Summary Tapes (NDSTs) were created to compact the data for neutral final state events and classify them by event topology. With the large amount of data, these steps make offline analysis for any of the neutral analyses quicker and easier with acceptable loss of efficiency.

The NDSTs were produced over a three month period on the Fermilab computer farm system by a group of three E835 personnel (one of whom was this author). Our raw data tapes were in the Fermilab 8mm tape vault where they were loaded into drives using the OCS software existing on the SGI machines dedicated for our use. Code based on the E835 offline summarized and classified the events by the number of calorimeter clusters and wrote them to various filesystems – this process was called staging. When a directory approached 5 GB (the amount of data an 8mm tape holds), all the data from each classification was written back to tapes (one tape would hold four cluster events, one would hold five cluster events, etc.) – this process was called spooling.

The NDSTs were created from the E835 raw data tapes with GN and GK prefixes

(i.e. where the neutral tagged final state events were streamed – see section 3.5). The following cuts were applied to data being written to the NDSTs:

1. Events Must have less than 10 and more than one PRUDE cluster (see section 3.5)
2. $P_t \equiv \sqrt{P_x^2 + P_y^2} \leq 350 \text{ MeV}$
3. $|P_z - P_{beam}| \leq 0.15 \times P_{beam}$

where \vec{P} is the vector sum of all the momenta associated with an intime or undetermined cluster and P_{beam} is the \bar{p} beam momentum. The classification of events and information kept for the summarized data is described in detail in the E835 NDST memo [66].

Although this procedure drastically reduces the time to analyze a reaction, the cuts listed above may cause some legitimate events to be cut. In the case of the $\omega\omega$ analysis, the 6 cluster NDST was used. There are two ways that a good event can be lost. First, the event can fail the four momentum cut (cuts 3 and 4 above). For a true $\omega\omega$ event where all 6 photons were in the calorimeter, an event that failed the four momentum cut would not survive the cut on the probability of fit requirement applied later anyway. The analysis efficiency will account for these events (section 4.4).

The second way to lose a real $\omega\omega$ event is if the event had 10 or more PRUDE clusters. Since the NDST consists only of events with 6 intime or undetermined clusters, the addition of 4 or more out of time clusters above 75 MeV (a PRUDE cluster) would cause the event to be lost. The largest cause of multiple out of time events is when a preceding event has an energy tail large enough to pass the

calorimeter's cluster threshold. This effect is greater at higher \sqrt{s} as is shown for $\omega\omega$ in section 4.4.3 which details the NDST efficiency study.

Appendix C

Angular Dependence of the Differential Cross Section

The total angular momentum, parity, and charge conjugation quantum numbers for a multi-particle state determines the angular dependence of the differential cross section. The preferred method for calculation of this dependence is using helicity formalism, and in this case, using the notations and phase conventions of Jacob and Wick [58].

This method is superior to the spin-orbit formalistic approach which introduces difficulties in describing spin states since the angular momentum is defined in the center of mass frame whereas the individual spins are defined in the particles' rest frames. The helicity operator, however, (see equation 4.4) is invariant under both rotations and boosts along \hat{p} .

C.1 Brief Introduction to D-functions

For a generic two particle decay $a \rightarrow b+c$, where J is the total angular momentum of a , M is its projection along an arbitrary \hat{z} -axis, and λ denotes helicity, the amplitude, A , can be written as,

$$A = \langle \theta, \phi, \lambda_b, \lambda_c | U | J, M \rangle \quad (\text{C.1})$$

U is the propagator taking the initial state to the final state, and since the momentum of b and c are equal and opposite in the center of mass frame, they can be abandoned in the amplitude description in place of the directions, θ and ϕ , of b 's decay relative to the quantization axis (\hat{z}). $|A|^2$ is now the probability that the decay results in b departing at angles θ and ϕ .

Since angular momentum is conserved, a complete set of two particle plane-wave helicity states can be introduced to equation C.1,

$$\begin{aligned} A &= \sum_{j,m} \langle \theta, \phi, \lambda_b, \lambda_c | j, m, \lambda_b, \lambda_c \rangle \langle j, m, \lambda_b, \lambda_c | U | J, M \rangle \\ &= \sum_{j,m} \langle \theta, \phi, \lambda_b, \lambda_c | j, m, \lambda_b, \lambda_c \rangle \delta_{m,M} \delta_{j,J} A_{\lambda_b, \lambda_c} \\ &= \langle \theta, \phi, \lambda_b, \lambda_c | J, M, \lambda_b, \lambda_c \rangle A_{\lambda_b, \lambda_c} \end{aligned} \quad (\text{C.2})$$

Consider $R(\alpha, \beta, \gamma)$ to be the rotation operator for the set of all rotations between angular momentum states, where α, β, γ are the Euler angles describing the rotation. The functions that are the matrix elements of R are the D-functions, $D_{m',m}^J(\alpha, \beta, \gamma)$. It can be shown [68] that the transformation of the two particle plane-wave helicity basis to the two particle spherical-wave helicity basis, $|\theta, \phi, \lambda_b, \lambda_c \rangle$, is

$$\langle \theta, \phi, \lambda_b, \lambda_c | J, M, \lambda_b, \lambda_c \rangle = C_J D_{M, \lambda_b - \lambda_c}^{J*}(\phi, \theta, -\phi) \quad (\text{C.3})$$

where the * implies the complex conjugate, C_J is a normalization which can be easily calculated as $\sqrt{\frac{2J+1}{4\pi}}$, and (the Euler angle) γ , being arbitrary, can without loss of generality be chosen to be $-\phi$ ¹.

From equations C.2 and C.3, the amplitude for the two particle decay, $a \rightarrow b + c$, is given by

$$A = \sqrt{\frac{2J+1}{4\pi}} D_{M, \lambda_b - \lambda_c}^{J*}(\phi, \theta, -\phi) A_{\lambda_b, \lambda_c} \quad (\text{C.4})$$

The interpretation of this given in reference [68] is as follows: the decay amplitudes are equal for a particle with spin J and projection of spin along the \hat{z} -axis, M , and a particle to have spin projection $\lambda_b - \lambda_c$ along the decay axis $\hat{n}(\theta, \phi)$ (multiplied by the coupling to the final state helicities, A_{λ_b, λ_c}).

Now, from the definition of $R(\alpha, \beta, \gamma)$,

$$R(\alpha, \beta, \gamma) = e^{-i\alpha J_z} e^{-i\beta J_y} e^{-i\gamma J_z} \quad (\text{C.5})$$

it can be derived (using the angular momentum eigenstates, $|j, m\rangle$), that

$$D_{m', m}^{J*}(\phi, \theta, -\phi) = e^{i\phi m'} d_{m', m}^J(\theta) e^{-i\phi m} \quad (\text{C.6})$$

where

$$\begin{aligned} d_{m', m}^J(\theta) = & \sum_n \left\{ \frac{(-1)^n [(J+m)!(J-m)!(J+m')!(J-m')!]^{\frac{1}{2}}}{(J-m-n)!(J+m-n)!(n+m'-m)!n!} \right. \\ & \left. \times (\cos \frac{\theta}{2})^{2J+m-m'-2n} (-\sin \frac{\theta}{2})^{m'-m+2n} \right\} \end{aligned}$$

¹The choice of $\gamma = -\phi$ makes many of the calculations easier.

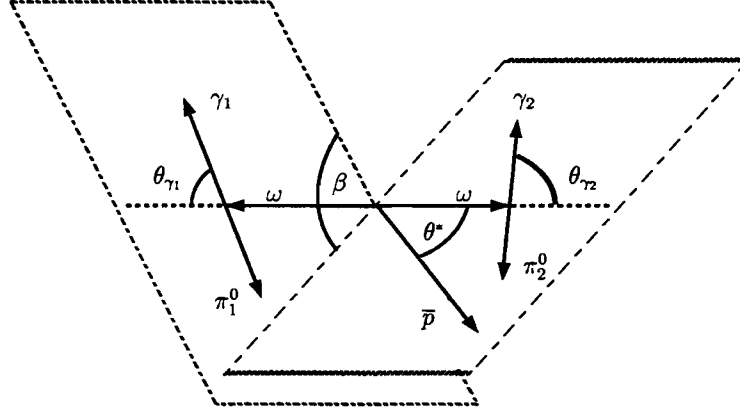


Figure C.1: Angles Describing the $\omega\omega$ Production and Decay

C.2 Calculation of the $\omega\omega$ Distribution

Using the definitions above, the angular distribution can now be calculated for the specific process, $\bar{p}p \rightarrow \omega\omega \rightarrow 2\pi^0 2\gamma \rightarrow 6\gamma$ using the notation for the particles as defined on page 94. Figure C.1 shows the representation of the reaction in the standard helicity type format where the relevant angles for each decay are defined in terms of the direction of one of the decay products in its mother's center of mass frame and using the mother's direction in its grandmother's rest frame as the polar axis for that process. Note that the π^0 decays are not represented here as they will not contribute to the final answer (their decays are isotropic).

For the process proceeding through an initial state with quantum numbers J^{P+} ($C = +1$ for production of two omegas) and \hat{z} -axis (beam axis) projection of spin,

m , the amplitudes for each stage are

$$\begin{aligned}
A(\bar{p}p \rightarrow J^P) &\propto f_{\lambda_p, \lambda_{\bar{p}}} D_{m, \lambda_p - \lambda_{\bar{p}}}^J(\phi_p, \theta_p, -\phi_p) \\
A(J^P \rightarrow \omega_1 \omega_2) &\propto a_{\lambda_{\omega_1}, \lambda_{\omega_2}} D_{m, \lambda_{\omega_1} - \lambda_{\omega_2}}^{J*}(\phi_{\omega_1}, \theta_{\omega_1}, -\phi_{\omega_1}) \\
A(\omega_1 \rightarrow \pi_1^0 \gamma_1) &\propto b_{\lambda_{\gamma_1}, \lambda_{\pi_1^0}} D_{\lambda_{\omega_1}, \lambda_{\gamma_1} - \lambda_{\pi_1^0}}^{J_{\omega_1}*}(\phi_{\gamma_1}, \theta_{\gamma_1}, -\phi_{\gamma_1}) \\
A(\omega_2 \rightarrow \pi_2^0 \gamma_2) &\propto c_{\lambda_{\gamma_2}, \lambda_{\pi_2^0}} D_{-\lambda_{\omega_2}, \lambda_{\gamma_2} - \lambda_{\pi_2^0}}^{J_{\omega_2}*}(\phi_{\gamma_2}, \theta_{\gamma_2}, -\phi_{\gamma_2}) \\
A(\pi_1^0 \rightarrow \gamma_a \gamma_b) &\propto d_{\lambda_{\gamma_a}, \lambda_{\gamma_b}} D_{\lambda_{\pi_1^0}, \lambda_{\gamma_a} - \lambda_{\gamma_b}}^{J_{\pi_1^0}*}(\phi_{\gamma_a}, \theta_{\gamma_a}, -\phi_{\gamma_a}) \\
A(\pi_2^0 \rightarrow \gamma_c \gamma_d) &\propto e_{\lambda_{\gamma_c}, \lambda_{\gamma_d}} D_{\lambda_{\pi_2^0}, \lambda_{\gamma_c} - \lambda_{\gamma_d}}^{J_{\pi_2^0}*}(\phi_{\gamma_c}, \theta_{\gamma_c}, -\phi_{\gamma_c})
\end{aligned}$$

Note that the ω_2 helicity in the first index of the ω_2 decay D-function is negative since it is being defined (in the function) along the \hat{z} -axis defined by the direction of the oppositely moving ω . Summing over the helicities of the non-observable decays and absorbing the constants C_J into the coupling amplitudes,

$$\begin{aligned}
A^{J^{P+}}(\bar{p}p \rightarrow \omega_1 \omega_2 \rightarrow \pi_1^0 \gamma_1 \pi_2^0 \gamma_2 \rightarrow \gamma_1 \gamma_a \gamma_b \gamma_2 \gamma_c \gamma_d) &\propto \sum_{\left\{ \begin{smallmatrix} m & \lambda_{\omega_1} & \lambda_{\omega_2} \\ \lambda_{\pi_1^0} & \lambda_{\pi_2^0} \end{smallmatrix} \right\}} \quad (C.7) \\
&\left\{ f_{\lambda_p, \lambda_{\bar{p}}} a_{\lambda_{\omega_1}, \lambda_{\omega_2}} b_{\lambda_{\gamma_1}, \lambda_{\pi_1^0}} c_{\lambda_{\gamma_2}, \lambda_{\pi_2^0}} d_{\lambda_{\gamma_a}, \lambda_{\gamma_b}} e_{\lambda_{\gamma_c}, \lambda_{\gamma_d}} \right. \\
&\times D_{m, \lambda_p - \lambda_{\bar{p}}}^J(\phi_p, \theta_p, -\phi_p) D_{m, \lambda_{\omega_1} - \lambda_{\omega_2}}^{J*}(\phi_{\omega_1}, \theta_{\omega_1}, -\phi_{\omega_1}) \\
&\times D_{\lambda_{\omega_1}, \lambda_{\gamma_1} - \lambda_{\pi_1^0}}^{J_{\omega_1}*}(\phi_{\gamma_1}, \theta_{\gamma_1}, -\phi_{\gamma_1}) D_{-\lambda_{\omega_2}, \lambda_{\gamma_2} - \lambda_{\pi_2^0}}^{J_{\omega_2}*}(\phi_{\gamma_2}, \theta_{\gamma_2}, -\phi_{\gamma_2}) \\
&\times \left. D_{\lambda_{\pi_1^0}, \lambda_{\gamma_a} - \lambda_{\gamma_b}}^{J_{\pi_1^0}*}(\phi_{\gamma_a}, \theta_{\gamma_a}, -\phi_{\gamma_a}) D_{\lambda_{\pi_2^0}, \lambda_{\gamma_c} - \lambda_{\gamma_d}}^{J_{\pi_2^0}*}(\phi_{\gamma_c}, \theta_{\gamma_c}, -\phi_{\gamma_c}) \right\}
\end{aligned}$$

The final state coupling amplitudes, e and d , when squared and summed over the final state helicities, contribute only an overall constant factor to $\frac{d\sigma}{d\Omega}$ and can thus be factored out of the equation. Also, note that $J_{\pi^0} = 0$ (and so $\lambda_{\pi^0} = 0$) and

$D_{n,n'}^{0*}(\phi, \theta, -\phi) = D_{0,0}^0(\phi, \theta, -\phi) \equiv 1$. The upper D index being zero, therefore, is equivalent to the requirement that $|\lambda_{\gamma_a(c)} - \lambda_{\gamma_b(d)}| = 0$ and so $\lambda_{\gamma_a(c)} = \lambda_{\gamma_b(d)} = \pm 1$. The quantization axis can be chosen such that $\phi_p = 0$ so that $D_{m,\lambda_p-\lambda_{\bar{p}}}^J(0, \theta^*, 0) = d_{m,\lambda_p-\lambda_{\bar{p}}}^J(\theta^*)$ where, by definition, $\theta^* \equiv \theta_p$. Furthermore, the choice of quantization axis can be made such that $\theta_{\omega_1} = 0$ and thus

$$D_{m,\lambda_{\omega_1}-\lambda_{\omega_2}}^{J*}(\phi_{\omega_1}, 0, -\phi_{\omega_1}) = e^{-i\phi_{\omega_1}(m-(\lambda_{\omega_1}-\lambda_{\omega_2}))} \delta_{m,\lambda_{\omega_1}-\lambda_{\omega_2}}$$

After inserting the value of the ω spin, $J_\omega = 1$, and summing over m , the amplitude becomes

$$\begin{aligned} A^{JP} \propto \sum_{\{\lambda_{\omega_1}, \lambda_{\omega_2}\}} & \left\{ f_{\lambda_p, \lambda_{\bar{p}}} a_{\lambda_{\omega_1}, \lambda_{\omega_2}} b_{\lambda_{\gamma_1}, 0} c_{\lambda_{\gamma_2}, 0} d_{\lambda_{\omega_1}-\lambda_{\omega_2}, \lambda_p-\lambda_{\bar{p}}}^J(\theta^*) \right\} \\ & \times D_{\lambda_{\omega_1}, \lambda_{\gamma_1}}^{1*}(\phi_{\gamma_1}, \theta_{\gamma_1}, -\phi_{\gamma_1}) D_{-\lambda_{\omega_2}, \lambda_{\gamma_2}}^{1*}(\phi_{\gamma_2}, \theta_{\gamma_2}, -\phi_{\gamma_2}) \end{aligned} \quad (C.8)$$

It is at this stage that if interference appeared in the data, the terms such as $|A^{0+} A^{2+}|$ should be investigated.

Parity conservation requires that, for the decay $1 \rightarrow 2 + 3$, with angular momentum J and coupling amplitude $\varpi_{\lambda_2, \lambda_3}$

$$\varpi_{\lambda_2, \lambda_3} = P_1 P_2 P_3 (-1)^J \varpi_{-\lambda_2, -\lambda_3} \quad (C.9)$$

and charge conjugation conservation requires

$$\varpi_{\lambda_2, \lambda_3} = (-1)^J \varpi_{\lambda_3, \lambda_2} \quad (C.10)$$

Thus we come up with the following requirements on the coupling amplitudes b and c ,

$$\begin{aligned} |b_{1,0}|^2 &= |b_{-1,0}|^2 \\ |c_{1,0}|^2 &= |c_{-1,0}|^2 \end{aligned}$$

Since the squares are equal, these amplitudes can be factored out of the equation as well.

Two useful properties of the D-functions are,

$$D_{n',n}^J(\xi) = (-1)^{n'-n} D_{-n',-n}^J(\xi) \quad (\text{C.11})$$

and

$$D_{n'_1, n_1}^{J_1}(\xi) D_{n'_2, n_2}^{J_2}(\xi) = \sum_{j, n', n} (2j+1) D_{n', n}^j(\xi) \begin{pmatrix} J_1 & J_2 & j \\ n'_1 & n'_2 & n' \end{pmatrix} \begin{pmatrix} J_1 & J_2 & j \\ n_1 & n_2 & n \end{pmatrix}$$

where the Wigner 3-j symbols have been introduced to define D-function multiplication (the 3-j symbol is zero unless $n_1^{(')} + n_2^{(')} = -n^{(')}$). With β defined as the azimuthal angle between γ_1 and γ_2 (i.e. the angle between the two $\pi^0\gamma$ decay planes in the $\bar{p}p$ center of mass), ϕ_{γ_1} will be replaced by $\beta + \phi_{\gamma_2}$. After multiplying the amplitude by its complex conjugate and using the D-function properties above, the only occurrences of the angle ϕ_{γ_2} is in the term,

$$e^{im(\beta+\phi_{\gamma_2})} d_{m,0}^j(\theta_{\gamma_2}) e^{im'\phi_{\gamma_2}} d_{m',0}^{j'}(\theta_{\gamma_2}) \quad (\text{C.12})$$

The ϕ dependence of the term is thus $e^{i\phi_{\gamma_2}(m+m')}$ so that the integral of the squared

amplitude can be performed over ϕ_{γ_2} to get a delta function, $\delta_{m,-m'}$. By summing over final state helicities and averaging over initial state helicities the differential cross section is obtained,

$$\frac{d\sigma}{d\Omega} = \frac{1}{2} \sum_{\left\{ \begin{smallmatrix} \lambda_p & \lambda_{\bar{p}} \\ \lambda_{\gamma_1} & \lambda_{\gamma_2} \end{smallmatrix} \right\}} |A^{J^P}|^2 \quad (\text{C.13})$$

So, after performing the sum over m' , λ_{γ_1} , and λ_{γ_2} , the differential cross section is,

$$\begin{aligned} \frac{d\sigma}{d\Omega} \propto & \sum_{\left\{ \begin{smallmatrix} \lambda_p, \lambda_{\bar{p}}, j, j', m \\ \lambda_{\omega_1}, \lambda_{\omega_2}, \lambda'_{\omega_1}, \lambda'_{\omega_2} \end{smallmatrix} \right\}} \\ & \left\{ |f_{\lambda_p, \lambda_{\bar{p}}}|^2 a_{\lambda_{\omega_1}, \lambda_{\omega_2}} a_{\lambda'_{\omega_1}, \lambda'_{\omega_2}}^* d_{\lambda_{\omega_1}-\lambda_{\omega_2}, \lambda_p-\lambda_{\bar{p}}}^J(\theta^*) d_{\lambda'_{\omega_1}-\lambda'_{\omega_2}, \lambda_p-\lambda_{\bar{p}}}^J(\theta^*) \right\} \\ & \times (-1)^{\lambda_{\omega_1}-\lambda_{\omega_2}} (2j+1) (2j'+1) (-1)^m e^{im\beta} d_{m,0}^j(\theta_{\gamma_1}) d_{m,0}^{j'}(\theta_{\gamma_2}) \\ & \times \begin{pmatrix} 1 & 1 & j \\ -\lambda_{\omega_1} & \lambda'_{\omega_1} & m \end{pmatrix} \begin{pmatrix} 1 & 1 & j \\ -1 & 1 & 0 \end{pmatrix} \begin{pmatrix} 1 & 1 & j' \\ -\lambda_{\omega_2} & \lambda'_{\omega_2} & m \end{pmatrix} \begin{pmatrix} 1 & 1 & j' \\ -1 & 1 & 0 \end{pmatrix} \end{aligned} \quad (\text{C.14})$$

The integral over θ_{γ_2} can now be performed over the entire range $\cos \theta_{\gamma_2}$ from -1 to 1. This helps to make the properties of the differential cross section more transparent and no information is lost since the angular distribution of γ_2 will be the same as that for γ_1 . Also, note from the parity conservation requirements in equation C.9 that, where η is the parity quantum number of the initial state of the reaction,

$$a_{1,1} a_{-1,-1}^* = a_{1,1}^* a_{-1,-1} = \eta |a_{1,1}|^2 \quad (\text{C.15})$$

Upon summing over the remaining helicities,

$$\begin{aligned}
\left(\frac{d\sigma}{d\Omega}\right)_J &\propto \tag{C.16} \\
&2|a_{11}|^2(|f_{\frac{1}{2},\frac{1}{2}}|^2(d_{0,0}^J(\theta^*))^2 + |f_{\frac{1}{2},-\frac{1}{2}}|^2(d_{1,0}^J(\theta^*))^2)(1 + \frac{1}{2}P_2(\cos\theta_{\gamma_1})) \\
&+ |a_{00}|^2(|f_{\frac{1}{2},\frac{1}{2}}|^2(d_{0,0}^J(\theta^*))^2 + |f_{\frac{1}{2},-\frac{1}{2}}|^2(d_{1,0}^J(\theta^*))^2)(1 - P_2(\cos\theta_{\gamma_1})) \\
&+ 2|a_{10}|^2(2|f_{\frac{1}{2},\frac{1}{2}}|^2(d_{1,0}^J(\theta^*))^2 + \\
&\quad |f_{\frac{1}{2},-\frac{1}{2}}|^2((d_{1,1}^J(\theta^*))^2 + (d_{1,-1}^J(\theta^*))^2))(1 - \frac{1}{4}P_2(\cos\theta_{\gamma_1})) \\
&+ |a_{1-1}|^2(2|f_{\frac{1}{2},\frac{1}{2}}|^2(d_{2,0}^J(\theta^*))^2 + \\
&\quad |f_{\frac{1}{2},-\frac{1}{2}}|^2((d_{2,1}^J(\theta^*))^2 + (d_{2,-1}^J(\theta^*))^2))(1 + \frac{1}{2}P_2(\cos\theta_{\gamma_1})) \\
&+ \frac{\sqrt{6}}{2}\eta|a_{11}|^2d_{2,0}^2(\theta_{\gamma_1})\cos 2\beta(|f_{\frac{1}{2},\frac{1}{2}}|^2(d_{0,0}^J(\theta^*))^2 + |f_{\frac{1}{2},-\frac{1}{2}}|^2(d_{1,0}^J(\theta^*))^2)
\end{aligned}$$

From equations C.9 and C.10, as well as from helicity requirements based on the magnitude of the total angular momentum, we get the constraints,

$$\begin{aligned}
J = 0 &\Rightarrow a_{1,0} = a_{0,0} = 0 \\
J = 1 &\Rightarrow a_{1,-1} = 0 \\
J = \text{odd} &\Rightarrow f_{\frac{1}{2},\frac{1}{2}} = a_{1,1} = a_{0,0} = 0 \\
\eta = -1 &\Rightarrow f_{\frac{1}{2},-\frac{1}{2}} = a_{1,-1} = 0 \\
J = \text{even} \ \&\ \eta = -1 &\Rightarrow a_{0,0} = 0
\end{aligned}$$

The articles written by Trueman [67] and Richman [68] were inspirational in helping the author perform this calculation.

Bibliography

- [1] Murray Gell-Mann. “Nonleptonic Weak Decays and the Eightfold Way.” *Physics Letters* 12:155–156 (1964).
- [2] Murray Gell-Mann. “A Schematic Model of Baryons and Mesons.” *Physics Letters* 8:214–215 (1964).
- [3] G. Zweig. “An $Su(3)$ Model for Strong Interaction Symmetry and it’s Breaking.” *CERN Reports* th412 (1964).
- [4] J. D. Bjorken and S. L. Glashow. “Elementary Particles and $Su(4)$.” *Physics Letters* 11:255–257 (1964).
- [5] N. Cabibbo. “Unitary Symmetry and Leptonic Decays.” *Physical Review Letters* 10:531–532 (1963).
- [6] L. Maiani S. L. Glashow, J. Iliopoulos. “Weak Interactions with Lepton - Hadron Symmetry.” *Physical Review D* 2:1285–1292 (1970).
- [7] Thomas Appelquist and H. David Politzer. “Heavy Quarks and e^+e^- Annihilation.” *Physical Review Letters* 34:43–45 (1975).
- [8] J. J. Aubert et al. “Experimental Observation of a Heavy Particle J.” *Physical Review Letters* 33:1404–1406 (1974).

- [9] J. E. Augustin et al. "Discovery of a Narrow Resonance in e^+e^- Annihilation." *Physical Review Letters* 33:1406–1408 (1974).
- [10] M. K. Gaillard and Benjamin W. Lee. "Rare Decay Modes of the K- Mesons in Gauge Theories." *Physical Review D* 10:897 (1974).
- [11] S. Okubo. "Phi Meson and Unitary Symmetry Model." *Physics Letters* 5:165–168 (1963).
- [12] Jugoro Iizuka. "Systematics and Phenomenology of Meson Family." *Prog. Theor. Phys. Suppl.* 37-38:21–34 (1966).
- [13] G. S. Abrams et al. "The Discovery of a Second Narrow Resonance in e^+e^- Annihilation." *Physical Review Letters* 33:1453–1455 (1974).
- [14] Richard P. Feynman. "Very High-Energy Collisions of Hadrons." *Physical Review Letters* 23:1415–1417 (1969).
- [15] E. Eichten et al. "Charmonium: Comparison with Experiment." *Physical Review D* 21:203–233 (1980).
- [16] J. Pumplin et al. "Fine Structure Corrections and Electromagnetic Decays of Charmonium." *Physical Review Letters* 35:1538 (1975).
- [17] Howard J. Schnitzer. "P States of Charmonium and the Forces that Confine Quarks." *Physical Review Letters* 35:1540 (1975).
- [18] V. B. Berestetskii, E. M. Lifshitz, and L. P. Pitaevskii. *Quantum Electrodynamics*. Pergamon Press, 1982.
- [19] A. B. Henriques et al. "Radiative Transitions and the P Wave Levels in Charmonium." *Physics Letters B* 64:85 (1976).

- [20] A. Rich. "Recent Experimental Advances in Positronium Research." *Rev. Mod. Phys.* 53:127–165 (1981).
- [21] Kamal Seth. Based on a Plot Provided by Kamal Seth.
- [22] C. Baglin et al. " J/ψ Resonance Formation and Mass Measurement in Anti-Proton - Proton Annihilations." *Nuclear Physics* B286:592 (1987).
- [23] C. Baglin et al. "Direct Observation and Partial Width Measurement of $\gamma\gamma$ Decay of Charmonium States." *Physics Letters* B187:191–197 (1987).
- [24] C. Baglin et al. "Search for the P Wave Singlet Charmonium State in Anti-P P Annihilations at the CERN Intersecting Storage Rings." *Physics Letters* B171:135 (1986).
- [25] T.A. Armstrong et al. "Study of the χ_1 and χ_2 Charmonium States Formed in $\bar{p}p$ Annihilations." *Nuclear Physics* B373:35–54 (1992).
- [26] T.A. Armstrong et al. "Study of the η_c (S Wave Singlet) State of Charmonium Formed in $\bar{p}p$ Annihilations and a Search for the η'_c (S Wave Doublet)." *Physical Review* D52:4839–4854 (1995).
- [27] M. Ambrogiani et al. "Study of the χ_0 (1^3P_0) State of Charmonium Formed in $\bar{p}p$ Annihilations." *Physical Review Letters* 83:2902–2906 (1999).
- [28] Howard E. Haber and Jacques Perrier. "Model Independent Analysis of Hadronic Decays of J/ψ and η_c (2980)." *Physical Review* D32:2961 (1985).
- [29] J. Peoples. *IEEE Transitions on Nuclear Science* NS-30:1970 (1983).
- [30] Design Report. "Tevatron I Project, Fermi National Accelerator Laboratory." September 1984.

- [31] Camille Marie Ginsburg. "Spectroscopy of J/ψ and ψ' Charmonium Resonances." Ph.D. diss., Northwestern University, 1995.
- [32] S. Chattopadhyay. "Some Fundamental Aspects of Fluctuations and Coherence in Charged-Particle Beams in Storage Rings." In *Proceedings of Physics of High Energy Accelerators*, 1983.
- [33] A. A. Zholentz et. al. "High Precision Measurement of the J/ψ and ψ' - Meson Masses." *Physics Letters* 96B:214 (1980).
- [34] Guilio Stancari. Plot Provided by Guilio Stancari.
- [35] D. Allspach et al. "The Variable Density Gas Jet Internal Target for Experiment 835 at Fermilab." *Nuclear Instruments and Methods* A410:195–205 (1998).
- [36] S. Trokenheim et al. "A $\bar{p}p$ Luminosity Monitor for Fermilab Experiment E760." *Nuclear Instruments and Methods* A355:308–319 (1995).
- [37] T. A. Armstrong et al. "Precision Measurements of Antiproton-Proton Forward Elastic Scattering Parameters in the 3.7 to 6.2 GeV/c Region." *Physics Letters* B385:479 (1996).
- [38] Todd K. Pedlar. "Elements of Precision: Luminosity Measurement in E835." E835 Internal Memo.
- [39] A. Buzzo et al. "A Silicon Pad Detector for E835 Experiment at Fermilab." *Nuclear Instruments and Methods* A391:443–451 (1997).
- [40] S. Bagnasco et al. "A Straw Chambers' Tracker for the High Rate Experiment 835 at the Fermilab Accumulator." *Nuclear Instruments and Methods* A409:75–78 (1998).

- [41] M. Ambrogiani et al. "Results from the E835 Scintillating Fiber Detector." *Nuclear Instruments and Methods* A419:632–636 (1998).
- [42] S. Bagnasco et al. "The Threshold Gas Cherenkov Counter of Charmonium Experiment 835 at Fermilab." *Nuclear Instruments and Methods* A424:304–320 (1999).
- [43] Todd K. Pedlar. "A Study of Two Photon Decays of Charmonium Resonances Formed in Proton-Antiproton Annihilations." Ph.D. diss., Northwestern University, 1999.
- [44] G. A. Akopdjanov et al. "Determination of Photon Coordinates in a Hodoscope Cherenkov Spectrometer." *Nuclear Instruments and Methods* A140:441–445 (1977).
- [45] Michelle Dawn Stancari. "Two Photon Decay Widths of Charmonium Resonances Formed in Proton-Antiproton Annihilations." Ph.D. diss., University of California, Irvine, 1999.
- [46] M. A. Hasan et al. "The Fermilab E760 Forward Electromagnetic Calorimeter." *Nuclear Instruments and Methods* A295:73–80 (1990).
- [47] DART collaboration and Fermilab Computing Division. "DYC3 Write-Up v1.0." <http://fnphyx-www.fnal.gov/elec/dyc3/dyc3nov.html>.
- [48] Wander Baldini. "Studio del Decadimento in Due Mesoni ϕ dello Stato η_c del Charmonio Formato in Annichilazione protone-antiprotone e ricerca dello stato η'_c ." Ph.D. diss., Università degli studi di Ferrara, 1998.
- [49] R. Ray et al. "A Trigger for the Fermilab E760 Lead Glass Calorimeter." *Nuclear Instruments and Methods* A307:254–264 (1991).

- [50] Sheng Jin and Jerry Rosen. "E835 Neutral Trigger." E835 Internal Memo 375.
- [51] Sheng Jin. "Ccal Gain Constants Adjustment." E835 Internal Memo 376.
- [52] O. I. Dahl, T. B. Day, and F. T. Solmitz. "SQUAW: Kinematic Fitting Program." Technical Report P-126, University of California Lawrence Radiation Laboratory, 1965.
- [53] Sheldon M. Ross. *Introductory to Probability and Statistics for Engineers and Scientists*. John Wiley and Sons, Inc., 1987.
- [54] Chen-Ning Yang. "Selection Rules for the Dematerialization of a Particle into Two Photons." *Physical Review* 77:242–245 (1950).
- [55] Donald H. Perkins. *Introduction to High Energy Physics*. Addison-Wesley Publishing Company, Inc., 1987.
- [56] Paolo Rumerio. Ph.D. diss., Northwestern University, Unpublished.
- [57] Theodore Vidnovic III. Ph.D. diss., University of Minnesota, Unpublished.
- [58] M. Jacob and G. C. Wick. "On General Theory of Collisions for Particles with Spin." *Annals of Physics* 7:404–428 (1959).
- [59] *The European Physical Journal C*, volume 15. 2000.
- [60] Wander Baldini and Flavio Marchetto. "Charged Trigger Efficiency for Inclusive j/ψ ." E835 Internal Memo 373.
- [61] Gary J. Feldman and Robert D. Cousins. "Unified Approach to the Classical Statistical Analysis of Small Signals." *Physical Review* D57:3873–3889 (1998).

- [62] Byron P. Roe. *Probability and Statistics in Experimental Physics*. Springer-Verlag New York, Inc., 1992.
- [63] M. Ambrogiani et al. "Search for the Eta(c)-Prime ($2\ 1(S)0$) Charmonium Resonance." *Physical Review D* 64:052003 (2001).
- [64] C. Edwards et al. "Upper Limit for $J / \Psi \rightarrow \text{Gamma Axion}$." *Physical Review Letters* 48:903 (1982).
- [65] T. Goldman and H. E. Haber. "Double ϕ Production in Charmonium Decays." Los Alamos Preprint LA-UR-83-2323 (1983).
- [66] Keith Gollwitzer and Todd K. Pedlar. "E835 Neutral DST Format and Production Streaming." E835 internal Memo 394.
- [67] T. L. Trueman. " $\phi\phi$ Decay as a Parity and Signature Test." *Physical Review D* 18:3423-3426 (1978).
- [68] J. Richman. "An Experimenter's Guide to the Helicity Formalism." Technical Report CALT-68-1148, California Institute of Technology, 1984.